UNIVERSITÄT ZU KÖLN

DOCTORAL THESIS

Hydrodynamic Modelling of Swimming Bacteria at Surfaces and in Thin Film

Author:
Bohan ZHANG

Supervisor:
Dr. Dmitry FEDOSOV
Dr. Gerhard GOMPPER

A thesis submitted in fulfillment of the requirements for the degree of Doctor of Philosophy

April 7, 2025

Abstract

Microorganisms are unique on Earth. They employ self-propulsion to explore the environment and seek nutrition. Their space exploration behavior is often considered to be hydrodynamically mediated and occurs in a regime with negligible inertial effect. One of the well-studied bacteria is *E. Coli* which has a motility pattern called "run and tumble". *E. Coli* is observed to swim straight for some time (run) with rapid reorientations (tumble). *E. Coli*-like microswimmers can be modeled as active particles. Systems consisting of active particles are out of equilibrium, and they are common in collective phenomena such as active turbulence, motility-induced phase separation (MIPS), and swarming.

Swarming is a typical phenomenon for bacteria, which can form large aggregates and migrate collectively. Swarming serves as the key to understanding physical mechanisms of biofilm formation. Many studies have considered the effects of hydrodynamic and steric interactions between bacteria on swarming. However, most of them have been limited to small-scale simulations or experiments. We employ a simplified model of microswimmers, the squirmer model, which has been shown to have good precision in modeling for field hydrodynamics. We consider a system of squirmers within a thin film confined between two no-slip walls. The thickness of the thin film allows a free rotation of spheroidal squirmers, but constrains them to have a two-layer structure. We investigate the effect of different parameters on collective behavior, including volume fraction, motility types (pusher, puller, or neutral squirmers), and the presence of rotlet dipole, which mimics the counter-rotating flow generated by flagellated bacteria. Different structural and dynamic properties are analyzed, characterizing the behavior of the systems into different states, including gas-like phase, swarming, and motility-induced phase separation. We found that the formation of collective structures is due to an interplay between the anisotropic shape of swimmers, hydrodynamic interactions between swimmers, and the steric interaction of swimmers with the walls. Furthermore, we highlight the influence of the walls on the emergent structure, and show that the differences in collective behavior for different swimming modes are strongly reduced by the presence of rotlet dipole. In the future, less confined or even semi-open systems to mimic the behavior of bacteria during biofilm growth should be considered.

Despite the seeming simplicity of the run-and-tumble behavior, the physical mechanisms underlying are still not fully understood. We establish a detailed run-and-tumble *E. Coli* model, which is suspended in a fluid simulated by dissipative particle dynamics (DPD). The motility behavior is calibrated by experimental measurements. We investigate how different *E. Coli* properties, including the body and flagella geometry, flagella stiffness and actuation strength, govern the run-and-tumble behavior. The model adequately captures essential physical properties of *E. Coli*, such as the rotational frequency of the body and flagella, tumbling time, and tumbling angle, which compare well to available experimental measurements. Furthermore, our simulations show that the stiffness of a hook (the short part of a flagellum that connects it directly to the motor) plays a vital role in the run-and-tumble behavior, which has also been suggested in some experimental studies. Also, simulations of *E. Coli* with different numbers of flagella were performed, demonstrating that our model can represent different types of *E. Coli*. This detailed model helps us better understand *E. Coli*'s swimming behavior and allows the exploration of *E. Coli* locomotion in more complex realistic environments.

Furthermore, we study how *E. Coli* tumbling enables the bacterium to escape. As suggested by Junot et al., 2022, tumbling is the dominant escape mechanism for

wild-type *E. Coli* which is subject to "wall entrapment" effect. We perform simulations using the *E. Coli* model confined between two no-slip walls. We collect a number of instances of successful escapes, and analyze the distribution of escape angles and the number of tumbles before escaping, which compare well with those in Junot et al., 2022. Finally, we conclude that the orientation of *E. Coli* body after tumbling determines its escape success. The work provides a novel way to investigate in detail the behavior of flagellated swimmers under confinement. Also, it would be interesting to study the collective behavior of many swimmers using this detailed model.

This thesis includes the studies of the behavior of single *E. Coli*-like microswimmers and their collectives. Studies of the collective behavior of active matter contribute to a better understanding of biofilm formation and the origin of different collective states. The detailed *E. Coli* model developed here can be used to explore the bacterial behavior in complex systems, providing a way to characterize the effects of detailed interactions, such as body-flagella and flagella-wall interactions, which are missing in simplified models such as squirmers. Therefore, the use of the detailed model to study the collective behavior of many bacteria bring us much closer to the understanding of the formation of biofilm.

Abstract

Mikroorganismen sind einzigartig auf der Erde. Sie nutzen ihren eigenen Antrieb, um die Umwelt zu erkunden und Nahrung zu finden. Ihr Verhalten bei der Erkundung des Weltraums wird häufig als hydrodynamisch vermittelt angesehen und findet in einem Bereich mit vernachlässigbarem Trägheitseffekt statt. Eines der gut untersuchten Bakterien ist *E. Coli*, das ein Motilitätsmuster namens "run and tumble" aufweist. *E. Coli* schwimmt eine Zeit lang geradeaus (run), um sich dann schnell umzuorientieren (tumble). *E. Coli*-ähnliche Mikroschwimmer können als aktive Teilchen modelliert werden. Systeme, die aus aktiven Teilchen bestehen, sind aus dem Gleichgewicht geraten und treten häufig in kollektiven Phänomenen wie aktiven Turbulenzen, bewegungsinduzierter Phasentrennung (MIPS) und Schwärmen auf.

Schwärmen ist ein typisches Phänomen für Bakterien, die große Aggregate bilden und gemeinsam wandern können. Das Schwärmen ist der Schlüssel zum Verständnis der physikalischen Mechanismen der Biofilmbildung. Viele Studien haben die Auswirkungen hydrodynamischer und sterischer Wechselwirkungen zwischen Bakterien auf das Schwärmen untersucht. Die meisten von ihnen beschränken sich jedoch auf Simulationen oder Experimente in kleinem Maßstab. Wir verwenden ein vereinfachtes Modell von Mikroschwimmern, das Squirmer-Modell, das sich bei der Modellierung der Hydrodynamik im Feld als sehr genau erwiesen hat. Wir betrachten ein System von Squirmern in einem dünnen Film, der zwischen zwei rutschfesten Wänden eingeschlossen ist. Die Dicke des dünnen Films erlaubt eine freie Rotation der kugelförmigen Squirmers, zwingt sie aber zu einer zweischichtigen Struktur. Wir untersuchen die Auswirkung verschiedener Parameter auf das kollektive Verhalten, einschließlich des Volumenanteils, der Motilitätstypen (Pusher, Puller oder neutrale Squirmers) und des Vorhandenseins eines Rotlet-Dipols, der die gegenläufige Strömung nachahmt, die von geißelnden Bakterien erzeugt wird. Es werden verschiedene strukturelle und dynamische Eigenschaften analysiert, die das Verhalten der Systeme in verschiedenen Zuständen charakterisieren, einschließlich der gasähnlichen Phase, des Schwärmens und der bewegungsinduzierten Phasentrennung. Wir fanden heraus, dass die Bildung kollektiver Strukturen auf ein Zusammenspiel zwischen der anisotropen Form der Schwimmer, hydrodynamischen Wechselwirkungen zwischen den Schwimmern und der sterischen Wechselwirkung der Schwimmer mit den Wänden zurückzuführen ist. Darüber hinaus heben wir den Einfluss der Wände auf die entstehende Struktur hervor und zeigen, dass die Unterschiede im kollektiven Verhalten für verschiedene Schwimmarten durch das Vorhandensein von Rotlet-Dipolen stark reduziert werden. In Zukunft sollten weniger begrenzte oder sogar halboffene Systeme in Betracht gezogen werden, um das Verhalten von Bakterien während des Biofilmwachstums zu imitieren.

Trotz der scheinbaren Einfachheit des Run-and-Tumble-Verhaltens sind die zugrunde liegenden physikalischen Mechanismen noch immer nicht vollständig verstanden. Wir erstellen ein detailliertes Run-and-Tumble von *E. Coli*-Modell, das in einer Flüssigkeit suspendiert ist, die durch dissipative Partikeldynamik (DPD) simuliert wird. Das Motilitätsverhalten wird durch experimentelle Messungen kalibriert. Wir untersuchen, wie verschiedene *E. Coli*, einschließlich der Körper- und Geißelgeometrie, der Steifigkeit der Geißel und der Antriebsstärke, das Run-and-Tumble-Verhalten bestimmen. Das Modell erfasst wesentliche physikalische Eigenschaften von *E. Coli*, wie z. B. die Rotationsfrequenz des Körpers und der Geißeln, die Taumelzeit und der Taumelwinkel, die sich gut mit den verfügbaren experimentellen Messungen vergleichen lassen. Darüber hinaus zeigen unsere Simulationen, dass die Steifigkeit eines Hakens (der kurze Teil einer Geißel, der sie direkt mit

dem Motor verbindet) eine entscheidende Rolle für das Run-and-Tumble-Verhalten spielt, was auch in einigen experimentellen Studien vermutet wurde. Auch Simulationen von *E. Coli* mit unterschiedlicher Anzahl von Geißeln durchgeführt, was zeigt, dass unser Modell verschiedene Arten von *E. Coli* darstellen kann. Dieses detaillierte Modell hilft uns, *E. Coli* besser zu verstehen und ermöglicht die Erforschung der Fortbewegung von *E. Coli* in komplexeren realistischen Umgebungen.

Darüber hinaus untersuchen wir, wie das Taumeln von *E. Coli*, durch Taumeln die Flucht des Bakteriums ermöglicht. Wie von Junot et al., 2022 vorgeschlagen, ist das Taumeln der dominante Fluchtmechanismus für Wildtyp-*E. Coli*, der dem "Wall-Entrapment"-Effekt unterliegt. Wir führen Simulationen mit dem *E. Coli*, das zwischen zwei rutschfesten Wänden eingeschlossen ist. Wir sammeln eine Reihe von Beispielen erfolgreicher Fluchten und analysieren die Verteilung der Fluchtwinkel und die Anzahl der Taumel vor der Flucht, die gut mit denen in Junot et al., 2022 vergleichbar sind. Schließlich kommen wir zu dem Schluss, dass die Ausrichtung des Körpers von *E. Coli*-Körpers nach dem Taumeln seinen Fluchterfolg bestimmt. Diese Arbeit bietet eine neue Möglichkeit, das Verhalten von Geißelschwimmern unter Begrenzung im Detail zu untersuchen. Außerdem wäre es interessant, das kollektive Verhalten vieler Schwimmer mit diesem detaillierten Modell zu untersuchen.

Diese Arbeit umfasst die Untersuchung des Verhaltens einzelner *E. Coli*-ähnlichen Mikroschwimmern und ihrer Kollektive. Studien zum kollektiven Verhalten aktiver Materie tragen zu einem besseren Verständnis der Biofilmbildung und des Ursprungs verschiedener kollektiver Zustände bei. Das detaillierte *E. Coli*-Modell kann zur Erforschung des bakteriellen Verhaltens in komplexen Systemen verwendet werden, da es eine Möglichkeit bietet, die Auswirkungen detaillierter Wechselwirkungen zu charakterisieren, wie z. B. die Wechselwirkungen zwischen Körper und Geißel und Geißel und Wand, die in vereinfachten Modellen wie Squirmers fehlen. Die Verwendung des detaillierten Modells zur Untersuchung des kollektiven Verhaltens vieler Bakterien bringt uns daher dem Verständnis der Biofilmbildung sehr viel näher.

Contents

Chapter 1

Introduction

1.1 Soft and active matter

Soft matter, by definition, is a board category including polymers, colloids, surfactants, liquid crystals, and others on a mesoscopic scale (Doi, 2013). The area of soft matter physics arises from the study of "Brownian motion," which was observed by Robert Brown (Brown, 1828). He immersed some grains of pollen with a typical size around $6-8\mu m$ into the water and noticed "many of them very evidently in motion." This motion was subsequently quantified and theorized by Einstein, 1905. Such research systems nowadays are called "colloids," which is the definition of a mixture where a substance of dispersed insoluble particles suspends in another substance. At the length scale of colloids, thermal fluctuation becomes an important factor in their motion, and it has an energy scale of kBT. The study of colloid physics has great implications for varied areas of research, such as nanomaterials (Maas, 2016), drug delivery (Yang and Alexandridis, 2000), biological sensors (Howes, Chandrawati, and Stevens, 2014) and etc.

Another fruitful area of our concern is active matter which is referred to the class of systems out of equilibrium, common in biological physical studies, such as bacteria and sperms. Compared to Brownian motion mentioned previously, which are passive particles driven by thermal fluctuation, bacteria or sperms are active swimmers, and they propel fluid behind and actively move forward (Gompper et al., 2020). More generally, the constituent agents of an active matter system can convert energy into force or torque, driving persistent motion (Gompper et al., 2020; Elgeti, Winkler, and Gompper, 2015). The feature of active matter systems leads to phenomena such as motility-induced phase separation (MIPS), swarming, and other collective behaviors that are not observed in equilibrium systems. The long-range correlation and large-scale structures in the active systems can often be explained by broken detailed balance and non-equilibrium statistical mechanics (Gompper et al., 2020). For example, the Vicsek model proposed by Vicsek et al., 1995 describes a system of self-driven colloids (active colloids). The particles have a velocity orientation depending on the velocity orientations of neighboring particles within a cutoff radius, capturing how the local interactions affect the global order (Vicsek et al., 1995; Vicsek and Zafeiris, 2012). Furthermore, it has been reported that emergent collective patterns exist in varied length scales. On mesoscopic scale, there are phenomena such as bacterial swarming in colonies (Dombrowski et al., 2004); on macroscopic length scale, we can often observe flocks of birds (Toner and Irimia, 2005), the motion of pedestrian (Helbing et al., 2001) and traffic (Helbing et al., 2001). Understanding the physics underlying mesoscopic active matter systems is crucial for us to comprehend and tackle the challenges of some biological processes, such as biofilm formation (Nagel et al., 2020; Worlitzer et al., 2022), the invasion and migration of cancer cells (Schmidt et al., 2020; Grosser et al., 2021; Ilina et al., 2020), or

targeted drug delivery (Palagi and Fischer, 2018; Langer, 1990; Tran et al., 2017; Kim and Dobson, 2009).

1.2 Single swimmer

The physics describing the swimming behavior of microswimmers is often considered in a regime of low-Reynolds number where the inertia effect is negligible (Purcell, 1977). There are abundant biological microswimmers on Earth, such as spermatozoa, protozoa, bacteria, and algae. Their motion can be driven by chemotaxis (food gradient) and phototaxis (light intensity gradient), etc. Also, different motility strategies are employed, such as flagella rotation and flagella beating.

1.2.1 Prokaryotic swimmers

Many bacteria possess a structure of helical filament, aiding their swimming behavior. They are called, in general, multi-flagellated bacteria. Based on the arrangement and the number of flagella they have on their body, they can be classified into four different categories: 1) Monotrichous bacteria that only have a single flagellum, such as *Vibrio Cholerae*; 2) Lophotrichous bacteria, their flagella are attached at specific spots on the surface, such as *Helicobacter Pylori*; 3) Amphitrichous bacteria which only have two flagella and each of them is located at the opposite end of the body, with an example of *Alcaligenes Faecalis*. 4) Peritrichous bacteria, on its body surface, the flagella can be arranged randomly at any location. The famous bacteria, *Escherichia Coli* is peritrichous (Janssen and Graham, 2011).

FIGURE 1.1 shows that the structure of the prokaryotic helical flagella contains a filament and a hook, and the hook acts as a universal joint connecting to a motor. The function and property of the hook will be described in section 2.3.4. The motor is formed by several proteins and is anchored into the cell wall of bacteria (Berg, 2004; Berg, 2003; Turner, Ryu, and Berg, 2000; Hyon et al., 2012). During swimming, the motor enables the rotation of the flagella, propelling swimmers forward. Also, by changing the rotational direction of each motor, bacteria can change its swimming direction (Platzer et al., 1997; Scharf, 2002).

As shown in FIGURE 1.2, a wild-type *E. Coli* is composed of a body and several flagella. The body is prolate spheroidal-shaped with a dimension of $2.5 \pm 0.6\mu m$ for length and $0.88 \pm 0.09\mu m$ for width (Darnton et al., 2007). There are typically $2 - 5$ left-handed flagella attached to the body, each has a length around $8.3 \pm 2.0\mu m$(Lee et al., 2018b). A wild-type smooth swimmer has a speed of $29 \pm 6\mu m$ in a medium of viscosity of $0.93 \times 10^{-3} Pa \cdot s$ with a rotation frequency of body and flagellar bundle being $23 \pm 8Hz$ and $131 \pm 31Hz$, respectively (Darnton et al., 2007).

Bacteria such as *E. Coli* and *Salmonella Rtyphimurium* explore the environment by a motility pattern of "run and tumble," illustrated in FIGURE 1.3(b). During the run phase, the flagellar filaments coalesce into a bundle that rotates counterclockwise (CCW), propelling the bacterium forward as a single helical structure. When transitioning to a tumble, one or more flagella switch to clockwise (CW) rotation and dissociate from the bundle, facilitated by a process called polymorphic transformation (Refer to section 2.3.4). This action reorients the bacterium's swimming direction (Turner, Ryu, and Berg, 2000; Berg, 2004). At the end of a tumble, the clockwise rotating flagella rotate counterclockwise again and rejoin the bundle; a new run begins. In a homogeneous and isotropic medium, the movement of wild-type *E. coli*

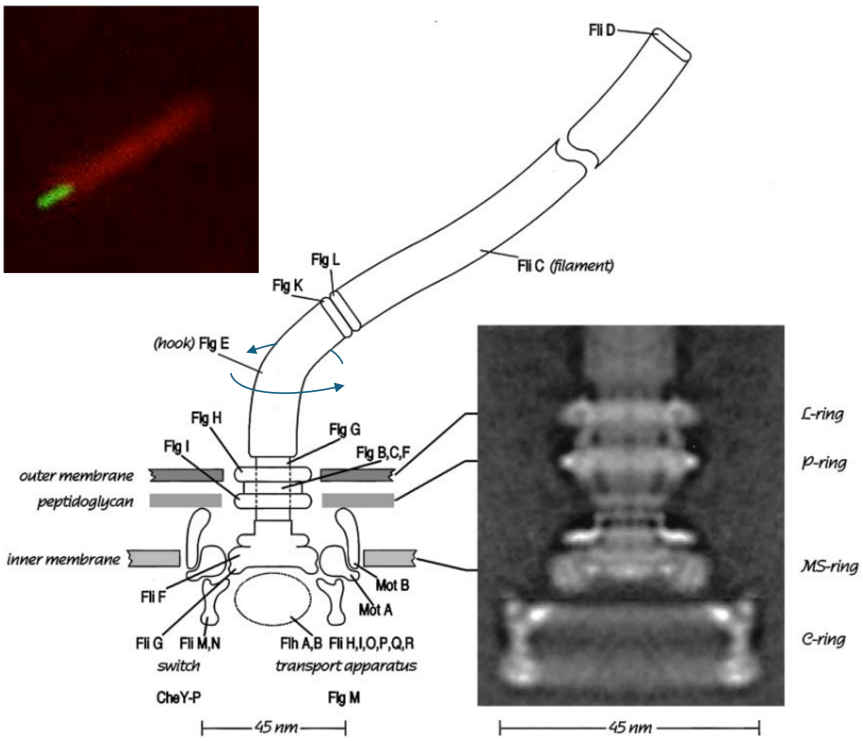

FIGURE 1.1: The flagellum structure and the motor connected to the flagellum and experimental observations of wild-type *E. Coli* strain RP437. A flagellum includes a hook and a filament; the hook acts as a universal joint point and is linked to a motor consisting of different protein complexes. The schematics of a photo of the motor are adapted from Berg, 2003 with permission, Annual Review of Biochemistry. The photo of wild-type *E. Coli* under microscopy is provided by Peixin Zhang, PMMH lab, Paris, France.

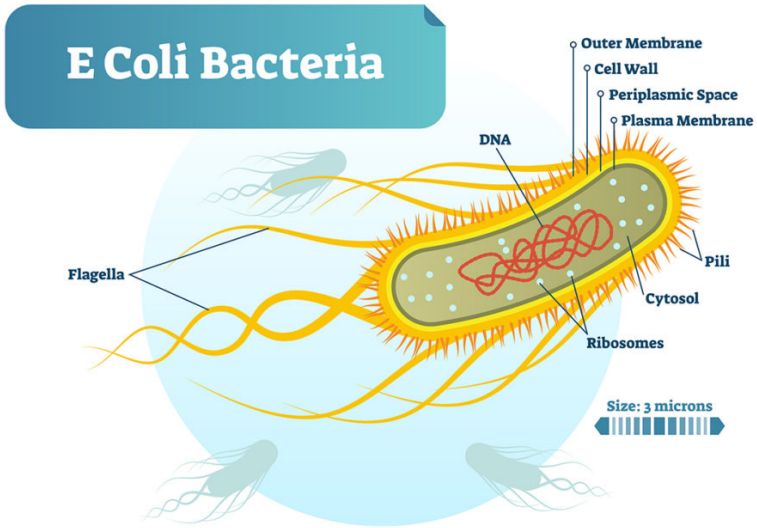

FIGURE 1.2: The structure of an *E. Coli* (Credit to VectorMine - stock.adobe.com)

follows a random walk pattern (Berg and Brown, 1972). In contrast, a chemical gradient biases this random walk and reduces the frequency of tumbling (Berg, 1977;

Blair, 1995).

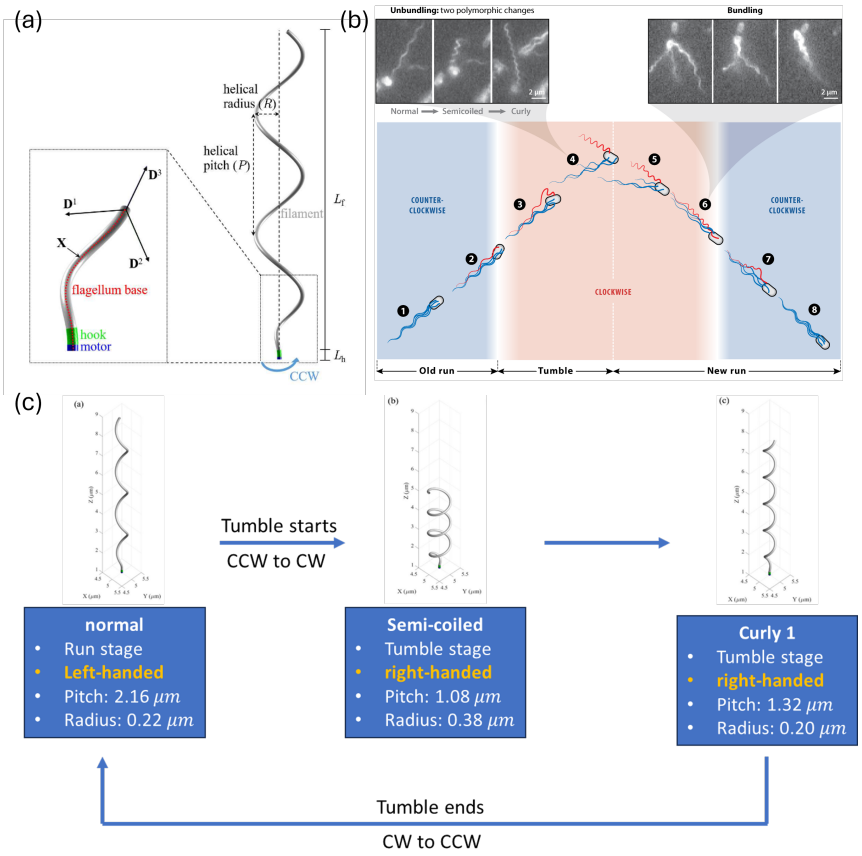

FIGURE 1.3: The experimental observations and the illustrations of the polymorphic transformation process within the run and tumble process. (a) The illustration of a helix with the demonstration of pitch length, radius, and helicity. Adapted with permission from Lee et al., 2018b, Physical Review E. (b) The process of run and tumble of a wild-type *E. Coli* with experimental observation attached. The picture is from Lauga, 2016, Annual Review (Open Access). (c) The details of how the tumbled flagellum changes its shape during a cycle of run and tumble. Adapted with permission from Lee et al., 2018b, Physical Review E.

The conformation of helices can be defined based on the chirality, pitch, and radius of helices. Chirality is also the handedness of a helix, and it can either be left-handed or right-handed, which are mirror images of each other. As shown in FIGURE 1.3(a), pitch length is the height of one complete turn by moving along the central axis of a helix. Radius is the radius of a helix turn. In the cycle of run and tumble, the three properties vary, resulting in different states of flagella, namely, "normal," "semi-coiled," and "curly-1", as shown in FIGURE 1.3(c) (Darnton et al., 2007; Turner, Ryu, and Berg, 2000; Berg, 2004). In the run stage, all of the flagella are in the normal state and rotate counter-clockwise, where they are left-handed with a pitch of $2.5\mu m$ and a radius of $0.22\mu m$. Following this, when a tumble starts, some filaments change to semi-coiled, then to curly-1 state, and rotate clockwise, while others remain in the normal state. The semi-coiled state is defined as a right-handed helix with pitch and radius of 1.32 and 0.38 μm, respectively. A helix at curly-1 state is right-handed with a pitch of $1.32\mu m$ and a radius of $0.20\mu m$. At the end of the

tumble, the CW rotating filament starts to rotate CCW again, and its conformation changes back to the normal state; they rejoin the bundle, and a new run begins.

1.2.2 Eukaryotic swimmers

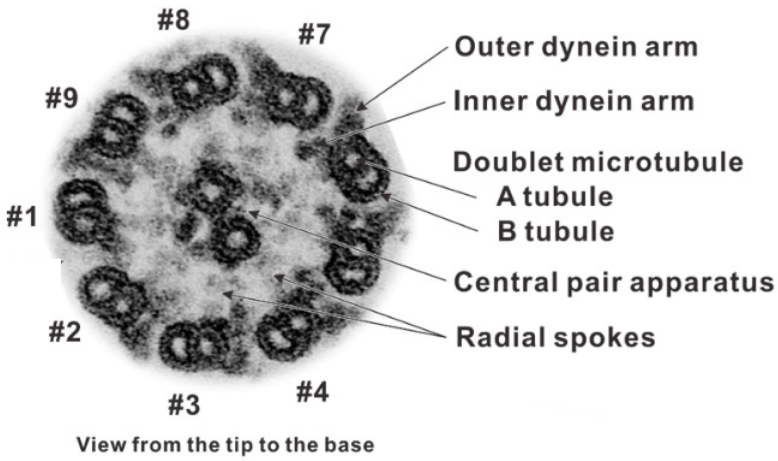

FIGURE 1.4: Structure and composition of a *Chlamydomonas* flagellar axoneme by double-stained ultra-thin section electron micrograph. The picture is from Ishibashi, Sakakibara, and Oiwa, 2020, Molecular Researches on Cilia, MDPI (Open Access)

.

Compared to prokaryotic cells, eukaryotic swimmers are facilitated by cilia or eukaryotic flagella. Cilia and eukaryotic flagella are similar in structure and composition, shown in FIGURE 1.4. The figure shows the cross-section of a flagellum or cilium. The structure is called an axoneme and is made up of a microtubule bundle where two microtubules serve as the central pair apparatus and 9 double microtubules surround them. Some proteins, such as radial spokes, stabilize the structure. The dyneins are motor proteins and also serve as the connecting protein linking the neighboring microtubules. During motion, dyneins slide microtubules over each other, resulting in an active bending force that soon spreads over the whole length of the structure. The difference between cilia and eukaryotic-flagella lies in two aspects: 1) Length: Cilium has a typical length of $10\mu m$ while $50\mu m$ for the flagellum (Elgeti, Winkler, and Gompper, 2015). 2) Beating patterns: The beating of the flagellum propagates a sinusoidal bending wave, while the cilia beat with two different phases called power stroke and recovery stroke. The beating patterns will be explained in more detail with specific examples of eukaryotic swimmers.

Sperm cells are produced in the human body to complete a run to reach the egg under chemotaxis (Kaupp et al., 2003; Eisenbach and Giojalas, 2006; Friedrich and Jülicher, 2007; Alvarez et al., 2014). It has a head, a middle piece, a principal piece, as well as a terminal segment, as shown in FIGURE 1.5. The head of $4\mu m$ long by $3\mu m$ in width, contains the nucleus, therefore including the genetic materials; the middle piece has many mitochondria for energy; and a flagellum made up of the principle piece and terminal segment as shown, it has a length of $41\mu m$. Sperm cells swim by beating their flagellum and wiggling through the liquid like a snake. As shown in FIGURE 1.6, the flagellar beating is a propagating bending wave. The bending wave of scallop spermatozoa is planar, which is typical for the sperm swimming on

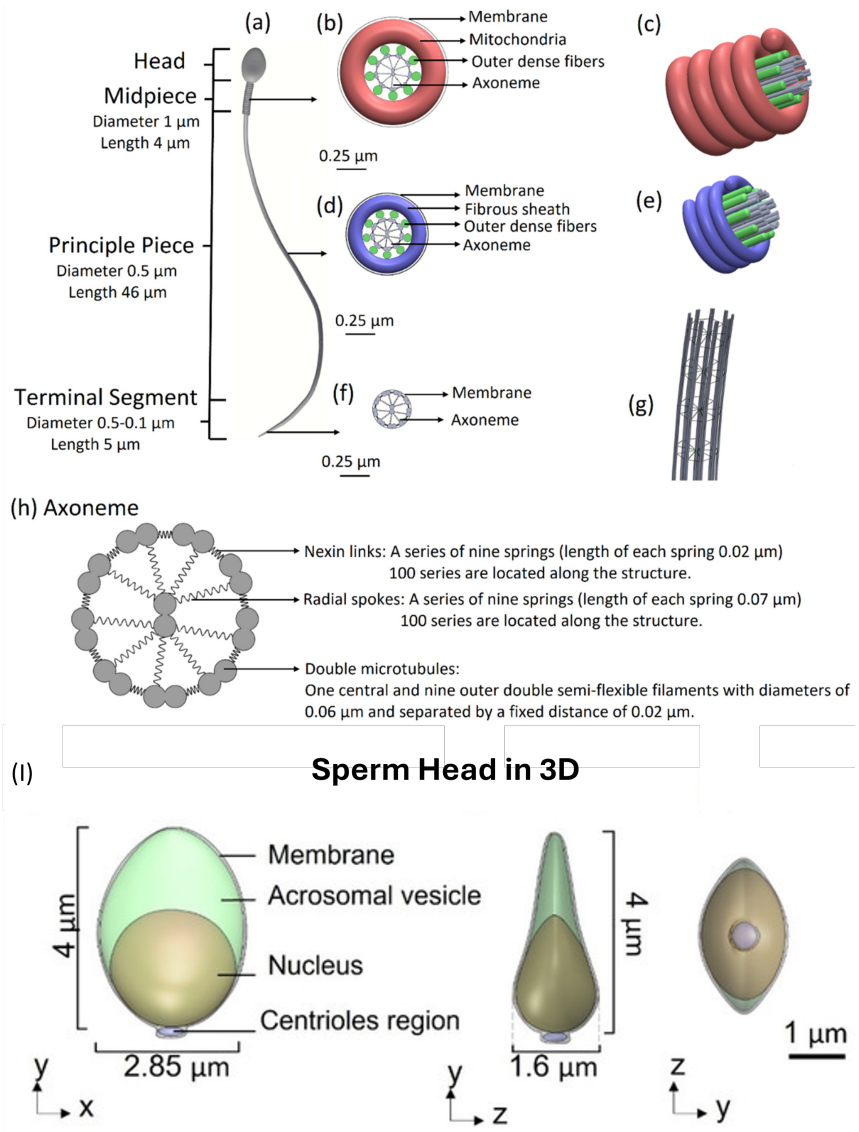

FIGURE 1.5: Demonstration of the structure of sperm. (a) overall structure of a sperm, consisting of a head (i), a middle piece (b-c), a principle piece d-e) and a terminal segment (f-g). (b), (d) and (f) give the cross-section of the corresponding structure while (c), (d) and (g) show the 3D structure. (h) The cross-section of axoneme: The double microtubules are connected by stiff springs (nexin links) and radial springs (radial spokes). (i) the 3D structure of a sperm head. Picture is adapted from Nassir et al., 2022, Cells, MDPI (Open Access)

the surface. The sperms have also been observed to have 3D waves with a conical envelope (Cosson et al., 2008).

Trypansomes (*T. brucei*) is a flagellated unicellular parasite and has caused trypanosomiasis in cows and humans. It has only 1 flagellum. However, unlike many single-flagellum microorganisms, the flagellum of Trypanosomes starts from the flagellar pocket, then wraps and goes along the whole body, demonstrated in FIGURE 1.7. The motility of trypanosomes is a result of the planar beat of the flagellum; also, the body with the asymmetrical shape induces a rotation motion while swimming (Uppaluri et al., 2011; Babu and Stark, 2012; Heddergott et al., 2012).

Chlamydomonas reinhardtii, a biflagellated alga of 10μm in size and two anterior

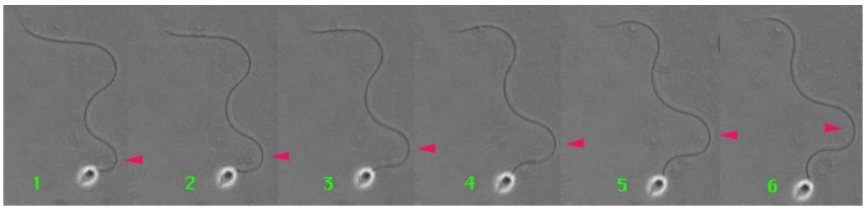

FIGURE 1.6: The time series of the movement of scallop spermatozoa. The flagellum beats and is shown as a sinusoidal traveling wave. The arrow points to the same bend area from image to image. The picture is adapted with permission from Bondarenko and Cosson, 2019, Theriogenology.

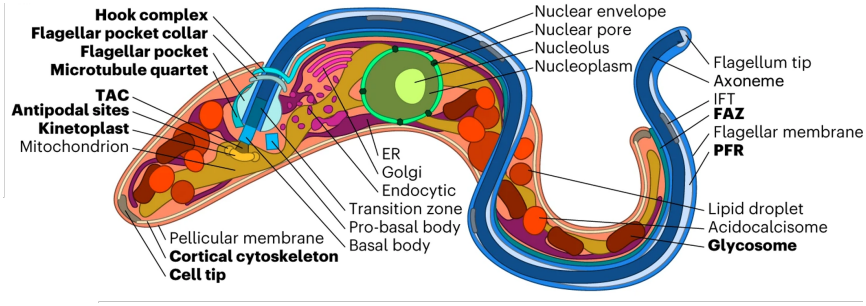

FIGURE 1.7: Schematics of trypansome structure. The organelles which are unique to trypansome lineage are labelled in bold font. The picture is from Billington et al., 2023, Nature Microbiology (Open Access).

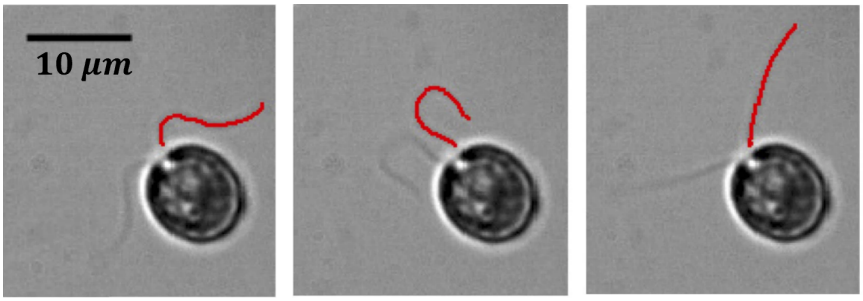

FIGURE 1.8: The breast-stroke-like motion of *chlamydomonas reinhardtii* during swimming. The beats of flagella aid the swimming. The photos are adapted from Qin et al., 2015, Scientific Reports (Open Access).

flagella of length around $10\mu m$ (Harris, 1989). It has a light-sensing spot; therefore, it swims under phototaxis. This bacteria can be commonly found in soil and freshwater. During swimming, the flagella of a *Chlamydomonas* executes a cyclical breast-stroke-like pattern, illustrated in FIGURE 1.8. In this cycle, the flagella are first stretched straight, bent over, and then pushed forward. This motion generates propulsion, and the local hydrodynamic field can be matched with the flow field of a "puller" (Guasto, Johnson, and Gollub, 2010; Harris, 1989).

Ciliates are a group of alveolates characterized by hair-like organelles called cilia on the surface, for example, *Paramecium* and *Opalinum*. *Paramecium* is a unicellular ciliate protozoa and can be typically found in marine water (Foissner, Chao, and Katz, 2009; Wichterman, 2012), such as ponds and lakes. They have a length ranging from 50 to $350\mu m$ and swim with a speed of a few millimeters per second (Machemer

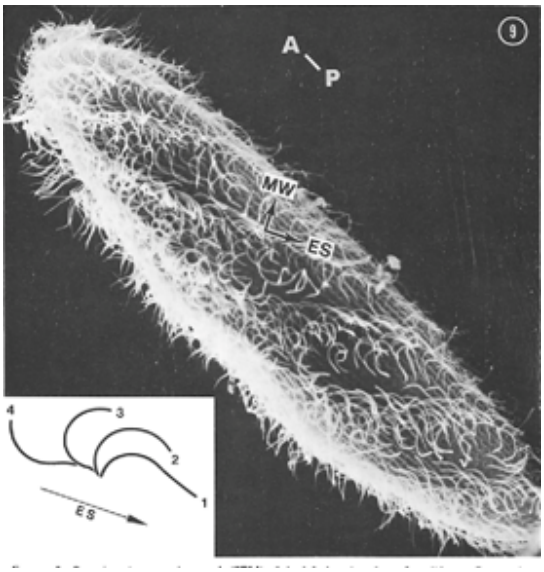

FIGURE 1.9: Scanning Electron Microscopy (SEM) of the surface of a wild-type Paramecium *in vitro*. The direction of the effective stroke (ES) of cilia on the surface is parallel to the metachronal wave (MW) front. The inset shows the beats of a single cilium. The cycle of a beat involves the power stroke (from position 4 to 1) and the recovery stroke (from position 2 -3). During the power stroke, the cilium is stretched out and moves rapidly in one direction, while in the recovery stroke, the cilium bends and retracts slowly. Photo is adapted from Tamm, Sonneborn, and Dippell, 1975, Journal of Cell Biology (Open Access).

and Machemer-Röhnisch, 1996). *Paramecium* is covered with cilia on the surface, and their cilia beat in the form of metachronal wave (FIGURE 1.9), propelling the swimmer to move forward. The beating is carried out in two phases: 1) power stroke, when the cilia become straight and move fast in one direction, followed by 2) recovery stroke, the cilia bend and twist, and then retract slowly (Tamm and Horridge, 1970; Machemer, 1972; Okamoto and Nakaoka, 1994).

Volvox is also a green algae, as shown in FIGURE 1.10. It is generally in a spheroidal shape of the colony, and it has a streamlined body surface consisting of two types of cells: 1) around 2000 somatic cells with the flagella pointed outwards to provide motility; 2) around 16 reproductive cells located inside the spheroid. A clear extracellular matrix occupies 99% of the volume where all the cells are embedded. The structure of the somatic cells is very similar to *Chlamydomonas Reinhardtii*. Volvox likes to swim toward light, which is enabled by the eye spots of the somatic cells. The eye spots are more developed near the anterior rather than the posterior. Volvox is a perfect example to be modeled by the squirmer model (section 2.3.3) because the synchronized motion of the flagella of somatic cells on the surface leads to a velocity difference between the surface and the local flow field. The flow field has been measured experimentally in some literature (Drescher et al., 2009; Drescher et al., 2010).

1.2.3 Synthetic microswimmers

With years of technology, synthetic microswimmers have great attention to their potential ability to move through a fluid phase and perform desired tasks. These

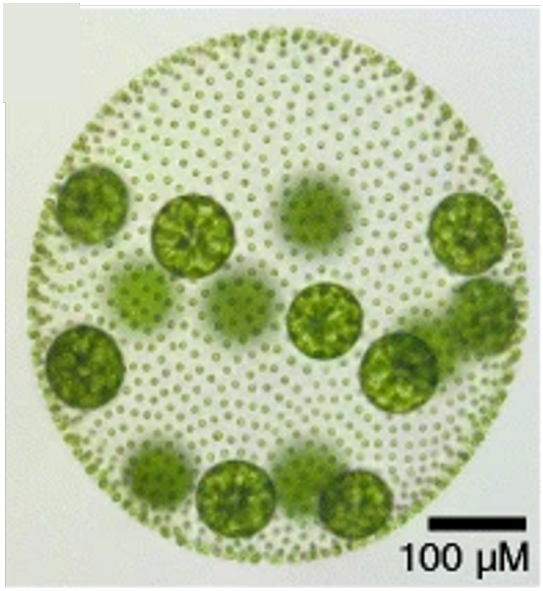

FIGURE 1.10: Light Microscopy of *Volvox Carteri*. It is a colony of thousands of cells organized into a spheroidal structure with a gel-like extracellular matrix. The larger cells are reproductive cells, and the small cells are somatic cells. Photo is adapted from Russell et al., 2017, BMC Biology (Open Access).

swimmers are built from nano blocks and have an energy source from *in situ* chemical reactions. This paragraph will introduce several examples, including bimetallic nanorods and microspheres, Janus colloids, and biomimetric microswimmers.

The bimetallic nanorods and microspheres have nanoscale motors made by immersing bimetallic Pt-Au nanorods in H_2O_2 solution. Pt and Au act as two electrodes, catalyzing the reaction of the dissolution of H_2O_2 into water and oxygen, producing energy (Paxton et al., 2004; Paxton et al., 2006; Fournier-Bidoz et al., 2005). Janus colloids classify a class of spherical particles composed of polystyrene or silica and a metallic cap. Due to the different reactions the metallic head could have, Janus colloids are further divided into catalytic or thermophoretic Janus colloids. For catalytic Janus particles, the metal catalyzes the chemical reaction happening in the fluid, leading to unbalanced distribution of reaction products, causing self-propulsion (Rückner and Kapral, 2007; Popescu, Dietrich, and Oshanin, 2009; Popescu et al., 2010; Popescu, Tasinkevych, and Dietrich, 2011; Thakur and Kapral, 2011; Golestanian, Liverpool, and Ajdari, 2005; Golestanian, 2009; Sabass and Seifert, 2012). For thermophoretic Janus colloids, they produce self-propulsion by self-thermophoresis where one end of metallic cap is heated by a laser beam while the other end not, generating a temperature difference so that the colloids diffuse (Jiang, Yoshinaga, and Sano, 2010; Rings et al., 2010; Yang and Ripoll, 2011; Bickel, Majee, and Würger, 2013; Buyl and Kapral, 2013; Braun and Cichos, 2013). Finally, the microswimmers designed according to the self-propulsion principles found in natural biological systems are classified as biomimetic microswimmers. There are a few examples, such as the swimmers mimicking the propulsion mechanism of a sperm cell (Dreyfus et al., 2005; Williams et al., 2014) and artificial cilia (Sanchez et al., 2011).

1.3 Collective Behavior

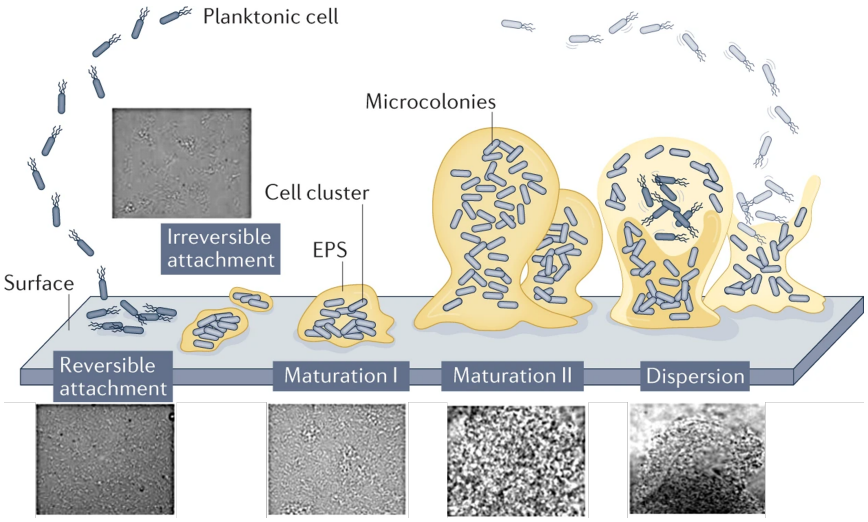

FIGURE 1.11: The demonstration of biofilm growth of bacteria *Pseudomonas aeruginosa* with experimental observation at every stage. There are five stages involved (Sauer et al., 2002; Petrova and Sauer, 2009). 1) Reversible attachment: Bacteria are attached to the surface by longitudinal attachment. 2)Irreversible attachment: During this stage, flagella reversal rates and flagella gene expression of bacteria decrease, and the biofilm matrix starts to be formed. 3) Biofilm Maturation I: Cells form clusters, and they are embedded in the matrix. 4) Biofilm Maturation II: The cell clusters develop into microcolonies.5) Dispersion: The biofilm matrix is degraded, and bacteria are released; these dispersed cells are motile. The experimental snapshots are adapted with permission from (Stoodley et al., 2002), Annual Reviews. The cartoon demonstration is adapted from (Sauer et al., 2022), Nature Reviews Microbiology (Open Access).

Biofilms are communities of microorganisms that grow from a pre-conditioning protein layer and form a protective matrix of extracellular polymeric substances (Flemming and Wingender, 2010; Wingender, Neu, and Flemming, 1999). Bacterial colonies with multiple strains and phenotypes interact and cooperate to perform complicated tasks, such as nutrient acquisition (Peterson et al., 2015; Flemming and Wingender, 2010), waste removal, and defense mechanisms. The formation of biofilms is often irreversible and stably fast (FIGURE 1.11), which is due to a few factors (Flemming and Wingender, 2010; Mann and Wozniak, 2012; Gloag et al., 2013; Pearce et al., 2019; Allen, Habimana, and Casey, 2018): 1) Bacteria produce adhesion proteins or pili that help them attach to surfaces (Berne et al., 2018). 2) Bacteria secrete Extracellular Polymeric Substances (EPS) to form a matrix protecting the growth of bacterial colonies. 3) The presence of quorum-sensing molecules enables bacteria to communicate and coordinate biofilm formation based on cell population density (Preda and Săndulescu, 2019) 4) Specific genes and regulatory pathways can help bacteria spread mutated genes against antibiotics and retain biofilm structure. 5) The collective migration of bacteria over surfaces helps bacteria to colonize surfaces, enhancing biofilm development (Elgeti, Winkler, and Gompper, 2015). Finally, a suitable environment for biofilm growth is also essential. Cells inside biofilms are

actively growing and exchanging nutrition and waste with the environment. Therefore, the condition of the environment contributes to the strengthening or weakening of the structure of biofilms (Allen, Habimana, and Casey, 2018; Rupp, Fux, and Stoodley, 2005; Tallawi, Opitz, and Lieleg, 2017).

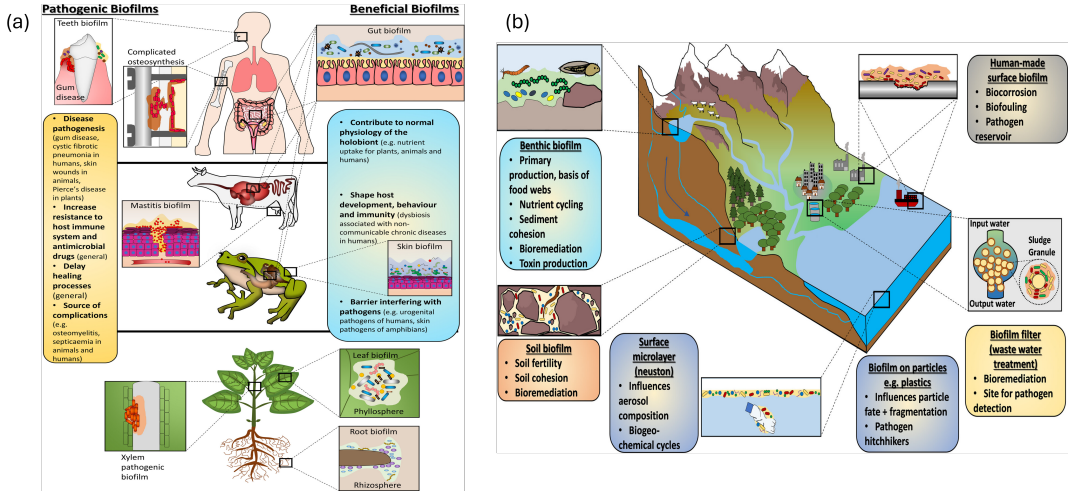

FIGURE 1.12: The effects of biofilm on humans, animals, plants, and ecosystems. (a) The role of biofilm in humans, animals, and plants. They can either be pathogenic(left) or beneficial(right). (b) The significance of biofilm at different land scales. It can occur in terrestrial ecosystems, marine ecosystems, or man-made surfaces such as boats and pipes. The picture is adapted from Sentenac et al., 2022, Functional Ecology (Open Access).

As shown in FIGURE 1.12(a), biofilms are often the roots of persistent infections in various infectious diseases, such as dental plaque on the teeth (Marsh, 2006), chronic wounds resistance to healing (Attinger and Wolcott, 2012), and many others. Also, the biofilms in humans and animals can act as a source to release pathogenic bacteria (because the last stage of biofilm is dispersion, as shown in FIGURE 1.11), and these bacteria can cause inflammation and colonize new tissue (Fleming and Rumbaugh, 2018). For animals, biofilm can cause chronic ear infections in dogs, mastitis in cattle, and etc. (Melchior, Vaarkamp, and Fink-Gremmels, 2006; Moreira et al., 2012; Olson et al., 2002). However, from another perspective, biofilm helps us and animals maintain the functioning of some organs, for example, for us and cows in the gut. However, no antibiotics still could effectively cure biofilm-related infections (Sharma, Misba, and Khan, 2019). Furthermore, for plants, most biofilm on plants are beneficial (Compant et al., 2019; Rodriguez et al., 2019; Vandenkoornhuyse et al., 2015), and they exist in leaf microbiome (Vorholt, 2012) or phyllosphere and root microbiome or rhizosphere (Lynch, 1994). It has also been reported that biofilm influences the ecosystems by preventing the impacts of pollution, cyanobacterial blooms, and synthetic molecules (Mazza, 2016; Lazarova and Manem, 1995; Flemming, Schmitt, and Marshall, 1996; Edwards and Kjellerup, 2013; Wu, 2017; Wu, 2016), also illustrated in FIGURE 1.12(b). Therefore, besides academic interests, studying biofilm brings insights into medicine and environmental protection.

As introduced above, bacteria migrate collectively on the surface inside a biofilm as aggregates. Swimmers, in general, have been observed to have varied collective motility patterns, such as clustering or living crystals, swarming and active turbulence, etc. In the following text, examples and illustrations of these collective motions will be provided.

For a system of active particles, it has been studied theoretically that at the appropriate combination of speed and density, they can form clusters even when interaction between them is purely repulsive (Tailleur and Cates, 2008; Fily and Marchetti, 2012; Redner, Hagan, and Baskaran, 2013), also confirmed in experiments (Buttinoni et al., 2013; Palacci et al., 2013). To explain this, let us assume in a simple case that two particles collide to form a temporary two-particle cluster. The time that the particles stay in this configuration depends on the rotational diffusion time, and the mean time between collisions depends on the speed of particles and the density of particles in the system. Therefore, with the right combination of density and speed, we can achieve that another particle joins this two-particle cluster before it breaks. With the accumulation, massive meta-stable clusters could be formed (Theurkauff et al., 2012; Ginot et al., 2015; Pohl and Stark, 2014; Pohl and Stark, 2015). Such clusters are very dynamic, subject to changes in size and shape, and have been found to have a positive correlation with the activity of particles.

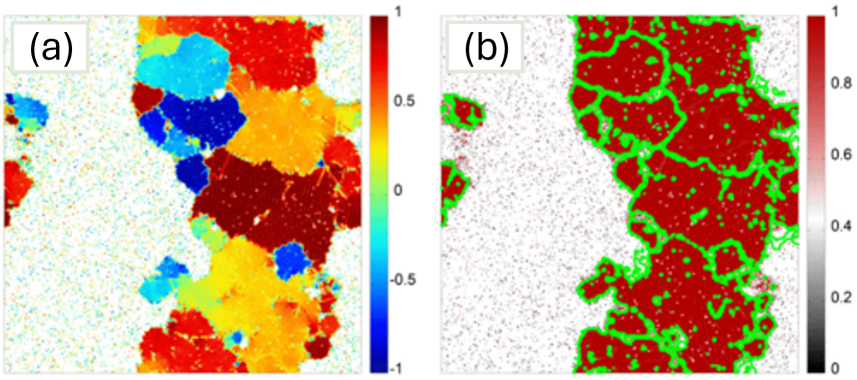

FIGURE 1.13: The illustration of MIPS coexistence region. (a) Different colours represent the different orientations of hexatic phases. (b) The green colour shows the interfaces between the domains with different orientations. The picture is adapted with permission from Digregorio et al., 2018, Physical Review Letters.

Motility-induced phase Separation (MIPS) is characterized by the existence of both low- and high-density phases of active particles; the high-density phase is often found to be a nearly immobile cluster with a size comparable to the size of the system (Palacci et al., 2013; Buttinoni et al., 2013; Liu et al., 2019), illustrated in FIGURE 1.13. The study by Digregorio et al., 2018 performed simulations of Active Brownian Disks (ABD) under varied conditions and, therefore, obtained a phase diagram of the activity of ABDs and packing fraction. FIGURE 1.13 in that work shows the phases with different hexatic orders are highly mobile; they change with time due to the breaking and recombination of blocks (Digregorio et al., 2018).

The collective motion of microswimmers was firstly detected by Mendelson et al., 1999 where they reported a short-lived dynamic pattern of *Bacillus Subtilis*. This is called "active turbulence" later (Wensink et al., 2012; Dunkel et al., 2013), as in the reference to the classical inertial turbulence (Dombrowski et al., 2004; Wolgemuth, 2008), as shown in FIGURE 1.14(a). Similar behavior and pattern have also been found in active bio-filament, which grows in cytoplasm (Sanchez et al., 2012; Doostmohammadi et al., 2017) and growing tissues (Lin et al., 2021; Doostmohammadi et al., 2015). Another common collective motion of microswimmers in biofilm is swarming, seen in FIGURE 1.14(b). The behavior is defined as rapidly migrating bacterial aggregates across a surface (Henrichsen, 1972). Swarming requires interactions between bacteria, surfactant secretion, and a rise in the number of flagella of

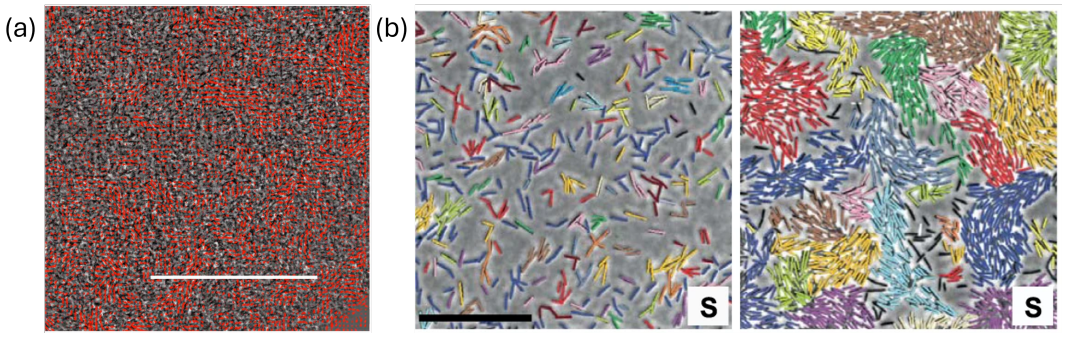

FIGURE 1.14: The experimental illustration of collective motion of bacteria. (a) Active turbulence of wild-type *E. Coli* of strain JEK1036, the red arrows represent the velocity direction. This was done in collaboration with Benjamin Perez at ESPCI Paris; both parties contributed to the work. (b) Snapshots of bacterial swarms in monolayer with different aspect ratios and densities. Colors represent different moving clusters. The scale bar corresponds to $50\mu m$. The snapshot is adapted from (Be'er et al., 2020), Communication Physics (Open Access).

the involved bacteria (Kearns, 2010). Different physical aspects of swarming have been studied, such as surface cell density (Zhang et al., 2010), aspect ratio of cells (Ilkanaiv et al., 2017), flagella number and structure (Courtney, Cozy, and Kearns, 2012; Guttenplan, Shaw, and Kearns, 2013), cell rigidity (Ben-Jacob et al., 2001), interactions between flagella and neighboring cells (Copeland et al., 2010) and others.

Chapter 2

Theoretical Background

2.1 Hydrodynamics

2.1.1 What is fluid?

A fluid is a liquid material that moves continuously and deforms (flows) under external force or applied shear stress. Also, there is no restoring force proportional to the displacement; however, resistance or friction may be present, which is usually proportional to the velocity. Microscopically, constituents of a fluid can move affecting each other and more freely compared to solids. Liquid and gas both can be governed by the equation of fluid dynamics. However, the main difference lies in density, compressibility, and viscosity.

2.1.2 Important dimensionless quantities

- Mach number (Ma) characterises the importance of compressibility. The number is defined as:

$$Ma = \frac{U}{c_s} \tag{2.1}$$

  U is the average flow speed and c_s is the speed of the sound in the fluid. With small Ma, density inhomogeneities of the fluid could be negligible as the unevenness in density could level out very quickly without disturbing the flow pattern. Therefore, we can safely assume the fluid density is a constant $\rho = const.$ under a small value of Ma.

- Reynolds number (Re) quantifies the importance of viscosity and inertia. It has a formula of:

$$Re = \frac{d\rho U}{\eta} = \frac{dU}{\nu} \tag{2.2}$$

  Here, d is the characteristic flow length, ρ is the fluid's density, and U is the flow speed. η is the dynamic viscosity and it has a relation with ν kinematic viscosity as $\nu = \eta/\rho$. Re quantifies the inertial to viscous forces ratio in the fluid (Landau and Lifshitz, 2013). We could neglect inertial effect on an object at a small Reynolds number, helping simplify the Navier-Stokes equation, which will be described in detail later. Some example values of Re include $Re \approx 10^4$ for a swimming human, $Re \approx 10^2$ for a swimming fish, and an object with micro-size typically has Re around 10^{-4} (Purcell, 2014).

2.1.3 Laws of conservation

- **Conservation of mass** (Landau and Lifshitz, 2013): Within a controlled volume V with boundary $A = \partial V$, the number of fluid particles only changes if there

is a net flux in or out the volume. We can represent the mathematical forms step by step:

$$N(t) = \int_v d^3x n(t, \mathbf{x}), \tag{2.3}$$

where $N(t)$ is the number of particles within V and $n(t, \mathbf{x})$ is the particle number density. The net flux $F(t)$ can be presented as:

$$F(t) = \int_{A=\partial V} dA_j n_j(t, \mathbf{x}) = \int_v d^3x \partial_j n_j(t, \mathbf{x}), \tag{2.4}$$

Here, $n_j(t, \mathbf{x})$ are the different component of the particle density with $j = 1, 2, 3$. The second equality is due to Gauss's law. Therefore, the law is written as:

$$\frac{\partial}{\partial t} N(t) + F(t) = \int_v d^3x \{\partial_t n(t, \mathbf{x}) + \partial_j n_j(t, \mathbf{x})\} = 0, \tag{2.5}$$

This equation holds for any volume V, therefore the conservation of the number of particles in local form is:

$$\partial_t n(t, \mathbf{x}) + \partial_j n_j(t, \mathbf{x}) = 0, \tag{2.6}$$

Under non-relativistic physics limit, we can assume $\rho(t, \mathbf{x}) = mn(t, \mathbf{x})$ and $\rho_j(t, \mathbf{x}) = mn_j(t, \mathbf{x})$, where m is the mass of each individual particle. Thus, the conservation of mass is written as:

$$\partial_t \rho + \partial_j \rho_j = 0, \tag{2.7}$$

- **Conservation of energy** (Landau and Lifshitz, 2013): It is defined simiarly to the conservation of mass:

  $$\partial_t \epsilon + \partial_j \epsilon_j = 0 \tag{2.8}$$

  Here $\epsilon(t, \mathbf{x})$ and $\epsilon_j(t, \mathbf{x})$ are the energy density and energy flux density, respectively.

- **Conservation of momentum** (Landau and Lifshitz, 2013): It is derived from Newton's second law. It can be written in terms of the momentum density p_k and momentum flux density p_{jk} by following similar derivation above, then we get:

  $$\partial_t p_k + \partial_j p_{jk} = 0 \tag{2.9}$$

  When the centrifugal forces are absent, momentum flux density must be symmetric, written as $p_{jk} = p_{kj}$, because otherwise strong rotational forces would act on a small fluid volume.

2.1.4 Fluid dynamic equations of motion

Rewriting conservation laws

Since the conservation laws are invariant w.r.t. Galilei boost transformation, it is possible and useful to write the quantities ρ, ρ_j, ϵ, ϵ_j, p_k and p_{jk} in a different form

(Landau and Lifshitz, 2013):

$$\rho = \rho, \tag{2.10}$$
$$\rho_j = \rho u_j, \tag{2.11}$$
$$p_k = \rho u_k, \tag{2.12}$$
$$p_{jk} = \rho u_j u_k + T_{jk}, \tag{2.13}$$
$$\epsilon = \frac{1}{2}\rho \mathbf{u}^2 + e, \tag{2.14}$$
$$\epsilon_j = (\frac{1}{2}\rho \mathbf{u}^2 + e)u_j + u_i T_{ij} + q_i. \tag{2.15}$$

Here, v_j is the fluid velocity field, T_{jk} is a stress tensor, e represents fluid internal energy and q_i is the heat flow. With this we can rewrite the mass conservation law (equation 2.7):

$$\partial_t \rho + u_j \partial_j \rho + \rho \partial_j u_j = 0 \tag{2.16}$$

It is called **continuity equation**, describing the evolution of mass density provided that there is a fluid velocity field v_j. The momentum conservation law can also be reformulated from equation 2.9:

$$\partial_t p_k + \partial_j p_{jk} = \partial_t(\rho u_k) + \partial_j(\rho u_j u_k + T_{jk}) = 0, \tag{2.17}$$

We can simplify this as (Landau and Lifshitz, 2013):

$$\rho(\partial_t + v_j \partial_j) u_k + \partial_j T_{jk} = 0. \tag{2.18}$$

Similarly, the energy conservation law becomes (Landau and Lifshitz, 2013):

$$(\partial_t + u_j \partial_j)\epsilon + \epsilon \partial_j u_j + (\partial_j u_k) T_{jk} + \partial_j q_j = 0. \tag{2.19}$$

Naiver-Stokes equation

Navier-Stokes equation describes the equation of motion of viscous fluid. We will now derive the equation from the conservation laws above.T_{jk} the momentum flux density tensor has the contributions from reversible momentum transport due to the motion of fluid particles, the pressure exerted on the fluid, and the friction between fluid particles resulting in irreversible spreading of momentum, T_{jk} can be written as:

$$T_{jk} = \delta_{jk} p(e, \rho) - 2\eta(e, \rho)\sigma_{jk} - \delta_{jk}\zeta(e, \rho)\partial_i u_i. \tag{2.20}$$

η and ζ are shear and bulk viscosity, respectively (Landau and Lifshitz, 2013). They are functions of two independent thermodynamic variables, e, and ρ. σ_{jk} is the component of a traceless and symmetric tensor with its first order in derivatives of fluid field defined by ρ, e and u_j, it has a formula of $\sigma_{jk} = \frac{1}{2}\partial_j u_k + \frac{1}{2}\partial_k u_j - \frac{1}{3}\delta_{jk}\partial_i u_i$. We plug equation 2.20 to the momentum conservation law (equation 2.18). Then we have the general version of **Navier-Stoke equation** (Landau and Lifshitz, 2013):

$$\rho(\partial_t + u_j \partial_j) u_k + \partial_k p - \partial_j[\eta(\partial_j u_k + \partial_k u_j - \frac{2}{3}\delta_{jk}\partial_i u_i)] - \partial_k(\zeta \delta_i u_i) = 0. \tag{2.21}$$

Note that the equation describes the fluid without any external forces. If we assume that the two viscosity coefficients are constant over the space (e, ρ), then we have:

$$\rho(\partial_t + u_j\partial_j)u_k + \partial_k p - \eta\partial_j\partial_j u_k - (\zeta + \frac{1}{3}\eta)\partial_k\partial_j u_j = 0. \tag{2.22}$$

The equation has 5 unknowns. Even with the continuity equation (equation 2.16) for ρ and the initial and boundary conditions, solving the Naiver-Stokes equation (equation 2.22) analytically is only applicable in some exceptional cases. We have to seek reasonable simplifications. One is that if we assume that fluid is incompressible, then we have:

$$\partial_i u_i = 0 \tag{2.23}$$

This corresponds to the case where the Mach number (Ma) is minimal, explained in section 2.1.2 (Landau and Lifshitz, 2013). By putting this into equation 2.22, we obtain the **incompressible Naiver-Stokes equation** (Landau and Lifshitz, 2013):

$$\partial_t u_k + u_j\partial_j u_k = -\frac{1}{\rho}\partial_k p + \frac{\eta}{\rho}\partial_j\partial_j u_k \tag{2.24}$$

This equation is still not linear, and therefore only solvable in some special cases.

2.1.5 Low Reynolds number

The Reynolds number (Re) introduced in section 2.1.2 quantifies the ratio of inertial forces to viscous forces; both are exerted on an object. For a micro-size swimmer, Re is on the order of 10^{-4} (Purcell, 2014), allowing for further simplifications of the Navier-Stokes equation of an incompressible flow (equation 2.24).

Firstly, for a steady flow, the speed of the flow is constant with time. Therefore, we have:

$$\partial_t u_k = 0 \tag{2.25}$$

We can substitute the equation in equation 2.24, then we obtain:

$$u_j\partial_j u_k = -\frac{1}{\rho}\partial_k p + \frac{\eta}{\rho}\partial_j\partial_j u_k \tag{2.26}$$

In this equation, the term $u_j\partial_j u_k$ has a dimension of $[U^2/d]$ where U is the flow speed, and d is the characteristic flow length. Also, the term $\frac{\eta}{\rho}\partial_j\partial_j u_k$ has a dimension of $[\eta U/\rho d^2]$ (Landau and Lifshitz, 2013). The ratio of the two terms gives the dimension of Re. Thus, under the case where $Re << 1$, we can neglect the term $u_j\partial_j u_k$, and this gives:

$$-\partial_k p + \eta\partial_j\partial_j u_k = 0 \tag{2.27}$$

Together with the condition for incompressibility of fluid $\partial_j = 0$, they can completely determine the motion, subject to appropriate initial and boundary conditions. This equation is called **Stokes equation** (Landau and Lifshitz, 2013). Following this, let us consider the case where a sphere of radius R is slowly moving through an incompressible, viscous, and steady fluid. The drag exerted on the body by the fluid is $F_{drag} \propto \eta R v$, where v is the sphere's speed. The derivation of the drag force can be done by a simple dimensional analysis. The density ρ does not appear in equation 2.27, so F_{drag} is the combination of R, η and v, the only combination is $\eta R v$. By more

vigorous deduction and proof, we can obtain that (Landau and Lifshitz, 2013):

$$F_{drag} = 6\pi\eta Rv \tag{2.28}$$

Generally, for a slow moving body of any shape, the dependence of $\mathbf{F}$ on $\mathbf{v}$ can be written as:

$$F^i_{drag} = \eta a_{ik} v_k \tag{2.29}$$

where a_{ik} is a symmetrical tensor of rank 2 and it is independent of $\mathbf{v}$.

The formula 2.28 is not applicable at large distances where $\mathbf{v} \approx \mathbf{u}$. The term $u_j \partial_j u_k$ can only be neglected (resulting in the equation 2.27 and equation 2.28) if $r << u/v$ where r is the distance from the center of the sphere. Further away from the sphere, we have the equation:

$$v_j \partial_j u_k = -\frac{1}{\rho}\partial_k p + \frac{\eta}{\rho}\partial_j \partial_j u_k \tag{2.30}$$

This is so-called **Oseen equation** (Oseen, 1910). The drag force is therefore:

$$F_{drag} = 6\pi\eta vR(1 + 3vR/8u) \tag{2.31}$$

where $Re = vR/u$. The equation also includes the next term in the expansion of drag force in the power of Re. It is important to note that Oseen's equation refines the picture of the flow at a distance further away from the sphere. We can see that in the limit of $Re \to 0$, we obtain the Stokes' formula shown in equation 2.28.

2.1.6 Hydrodynamic interactions

The hydrodynamic interactions induced by the flow field between the bodies immersed in the same fluid are important for our studies. The force on a unit surface area with its surface normal pointing inwards is given by $f_k = -\sigma_{kj} n_j$ (Landau and Lifshitz, 2013), provided a boundary condition of that the velocity of fluid particles at the surface of the objects is equal to the velocity of the surfaces; in other words, a non-slip boundary condition. Therefore, the overall force on a body of volume V and surface area ∂_V moving at velocity of $\mathbf{v}(t)$ is given by:

$$F_i = -\oint_{\partial V} dn_j \sigma_{ij}, \tag{2.32}$$

$$\mathbf{u}(\mathbf{r})|_{\mathbf{r}\in\partial V} = \mathbf{v}(t). \tag{2.33}$$

Together with Stokes' equation (equation 2.27), they can describe a complete picture of the behavior in a low-Reynolds-number regime. The equations cannot be solved directly; however, for an unbounded system with an external force field $\mathbf{f}(\mathbf{r}, t)$, the Stoke's equation (equation 2.27)is changed into:

$$-\partial_k p + \eta \partial_j \partial_j u_k = -f_k(r_k, t). \tag{2.34}$$

The equation can be solved by Fourier transform in the reciprocal space. The result in the real space is:

$$u_i(\mathbf{r}) = \int d\mathbf{r}' H_{ik}(\mathbf{r} - \mathbf{r}') f_k(\mathbf{r}'), \tag{2.35}$$

Where $\mathbf{H}(\mathbf{r}-\mathbf{r}')$ is Oseen tensor, and it has a formula in Cartesian components of (Dhont, 1996; Español and Warren, 1995):

$$H_{ij}(\mathbf{r}) = \frac{1}{8\pi\eta r}[\sigma_{ij} + \frac{r_i r_j}{r^2}]. \tag{2.36}$$

where $i, j \in \{x, y, z\}$ and $r = |\mathbf{r}|$. It shows that hydrodynamic interactions decay as $1/r$ (long range). Also, the Oseen tensor (equation 2.36) is the Green's function of the Stokes' equation with external forces (equation 2.34). When the force field is a point force $\mathbf{f}(\mathbf{r}, t) = \delta(\mathbf{r})\hat{\mathbf{e}}$ where $\hat{\mathbf{e}}$ is the unit vector in the direction of the force application. Then the equation becomes:

$$u(\mathbf{r})_i = \frac{1}{8\pi\eta r}[\hat{e}_i + \frac{r_j \hat{e}_j r_i}{r_k r_k}] \tag{2.37}$$

The equation diverges at $r \to \infty$, which is due to the omission of inertia in the Stokes equation.

2.2 Diffusion and transport

2.2.1 Diffusion: Fick's laws

Let us imagine a pipe of water. A small quantity of dye is placed inside the pipe, allowing it to diffuse in both directions along the pipe. It is common sense to know that the dye diffuses from regions of higher concentration to regions of lower concentration. We assume the concentration profile of the dye at position x of the pipe is $C(x, t)$ with a unit of m^{-1}. Also, we define a quantity flux J, which is the number of atoms passing through unit area of a cross-section per unit time. We assume the quantity J is proportional to the concentration gradient of the pipe; we thus have:

$$J = -D\frac{\partial C}{\partial x}. \tag{2.38}$$

Where $D > 0$ and it has a unit of $[m^2/s]$ and is called diffusion coefficient (Paul et al., 2014). The minus sign indicates that the flux direction is opposite the concentration gradient. This equation is called the **Fick's first law** (Paul et al., 2014).

Now consider a small segment from x_1 to x_2 of the pipe. It is easy to get that the rate of change of the dye atom numbers is given by:

$$\frac{dn}{dt} = J(x_1, t) - J(x_2, t), \tag{2.39}$$

where n is the number of the dye particles within the segment and it has an expression of $n = C(x, t)\Delta x$ ($\Delta x = x_2 - x_1$). We can therefore write as:

$$\frac{\partial C(x,t)}{\partial t}\Delta x = D(\frac{\partial C(x_2,t)}{\partial t} - \frac{\partial C(x_1,t)}{\partial t}), \tag{2.40}$$

The right hand side of the equation is due to the substitution of Fick's first law (equation 2.38). Then we can divide by Δx both sides, we have:

$$\frac{\partial C}{\partial t} = D\frac{\partial^2 C}{\partial x^2} \tag{2.41}$$

This is the **Fick's second law** (Paul et al., 2014).

2.2.2 Brownian motion

As introduced in the Introduction, "Brownian Motion" was observed by Robert Brown and then theorized by Albert Einstein in 1905. Brownian particles are also called colloids suspended in a medium such as liquid or gas. To model the motion, a few quantities are needed: the position of the particle $\boldsymbol{r}$, the velocity $\boldsymbol{v}$, the friction due to fluid acting on the particle $-\gamma\boldsymbol{v}$ where γ is the friction coefficient, a random force $\boldsymbol{\xi}$ for thermal fluctuation and a conservative potential U. Therefore, the Langevin equation is:

$$m\dot{\boldsymbol{v}} = -\gamma\boldsymbol{v} - \nabla U(\boldsymbol{r}) + \boldsymbol{\xi}(t). \tag{2.42}$$

The random force models the perpetual thermal fluctuations of fluid molecules, and it is often referred to as "white noise". In other words, the force is isotropic, uncorrelated, and Gaussian distributed (Stancil, 2012). The force in a system of d dimensions at the temperature of T can be realized by:

$$\langle \boldsymbol{\xi}(t_1) \cdot \boldsymbol{\xi}(t_2) \rangle = 2dk_B T\gamma\delta(t_1 - t_2), \tag{2.43}$$

$$\langle \boldsymbol{\xi}(t) \rangle = 0, \tag{2.44}$$

Here, the first equation represents a relation between the magnitude of driving fluctuations and the magnitude of frictional dissipation, and it has the name of **fluctuation-dissipation theorem** (Zwanzig, 2001). In the case of a constant potential $U = const.$ It is easy to see that the particle does not show a positive net displacement $\langle \boldsymbol{r} \rangle = \boldsymbol{r}(t_0)$; however, the particle explores the space by the thermal fluctuations. A quantity called mean square displacement (MSD) is used to quantify the motion. MSD can be written as $\langle \Delta r^2 \rangle$, in which $\Delta\boldsymbol{r} = \boldsymbol{r}(t) - \boldsymbol{r}(t_0) = \int_{t_0}^{t} dt' |\boldsymbol{v}(t')|$. MSD has an expression of:

$$\langle \Delta r^2 \rangle = 2d\frac{k_B T}{\xi}(t - \frac{m}{\xi} + \frac{m}{\xi}e^{-\xi t/m}), \tag{2.45}$$

If we look at different limits in time, we can simplify the expression:

$$\langle \Delta r^2 \rangle \approx \begin{cases} 2d\frac{k_B T}{\gamma}t, & t \gg \frac{m}{\gamma} \\ d\frac{k_B T}{\gamma}(\frac{t}{m/\gamma})^2, & t \ll \frac{m}{\gamma} \end{cases} \tag{2.46}$$

Here, we can see that there are two regimes of approximation. When $t \ll m/\gamma$, $\langle \Delta r^2 \rangle \propto t^2$, the particles move ballistically. When $t \gg m/\gamma$, the momentum of the particles is transferred to the fluid via friction, the particles' motion is now in the so-called diffusive regime and $\langle \Delta r^2 \rangle \propto t$. In this regime, the Fick's law can be applied to describe the dynamics of fluid (Section 2.2.1), where D in Fick's law (equation 2.38) has a form of

$$D = \frac{k_B T}{\gamma} = \frac{k_B T}{8\pi\eta R} \tag{2.47}$$

This equation is called **Stokes-Einstein equation**, and it links the diffusion coefficient with the strength of the thermal fluctuation and the friction, which is indicated in equation 2.28. For the rotational Brownian motion, the orientation vector of the colloids $\hat{e}$ relaxes following an exponential decay, written as:

$$\langle \hat{e}(t) \cdot \hat{e}(t_0) \rangle = e^{-t/\tau_R} \tag{2.48}$$

Where τ_R is the lifetime of the exponential decay of the rotational diffusion $\tau_R = 1/D_R$ and D_R indicates the rotational diffusion coefficient. The friction force ξ_R becomes $\gamma_R = 8\pi\eta R^3$ rather than in equation 2.28. The rotational diffusion coefficient D_R has a formula:

$$D_R = \frac{k_B T}{\gamma_R} = \frac{k_B T}{8\pi\eta R^3} \tag{2.49}$$

This is sometimes referred to as **Stokes–Einstein–Debye relation** (Zwanzig, 2001).

2.2.3 Active Brownian motion

The motion of Brownian particles is predicted by equilibrium statistical mechanics where equipartition and fluctuation-dissipation theorem can be applied. However, driving the motion of Brownian particles out of equilibrium leads to new and exciting phenomena (Bunde et al., 2017; Falasco et al., 2014; Rings et al., 2010). The physics of colloids out-of-equilibrium is different because two parts need to be considered: thermal fluctuation and active driving within the agents. One of the models is "Active Brownian Particles (ABP)." In this chapter, we will introduce its definitions and fundamental theories. We can see how it is different from the motion of Brownian Particles. The motion of an ABP particle can be described as:

$$\dot{\mathbf{r}}(t) = v_0\hat{\boldsymbol{e}}(t) + \frac{1}{\gamma}\boldsymbol{\xi}(t), \tag{2.50}$$

Where the particle is subject to fluctuating and overdamped forces, it has a constant speed of v_0, and its orientation vector is $\hat{\boldsymbol{e}}(t)$ (Das, Gompper, and Winkler, 2018). The random force $\boldsymbol{\xi}(t)$ is subject to the same conditions as in equation 2.43. The orientation vector $\hat{\boldsymbol{e}}(t)$ is subject to the rotational Brownian motion. Similarly, we can calculate the mean square displacement for ABP from equation 2.50 and equation 2.48, giving:

$$\langle \Delta r^2 \rangle = 2dDt + 2v_0^2\tau_r^2\left(\frac{t}{\tau_r} + e^{-t/\tau_r} - 1\right), \tag{2.51}$$

By taking three limits of time we have:

$$\langle \Delta r^2 \rangle \approx \begin{cases} 2dD_R t, & t \to 0 \\ v_0^2 t^2, & 0 \ll t \ll \tau_r \\ 2(dD_R + v_0^2\tau_r)t, & t \gg \tau_r \end{cases} \tag{2.52}$$

The particles have diffusive motion at the small time scale; at the intermediate scale, particles move ballistically. Once $t \gg \tau_r$, ABPs present diffusive diffusion again but with an increased diffusion coefficient by its activity. Therefore, the transition time from ballistic to diffusive regime of diffusion τ_r can be determined by analyzing the autocorrelation function of the orientation vector $\hat{\mathbf{e}}(t)$ as in equation 2.48.

To characterize the ratio of advective and diffusive time scales, a quantity called *Pe* number defines how much the active propulsion of an ABP compared to its rotation, and it has a form of (Das, Gompper, and Winkler, 2018):

$$Pe = \frac{v_0}{2RD_R} \tag{2.53}$$

For an ABP with a radius of R and speed of v_0. *Pe* can also be applied and measured for microswimmers, for example, *E. Coli* has a *Pe* value of around 100 (Bianchi, Saglimbeni, and Di Leonardo, 2017).

2.3 Physics of micro-swimmers

As introduced in the Introduction, microorganisms are ubiquitous on Earth. They are abundant in varieties and evolved self-propulsion mechanisms to explore their environment and colonize new places. Their exploration is frequently facilitated by active reorientation driven by intricate internal processes that exhibit temporal dependence. Even though the scientific community has understood the hydrodynamics of their motion in Newtonian fluids, their interactions with the environment, such as walls, obstacles, and non-Newtonian fluids, remain less understood. In this chapter, we will first introduce some fundamental theories of microswimmers; then, we will focus on the behavior of *E. Coli* and finally, we will introduce the collective motion of swimmers.

2.3.1 Far-field hydrodynamics: Dipole swimmer

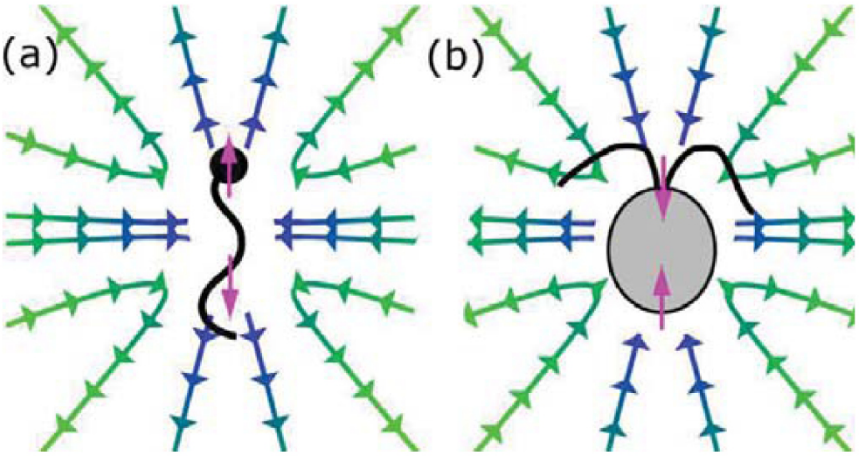

FIGURE 2.1: Illustrations of the flow field of dipolar swimmers (a) pusher (b) puller. The pictures are adapted with Permission from Elgeti, Winkler, and Gompper, 2015, IOP Science.

Most swimmers can move freely in a fluid, which means that the external forces applied to the fluid are zero and vice versa. In the literature by Ishikawa, Locsei, and Pedley, 2008; Lauga and Powers, 2009, they proposed to use "force-dipole" to explain the far-field dynamics of the swimmers(such as bacteria, algae, or spermatozoa) at a distance away from the swimmer larger than the swimmer's size. Based on the flow field, the swimmers can be classified into two classes: "pusher" and "puller," shown in FIGURE 2.1. The pushers have their motors at the back while the pullers are in the front; notably, this has also been observed in experiments (Drescher et al., 2011), for example, *E. Coli* is a pusher, while algae *Chamydomonas Reinhardtii* is a puller. As shown in FIGURE 2.1, the flow field is very similar except for the opposite flow direction. This draws a very significant difference when calculating the swimmers' interactions within a pair or with a wall. Consider that a pusher swimmer in the form of a force dipole is located at $\mathbf{r}_0$. The flow field $\mathbf{u}_{fd}$ at the distance $\mathbf{r}$ from the swimmer can be formulated from the Oseen tensor (equation 2.36) as:

$$\mathbf{u}_{fd}(\mathbf{r}) = \frac{f_0 d}{8\pi\eta r^3}\Big[-1+3(\mathbf{r}\cdot\hat{\mathbf{r}})^2\Big]\hat{\mathbf{r}} \tag{2.54}$$

Here, we define the two points of forces located at $\mathbf{r} = \mathbf{r}_0 \pm 1/2\mathbf{d}$ where $\mathbf{d} = d \times \hat{\mathbf{e}}$ with the two forces at two opposite directions of $\mathbf{f}_0 = \pm f_0 \hat{\mathbf{e}}$ (Elgeti, Winkler, and Gompper, 2015). Also, $P = f_0 d$ is the dipole strength; here, for pusher, $P > 0$, while for puller $P < 0$. Compared to equation 2.37 where a force monopole is considered, for which the flow field decays as $1/r$, u_{fd} decays much faster as $1/r^2$.

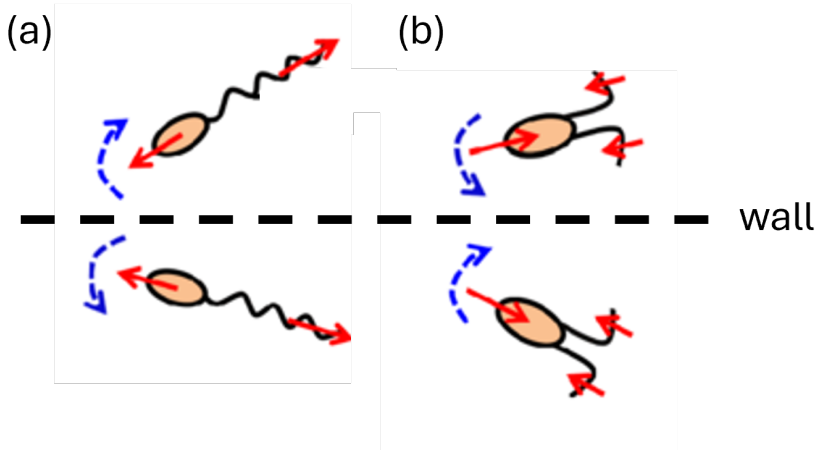

FIGURE 2.2: Illustration of the orientation of a swimmer-pair. (a) Pusher-pusher pair (b) Puller-puller pair. When there is no wall, the pushers prefer a parallel orientation to each other and the swimming direction, while pullers tend to orient themselves perpendicular to the swimming direction. When a wall is present, by far-field approximation, the relative orientation of a wall is analyzed through mirror images. Therefore, in (a), pushers like swim parallel to the wall while in (b) pullers like swim along the wall normal. Adapted with permission from Lauga and Powers, 2009, IOP Science.

Particle-particle interactions

Dipolar flow fields also have a vorticity associated with it, formulated as:

$$\Omega(\mathbf{r}) = \nabla \times \mathbf{u}_{fd}(\mathbf{r}) = \frac{3P}{4\pi\eta r^3}(\hat{\mathbf{e}} \cdot \hat{\mathbf{e}})(\hat{\mathbf{e}} \times \hat{\mathbf{e}}) \tag{2.55}$$

This expression means that two swimmers at close distance will orient each other by the advection produced by the neighboring swimmer. When the vorticity vanishes, there are two solutions: $\hat{\mathbf{e}} \cdot \hat{\mathbf{e}} = 0$ or $\hat{\mathbf{e}} \times \hat{\mathbf{e}} = 0$, the two equilibrium orientations. For $\hat{\mathbf{e}} \cdot \hat{\mathbf{e}} = 0$, the swimming direction is perpendicular to the dipole direction, this is only stable for pushers ($P > 0$); for $\hat{\mathbf{e}} \times \hat{\mathbf{e}} = 0$, the swimming direction is parallel to the dipolar direction, where only pullers can be stable ($P < 0$). Therefore, when two pushers are on a converging path, they re-orient each other in a configuration that they swim in parallel and side by side. However, if pullers move on a diverging course, the vorticity will orient them to a configuration where they are anti-parallel, swim away, and head-to-toe. These are illustrated in FIGURE 2.2.

Particle-Wall interactions

Considering a planar slip wall at $z = 0$, the force dipole has a mirror image symmetrical w.r.t the wall (FIGURE 2.2). The force dipole of the mirror image has a dipole direction of $\hat{\mathbf{e}}'$ and is centered at $\mathbf{r}_0' = (x_0, y_0, -z_0)$ [Also, $\mathbf{r}_0 = (x_0, y_0, z_0)$], where

$z_0 > 0$. The flow field at the wall is the result of the hydrodynamical interactions of the force dipole and its image. To express the flow field at the wall in the z-direction, we have the expression:

$$u^z_{fd,w}(z_0) = -\frac{P}{32\pi\eta z_0^2}[1 - 3(\hat{\mathbf{e}} \cdot \hat{\mathbf{e}}_z)^2] \tag{2.56}$$

where $\hat{\mathbf{e}}_z$ is the unit vector in z direction. This equation shows that pushers are attracted to the wall. It is easy to deduce that pullers are repelled from the wall since $P < 0$ for pullers. For the non-slip walls, as shown in (Berke et al., 2008), the analytical solution is very similar compared to equation 2.56, except that the pre-factor is $-P/48\pi\eta z_0^2$.

As discussed previously, pushers interact and re-orient each other to swim in parallel side by side, while two pullers swim in antiparallel and away from each other. By applying similar thinking of using mirror images concerning the wall, it is easy to deduce that the flow will attract the pushers to the wall and align their swimming direction with the wall surface. At the same time, the pullers have a stable swimming direction along the wall-normal, leading to attraction between the images shown in FIGURE 2.2.

It's crucial to emphasize that far-field hydrodynamics alone does not fully describe particle-particle and particle-wall interactions. The important role of near-field effects, steric interactions, and Brownian rotational diffusion, as demonstrated by Kantsler et al., 2013, significantly contributes to our understanding of swimmer orientation.

2.3.2 Self-propulsion mechanism of microswimmers

In section 2.1.5, we have shown that in the case of low-Reynolds-number fluid (incompressible viscous and steady flow), we predict the flow by solving Stokes equation (equation 2.27). Consider a solid object embedded, in a fluid, and an external force is applied on it to drag it through this fluid. The boundary conditions to the flow field are given by:

$$\boldsymbol{u} = \boldsymbol{v} + \boldsymbol{\omega} \times \boldsymbol{r} \tag{2.57}$$

Where $\mathbf{v}$ and $\boldsymbol{\omega}$ are the translational and rotational velocity of a particle at location $\mathbf{r}$ on the body. In order to get the force $\mathbf{F}$ and torque $\mathbf{T}$ acting on the object, the stress tensor $\boldsymbol{\sigma} = \eta(\nabla\mathbf{u} + \nabla\mathbf{u}^T)$ is integrated over the object surface S and then we obtain:

$$\mathbf{F} = \oint_S \boldsymbol{\sigma} \cdot \hat{\mathbf{n}} dS, \tag{2.58}$$

$$\mathbf{T} = \oint_S \mathbf{r} \times \boldsymbol{\sigma} \cdot \hat{\mathbf{n}} dS. \tag{2.59}$$

Here, $\hat{\mathbf{n}}$ is the unit surface normal vector (Bechinger et al., 2016). Also, swimmers are force-free and torque-free. With the linearity of the Stokes equation, we can write:

$$\begin{bmatrix} \mathbf{F} \\ \mathbf{T} \end{bmatrix} = \begin{bmatrix} \mathbf{A} & \mathbf{B} \\ \mathbf{B}^T & \mathbf{D} \end{bmatrix} \begin{bmatrix} \mathbf{v} \\ \boldsymbol{\omega} \end{bmatrix} \tag{2.60}$$

In this equation, $\mathbf{A}$, $\mathbf{B}$, $\mathbf{B}^T$, and $\mathbf{D}$ are the tensors determining the orientation and shape of the object. $\mathbf{A}$ and $\mathbf{D}$ are the tensors related to the pure motion of translation and rotation with a translational velocity of $\mathbf{v}$ or $\boldsymbol{\omega}$, respectively. $\mathbf{B}$ and $\mathbf{B}^T$ represent the coupling between the translational and rotational motion (Bechinger et al., 2016).

Generally, **A** and **D** are not isotropic, and **B** and $\mathbf{B}^T$ do not vanish. One example of the swimmers possessing chiral bodies (they do not have three mutually orthogonal planes of symmetry) can move by self-propulsion with a thrust force of $\mathbf{B} \cdot \boldsymbol{\omega}$. However, this does not happen for a spherical swimmer as its $\mathbf{B} = \mathbf{B}^T = \mathbf{0}$.

For the tensors **A** and **B**, the analytical solution with or without simplifications only exists in a few cases (Lighthill, 1976; Kim and Karrila, 2005; Rodenborn et al., 2013). Here, we focus on the case of the helical propeller, which is possessed by many bacteria, such as *E. Coli*. During the run stage of an *E. Coli* swimming, the helical flagella form a bundle and act as a helical propeller, driving the fluid behind, therefore pushing the body forward. The theoretical estimation of the resistance coefficient of such swimmers has been shown in Rodenborn et al., 2013; corresponding experimental measurements can also be found in Chattopadhyay et al., 2006; Bianchi et al., 2015.

We can calculate the translational and rotational speed from the tensor **A** and **B** of an *E. Coli* by assuming that it consists of two connected rigid bodies, and they rotate at different speeds along a common axis. We also assume that the speed component on the common axis is non-zero while other components vanish. We can thus write the equation 2.60 in a scalar form:

$$F_b = A_b v, \tag{2.61}$$

$$F_f = A_f v + B_f \omega. \tag{2.62}$$

b and f denote "body" and "flagella bundle," respectively. During swimming, no external force is applied to the body; we have $F_b + F_f = 0$, and we can rewrite the equation and obtain the formula of speed v:

$$v = \frac{B_f \omega}{A_b + A_f}. \tag{2.63}$$

The same ideas can be applied to obtain the rotational speed ω provided that no external torque is acting on the object. We obtain:

$$\omega = \frac{B_f v}{D_f + D_B}. \tag{2.64}$$

Generally, there are two mechanisms for self-propelling particles to impose boundary conditions on the flow field (Bechinger et al., 2016): 1) Some swimmers modify their shape and displace the fluid with sticky boundary conditions. 2) The others impose a tangential slip velocity on the surface, like squirmers, which will be introduced below. It is essential to note that the fundamentals of self-propulsion lie in the shape deformation of swimmers, which is cyclic but not reciprocal during the period of the propulsion motion. Lauga and Powers, 2009 show that Stokes equation has no explicit dependence on time, so if the shape deformation is reciprocal, the net displacement $\int_0^T \boldsymbol{v} dt$ is 0 after a period of shape deformation.

2.3.3 Theoretical models of microswimmers

This chapter will introduce some generic microswimmer models which can capture the essential swimming aspects. From one side, these models help to resolve the

mechanism of interactions. Furthermore, with simplified model, the study of interactions within a large system is much more accessible. Three models will be introduced, however, within these, the squirmer model will be emphasised as it serves as the basis for one chapter of the Results.

Purcell swimmer

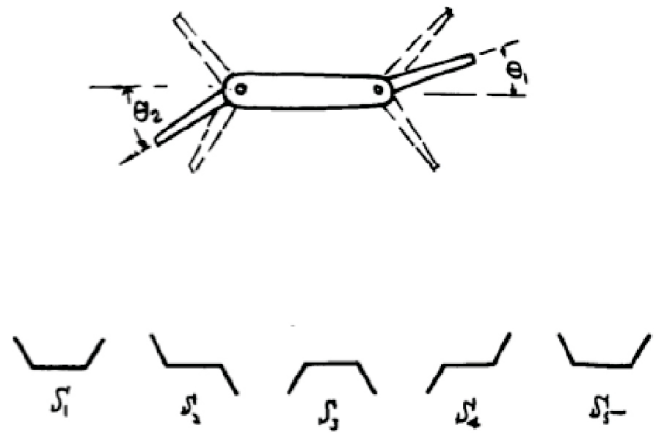

FIGURE 2.3: Illustration of Purcell swimmer which is composed of three connected rod side by side and they can be tilted with respect to each other. At the bottom, it shows the reciprocal temporal sequence of the forward movement of the swimmer. Adapted with permission from Purcell, 1977; Elgeti, Winkler, and Gompper, 2015. The original picture is from Purcell, 1977, Biophysical Journal (Open Access); the picture was then reproduced by Elgeti, Winkler, and Gompper, 2015, IOP Science. The picture included within the thesis is adapted with permission from Elgeti, Winkler, and Gompper, 2015, IOP Science

Purcell, in 1977, proposed a model by considering a swimmer made up of three rigid segments connecting side-by-side by two joints (Purcell, 1977), as shown in FIGURE 2.3. He realized that the swimmer can move forward at low-Reynolds-number fluid when the two angles vary periodically in time but break time-reversal symmetry.

Three-bead swimmer

The three-bead swimmer model was proposed in Najafi and Golestanian, 2004 and consists of three spheres linked together by two rigid rods whose lengths can be varied between two values. A periodic motion is imposed on them so that the time-reversal and translation symmetry is broken. The 1D swimmer can, therefore, swim forwards under low-Reynolds-number conditions. The ideas of the model are similar to the Purcell swimmer; however, some literature reports that the model allows a theoretical solution and the properties of the swimmer can even be solved analytically (Najafi and Golestanian, 2004; Alexander, Pooley, and Yeomans, 2008).

Squirmer model

Squirmer model represents a microswimmer by an active particle with spherical or spheroidal shape with slip velocity on the surface (Lighthill, 1952; Blake, 1971;

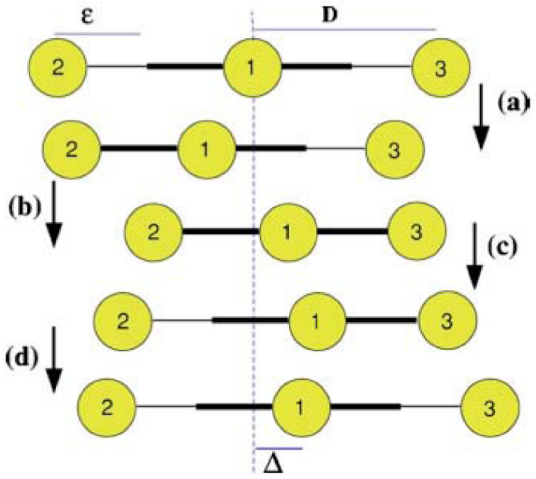

FIGURE 2.4: Illustration of a three-bead swimmer and its moving sequence. The three beads are connected by two rigid rods; the swimmer swims forward when the distance between the spheres varies cyclically with time. In one cycle, the swimmer moves a distance of Δ, and it is also essential that the cycle breaks time-reversal symmetry. The picture is adapted with permission from Najafi and Golestanian, 2004, Physical Review E.

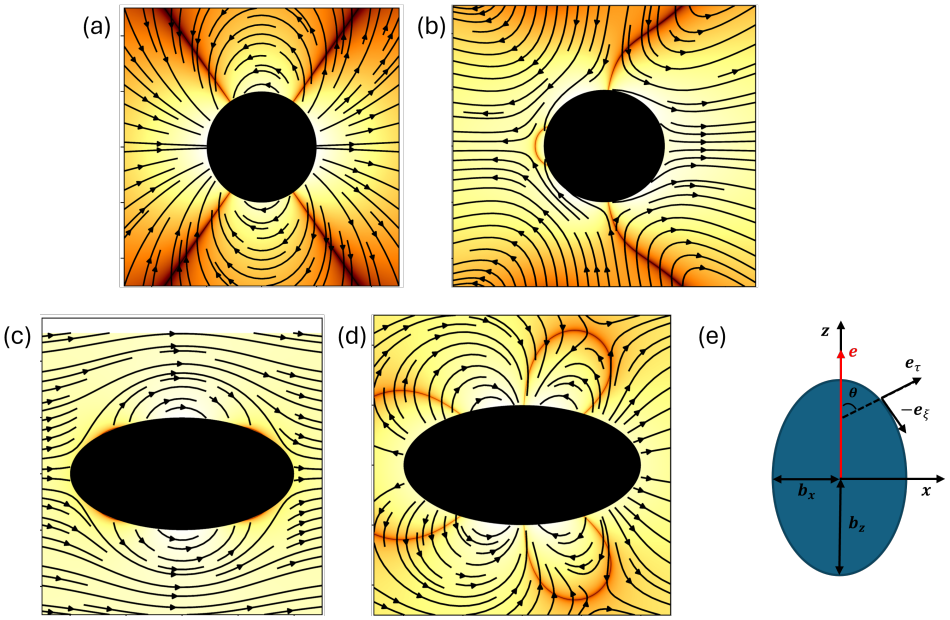

FIGURE 2.5: Flow field of spheroidal (a-b) and spherical squirmers (c-d) with $\beta = 0$ [neutral, for (a) and (c)] and with $\beta = 5$ [pusher for (b) and (d)] in laboratory frame. The spheroidal swimmer has a aspect ratio of 2. The magnitude of the velocity field is coded the color. (e) Schematic of a spheroidal squirmer model. The orientation vector $\boldsymbol{e}$ is aligned with the squirmer's major $z-$axis, b_x and b_z label the minor and major radii of the spheroid, respectively. $\boldsymbol{e}_\tau$ and $\boldsymbol{e}_\zeta$ denote the local normal and tangential unit vectors. (e) is adapted from Wu-Zhang, Fedosov, and Gompper, 2024, Soft Matter (Own work).

Theers et al., 2016a). Initially, the model was only proposed for spherical swimmers with active cilia covering the whole body, such as *Volvox Carteri* (Lighthill, 1952; Blake, 1971). The synchronized beating of cilia also displaces fluid behind

during the movement, leading to a velocity difference between the surface and the fluid around (slip velocity). Despite its simplicity, the model can capture different swimming modes, such as neutral microswimmers (*Paramecium*), pullers (*Chlamydomonas*), and pushers (*E. Coli*), as described in section 2.3.1. Also, the far-field and near-field hydrodynamics of realistic microswimmers can be described well with this simple model.

For a spherical squirmer with a radius of R, the slip velocity $\mathbf{u}_{sq}$ is given by:

$$\mathbf{u}_{sq}(\mathbf{r}_s, \hat{\mathbf{e}}) = \sum_{n=1}^{\infty} B_n \frac{2}{n(n+1)} \left(\frac{\hat{\mathbf{e}} \cdot \mathbf{r}_s}{R} \frac{\mathbf{r}_s}{R} - \hat{\mathbf{e}}\right) P_n'\left(\frac{\hat{\mathbf{e}} \cdot \mathbf{r}_s}{R}\right) \tag{2.65}$$

Here, $\mathbf{r}_s$ denotes the position of the point on the surface with respect to the center, $\hat{\mathbf{e}}$ is the instantaneous orientation vector, B_n is the magnitude of the n^{th} mode and $P_n'(cos\theta)$ is the derivative of the n^{th} Legendre polynomial (Blake, 1971). Quite often, two modes of the expansion of equation 2.65 are usually considered, resulting in two coefficients of the amplitudes B_1 and B_2. People often define $\beta = B_2/B_1$, which characterizes the swimming modes of squirmers: Neutral for $\beta = 0$, puller for $\beta > 0$, and pusher for $\beta < 0$. Furthermore, the coefficient B_1 determines the swimming speed of the squirmer: $U_0 = 2B_1/3$ (Ishikawa, Simmonds, and Pedley, 2006). The flow field of the spherical swimmers with $\beta = 0$ (neutral) and 5 (puller) is shown in FIGURE 2.5(a-b). The flow field of pusher swimmer is very similar with the puller's [FIGURE 2.5(b)], except that the directions of arrows are opposite.

However, many swimmers do not have a spherical shape, such as *E. Coli* and *Chlamydomonas*. Therefore, some literature proposed squirmers with a prolate-spheroidal shape (Keller and Wu, 1977; Ishimoto and Gaffney, 2013). However, these models cannot be solved analytically or provide the complete picture of hydrodynamic interactions. More recently, the spheroidal squirmer model proposed by our group (Theers et al., 2016b) incorporates the force-dipole model as mentioned in section 2.3.1 and has a significant advantage that the flow field can be calculated analytically, shown in FIGURE 2.5(c-d).

Consider a spheroidal-shaped squirmer with the length of the semi-major axis b_z and semi-minor axis as $b_x = b_y$; the slip velocity has a form of:

$$\mathbf{u}_{sq} = -B_1(\mathbf{e}_\zeta \cdot \mathbf{e}_z)(1 + \beta\zeta)\mathbf{e}_\zeta \tag{2.66}$$

where $\mathbf{e}_z$, $\mathbf{e}_\zeta$, and $\mathbf{e}_\varphi$ are unit vectors in spheroidal (ζ, τ, φ) coordinates (FIGURE 2.5(e)), they can be converted into Cartesian coordinates (x, y, z) as:

$$x = c\sqrt{\tau^2 - 1}\sqrt{1 - \zeta^2}\cos\varphi, \tag{2.67}$$

$$y = c\sqrt{\tau^2 - 1}\sqrt{1 - \zeta^2}\sin\varphi, \tag{2.68}$$

$$z = c\tau\zeta. \tag{2.69}$$

Here, $c = \sqrt{b_z^2 - b_x^2}$, and the spheroidal coordinates have the ranges $-1 \leq \zeta \leq 1$, $1 \leq \tau < \infty$ and $0 \leq \varphi < 2\pi$. Similarly, β defines the swimming mode of a squirmer, and it can either be a pusher, neutral, or puller. Also, B_1 determines the swimming speed due to the self-propulsion, and it can be formulated as:

$$U_0 = B_1\tau_0(\tau_0 - (\tau_0^2 - 1)\coth^{-1}\tau_0) \tag{2.70}$$

where $\tau_0 = b_z/c$ and $c = \sqrt{b_z^2 - b_x^2}$ (Theers et al., 2016b; Qi et al., 2020). Based on this

model, Qi et al., 2022proposed an extra term of a rotlet dipole for the slip velocity in equation 2.66, and it mimics a counter-rotating flow field of a single squirmer, which has been indeed being observed in the flow field of some bacteria such as *E. Coli* (Hu et al., 2015a), as their body and flagella bundle rotate in opposite directions. The form and effect of the rotlet dipole term will be mentioned more specifically in the corresponding Results chapter.

Given the model's simplicity, it has been applied in a variety of cases, notably in the study of collective behavior of microswimmers in quasi two-dimensional (2D) systems (i.e., a monolayer of swimmers) (Theers et al., 2018; Qi et al., 2022; Kuhr, Rühle, and Stark, 2019; Kyoya et al., 2015; Alarcón, Valeriani, and Pagonabarraga, 2017; Zöttl and Stark, 2014; Yoshinaga and Liverpool, 2017; Blaschke et al., 2016) and in three-dimensional (3D) settings with periodic boundary conditions (BCs) (Ishikawa and Pedley, 2007; Delmotte et al., 2015; Ishikawa, Locsei, and Pedley, 2008; Evans et al., 2011; Alarcón and Pagonabarraga, 2013); the behavior in external flow (Zöttl and Stark, 2012; Pagonabarraga and Llopis, 2013).

2.3.4 E. Coli: a model bacterium

E. Coli being a pusher

We have mentioned that *E. Coli* is a perfect example of a pusher in section 2.3.1. Here, I want to give a detailed explanation for that. The flagellated swimming enables the rotating flagella bundle to push the fluid behind, while an opposite force is generated on the body, and this force pushes fluid along the swimming direction. Therefore, the flow field of *E. Coli* is the fluid flowing forward and backward in the swimming direction while a lateral flow comes in, ensuring the conservation of mass, as shown in FIGURE 2.5(d). Being a pusher swimmer is a fundamental reason why *E. Coli* can have many interesting biological phenomena, such as swimming at a solid surface(Lauga, 2016; Hartmann et al., 2019; Costerton et al., 1987; Frymier et al., 1995; Bianchi, Saglimbeni, and Di Leonardo, 2017), active turbulence(Wioland et al., 2013; Martinez et al., 2020; Guo et al., 2018b; Wensink et al., 2012; Stenhammar et al., 2017; Bárdfalvy et al., 2019; Qi et al., 2022; Lushi, Wioland, and Goldstein, 2014; Theillard, Alonso-Matillaa, and Saintillan, 2017), and others. These will be discussed in more detail later in this chapter.

Run-and-tumble exploration

As mentioned in the Introduction, *E. Coli* samples the environment with a strategy of "run and tumble" with the aid of polymorphic transformation of flagella. There are many measurements to characterize the behavior, such as run time, tumble time, and tumble angle. However, many measurements vary from each other due to different definitions or experimental setups. For example, Junot et al., 2022 used the unbundling time to characterize the tumble duration, and they defined that as the time when a *E. Coli* has at least 1 flagellum outside the bundle. They estimated the average unbundling time of $0.4s$ (Junot et al., 2022). Other works such as Korobkova et al., 2004 who measured CCW-CW series of motors of wild-type *E. Coli* found an average CW-rotating time of around $0.38s$. The fundamental work by Berg and Brown, 1972 was the first time to measure the quantities characterizing the tumbling event of wild-type *E. Coli*. He used the concept of twiddle instead of tumbling; a wild-type *E. Coli* twiddles when the disorienting speed is over 269.5 degree$/s$. They measured the twiddle angle of $62 - 68^\circ$ within a twiddle time of $0.2s$. Some years

later, Taute et al., 2015 measured similar quantities with better equipment and obtained a twiddle angle of 57 ± 37 and twiddle time of $0.19s$. The distribution of run and tumble time has also been under debate for years. The classic picture is that run and tumble are Poissonian, so an exponential distribution for both is expected (Berg and Brown, 1972; Berg, 2004; Saragosti et al., 2011; Alon et al., 1998), with a mean of around $1s$ for run time, around $0.1s$ for tumble time (Berg, 2004; Qu et al., 2018). However, recent studies (Korobkova et al., 2004; Korobkova et al., 2006; Emonet and Cluzel, 2008; Min et al., 2009; Wang et al., 2017) revealed that the results of the measurements for the CCW-rotating time for the motors deviate from exponential distribution and it can be estimated with a power law at long time scale. Figueroa-Morales et al., 2020 extended the idea and found that the run time is log-normal distributed.

The role of hook

Shown in FIGURE 1.3(a), the hook is the short part of a flagellum connecting the motor and the filaments. According to some literature (Vogel and Stark, 2012; Son, Guasto, and Stocker, 2013; Riley, Das, and Lauga, 2018), it has a vital role in the dynamics of bundling and unbundling (Vogel and Stark, 2012; Son, Guasto, and Stocker, 2013; Riley, Das, and Lauga, 2018). Its mechanical property is very crucial so that the hook can be sufficiently flexible for multi-flagellated swimmers to bundle during run (Brown et al., 2012; Lee et al., 2018b; Nguyen and Graham, 2018), while the hook must also be stiff enough to withstand the torque from the motor and help the filaments leaving the bundle during tumble. Many groups have measured different mechanical properties of the hook of *E. Coli*. Block, Blair, and Berg, 1991 show the torsional rigidity of hooks is $1 \times 10^7 Nm^{-2}$ and Sen, Nandy, and Ghosh, 2004 measured the bending stiffness with a value of $10^{-29} Nm^2$. Some other works propose a changing bending stiffness of hooks due to the different requirements on its mechanical properties during run and tumble. Son, Guasto, and Stocker, 2013 show the hook has a bending stiffness of $2.2 \times 10^{-25} Nm^{-2}$ when bacteria swim steadily while the bending stiffness drops to $3.6 \times 10^{-26} Nm^{-2}$ when they do not swim. Nord et al., 2022 present an increase in bending stiffness with torque. Furthermore, Zhang et al., 2023 report that the hook is stiffer when the motor attached rotates CW (tumble) than CCW (run) under a similar magnitude of the torque.

Flagellar synchronization and bundle formation

We have mentioned that the helical flagella of *E. Coli* naturally bundle together under CCW rotation during the run stage. Generally, the synchronization mechanism has been studied in various works (Kim and Powers, 2004; Reichert and Stark, 2005; Kim et al., 2003) since the presence of kinematic reversibility in Stokes equation (equation 2.27) may prevent the synchronization process provided that the swimmers have the right symmetries. Different swimmers have developed different strategies to overcome the limit of hydrodynamics at low Reynolds number, such as the flagellated swimmers (*E. Coli* as an example). The synchronization of the flagella is a result of hydrodynamically-induced attraction between rotating helices (with the correct combination of rotating direction and helicity of the helices). The attraction can be induced between CCW-rotating left-handed flagella and its mirror images. The attraction between flagella during bundling results from the standard flow field generated by individual rotating helices (Reigh, Winkler, and Gompper, 2012; Flores et al., 2005; Kim and Powers, 2004). The bundling process has been quantitatively

studied in a few works (Janssen and Graham, 2011; Reigh, Winkler, and Gompper, 2012). In the beginning, the helices are aligned and unbundled; the tangential hydrodynamic forces generated due to the rotating flow fields tilt the individual flagella so that they are in closer contact near the fixed end while the free ends are still separated (Macnab, 1977). Also, Reigh, Winkler, and Gompper, 2012 found that the flagella with phase mismatch can synchronize by hydrodynamic interaction within a few rotations. Some numerical works have also investigated the effect of the filaments' elasticity on the dynamics of bundling or unbundling (Flores et al., 2005; Watari and Larson, 2010; Janssen and Graham, 2011; Kanehl and Ishikawa, 2014; Ishimoto and Lauga, 2019; Reigh, Winkler, and Gompper, 2013; Reigh, Winkler, and Gompper, 2012). In which, Janssen and Graham, 2011 show that for the helices with different flexibility and initial conditions, helices can have varied bundling states, such as tight bundles with helices in mechanical contact or loose bundles with non-touching and interwind helices.

Swimming at solid surfaces

In bulk solution, *E. Coli* is known to swim in a fashion of random walk, so it swims generally in a straight line with rapid re-orientations in between, called tumble described previously. However, there are rarely such systems where bacteria can be isolated and swim freely; primarily, a surface is present (Lauga, 2016; Hartmann et al., 2019; Costerton et al., 1987). The presence of surfaces is vital for many bacteria's survival, such as the formation of biofilm (section 1) where spreading of bacteria on surfaces is fundamental. Furthermore, the use of microfluidic devices in modern experimental techniques allows the manipulation and observation of microorganisms (Kantsler et al., 2013; Denissenko et al., 2012), so it is important to study the effect of surfaces theoretically to interpret experimental results. Flagellated *E. Coli*-like microorganisms are reported to have a phenomenon called "wall entrapment" (Frymier et al., 1995; Bianchi, Saglimbeni, and Di Leonardo, 2017; Berke et al., 2008) where they are get trapped, swim in circles and parallel to the solid wall. The circular motion is a result of the hydrodynamics-induced torque force on the swimmer, and the torque is due to the increased drag of the confined liquid between the swimmer and the surface. Depending on the boundary condition, the circular motion would be clockwise on a non-slip wall (Lauga et al., 2006; Li et al., 2008; Lemelle et al., 2010; Lopez and Lauga, 2014) or counter clockwise on a slip wall.

It is still under debate whether the phenomenon arises from a statistical effect of steric interactions (Li and Tang, 2009; Li et al., 2011) or it has a pure hydrodynamic origin (Vigeant et al., 2002; Vigeant and Ford, 1997; Berke et al., 2008; Sipos et al., 2015). From the perspectives of the hydrodynamic origin, as described before in this section, *E. Coli* can be modeled as a pusher. Far-field hydrodynamics predicts that it could be attracted to surfaces while aligning its main axis with surfaces (section 2.3.1). However, in the near-surface hydrodynamics of microswimmers, the higher-order terms of multipole expansions become essential. Spheroidal squirmer has been used widely to model elongated microswimmers, as mentioned in section 2.3.3. The slip velocity is written as a sum of Legendre polynomials (similar to equation 2.65). Ishimoto and Gaffney, 2013 have performed fixed-point analysis of such squirmers, and they found that at a small aspect ratio, pullers have stable fixed points with the orientation pointing towards the wall, while pushers show unstable fixed points at medium-ranged values of B_2 and B_3 (the magnitude of the higher order terms in equation 2.65). When the aspect ratio increases, pushers develop stable fixed points with the orientation vector pointing away from the wall. However,

pullers present more unstable paths at a fixed distance from the wall. Ishimoto and Gaffney, 2013 also reported the effect of the boundary conditions of a wall (slip or non-slip) on the location and characteristics of fixed points, leading to different behavior of microswimmers near walls.

Furthermore, for the swimmers in close contact with the wall, the hydrodynamic torques due to the anisotropic bodies result in a finite angle between the swimming direction and the wall (Vigeant et al., 2002). Another interesting aspect appears when rotational diffusion is also involved (Elgeti and Gompper, 2009; Drescher et al., 2011). As a pusher swimmer aligns its orientation vector with the wall hydrodynamically, the rotational diffusion deviates the orientation from the parallel arrangement. Therefore, the distance to the wall is expected to fluctuate for a pusher with a low speed and significant orientation fluctuation.

Many literatures have reported that for any theoretical model of active random walk with a finite persistence length, wall accumulation of these active particles can be observed (Ezhilan, Alonso-Matilla, and Saintillan, 2015; Elgeti and Gompper, 2009; Tailleur and Cates, 2009; Yan and Brady, 2015; Maggi et al., 2015; Bechinger et al., 2016). However, without re-orientation, the active particles are just trapped by walls. Therefore, rotational diffusion is a crucial factor for active particles to escape from the wall. Li and Tang, 2009; Li et al., 2011; Elgeti and Gompper, 2009 propose that the steric repulsion and rotational Brownian motion adequately explain the wall accumulation of bacteria. Elgeti and Gompper, 2009 ran Brownian dynamics simulations of the encounter of Brownian rods with a wall without any hydrodynamic interactions. Therefore, the competition between the excluded-volume interaction with the wall and the noise of the rod orientation produces an interesting adsorption behavior, also reported in Li and Tang, 2009. The first drives the rod orientations parallel with the wall, and the latter effectively propels the rods away from the wall. Since the orientation of the rod is randomly distributed, but eventually, the rod hits the surface at some moment. Following this, the steric interaction aligns the orientation of the rod with the wall, and then the rod moves parallel to the wall. In the meantime, the orientation fluctuation makes the rod slowly wiggle along the path until the rod finally moves away from the wall. This process has also been experimentally observed in Li and Tang, 2009.

Some other works have also studied the trapping effect of a wall of different shapes, such as concave (Vladescu et al., 2014; Fily, Baskaran, and Hagan, 2014) or convex (Sipos et al., 2015). Furthermore, other surface-induced microswimmer phenomena have also been investigated, such as the trapping of active particles with cusps (Kaiser, Wensink, and Löwen, 2012), and collective aggregation and adhesion of self-propelled colloids at walls (Wensink and Löwen, 2008).

The escape mechanism of *E. Coli* from a non-slip wall is still not fully understood. Dunstan et al., 2012 proposed a two-sphere model to simulate the behavior of *E. Coli* near a non-slip solid wall. They found that the swimmer could escape from the surface even without a tumbling mechanism, provided that the initial distance to the wall and the initial orientation with respect to the wall are in the right regime. Guccione et al., 2017 theoretically studied how the effective diffusion coefficient is related to the tumble rate of an *E. Coli*-like microswimmer confined between two walls. The hydrodynamical interaction is described by Stokes equations with appropriate boundary conditions at the interface. They found that at low confinement, the microswimmers, which could leave the stable state of orbiting and escape from the wall, have an optimal tumble frequency to maximize the effective diffusion coefficient. Molaei et al., 2014 used digital holographic microscopy to observe

the trajectories of wild-type *E. Coli* near a solid wall, they claimed that surfaces hinder tumbling and orient the post-tumbling direction parallel to the surface, making tumbling an ineffective escape mechanism. Lastly, in the work of Junot *et al.*, by using two-color three-dimensional tracking on individual motile *E. Coli*, they demonstrated that tumbling is the dominant escape mechanism. Also, they adapted the "behavioral variability" (BV) model from Figueroa-Morales et al., 2020 (described in detail later) to simulate the behavior of *E. Coli*, and obtained consistent results (Junot et al., 2022).

Theoretical models

The spatial exploration of *E. Coli* has been studied in great detail where *E. Coli* models which can describe the full behavior of "run and tumble" have been raised in full attention due to their ability to study various motility patterns of *E. Coli* as described before. The first model is the "Behavioral Variability"(BV) model initially proposed in Tu and Grinstein, 2005. Following the assumptions made in Khan and Macnab, 1980, the bacterial motor has two states: clockwise (CW) and counter-clockwise (CCW), with each state corresponding to a different potential well. The transitions between two states are governed by a thermal fluctuation over an energy barrier, determined by the instantaneous concentration of phosphorylated protein CheY-P, represented by $[Y](t)$. Let's consider the mean value of the concentration $[Y_0]$, thus, the concentration fluctuation is $\delta Y(t) = [Y](t) - [Y_0](t)$. δY can be normalised with its standard deviation of Y, σ_Y to become $\delta X = \delta Y/\sigma_Y$. δX serves as an internal parameter, and its fluctuation is modeled as an Ornstein-Uhlenbeck process in the "BV" model with a memory time of T_Y and δY is therefore Gaussian distributed, resulting in a switching event rate of:

$$\tau_s = \tau_0 e^{-\Delta_n \sigma X}. \tag{2.71}$$

Here, τ_0 is a standard switching time at the mean concentration $[Y_0]$, and Δ_n gives the sensitivity of transition between run and tumble to the concentration of CheY-P. For example, for a higher concentration of CheY-P, Δ_n has a higher value, so the run times are shorter (Cluzel, Surette, and Leibler, 2000). For the switching from $CCW \rightarrow CW$, δX of bacteria in a sample is randomly distributed, and each δX corresponds to a switching time of τ_s. As assumed in BV model, δX is Gaussian distributed, so the Gaussian distribution of $\ln(\tau_s)$ has a mean of $\ln(\tau_0)$ and a standard deviation of $\sigma_{ln(\tau_p)} = \Delta_n$, where τ_p is the persistence time. The consequence is that the run time is log-normal distributed provided that Δ_n is large, such distribution of run time has been confirmed in Korobkova et al., 2004 as described in section 2.3.4. For the switching of $CW \rightarrow CCW$, Δ_n is small, leading to an exponential distribution, also confirmed in many works before, shown in section 2.3.4. BV model has successfully predicted the three-dimensional exploration behavior, the escaping behavior from surfaces of *E. Coli* (Junot et al., 2022; Figueroa-Morales et al., 2020).

Another *E. Coli* model worthy of mentioning is the hydrodynamic bead-spring model of flagellated swimmers proposed by Watari and Larson, 2010; Kong et al., 2015, shown in FIGURE 2.6. The hydrodynamic interactions, driving the flagellar bundling, swimming, and flagellar unbundling while tumbling, are imposed by considering each bead as Stokeslet, modeled by the Rotne-Prager tensor. Torque is applied to the connecting joint between the flagella and the body to model the action of the motor. Furthermore, the features of the model, such as the dimensions of the body and the flagella, the polymorphic transformation of CW-rotating flagellum, and the motor torque, are chosen to match with the experimental observations from

Turner, Ryu, and Berg, 2000; Darnton et al., 2007. Also, the polymorphic transformation of the unbundling flagellum is achieved by switching the equilibrium bending and torsional angle of the flagellum, resulting in a series of states, including the normal, semi-coiled, and curly-1, in turn defining the time points of the run-and-tumble process. The model shows the prediction of run speed, bundle, body and motor rotation frequency, and tumble angle in good agreement with the measurements done by Turner, Ryu, and Berg, 2000; Darnton et al., 2007 (Refer to section 1 for the details of these measurements.)

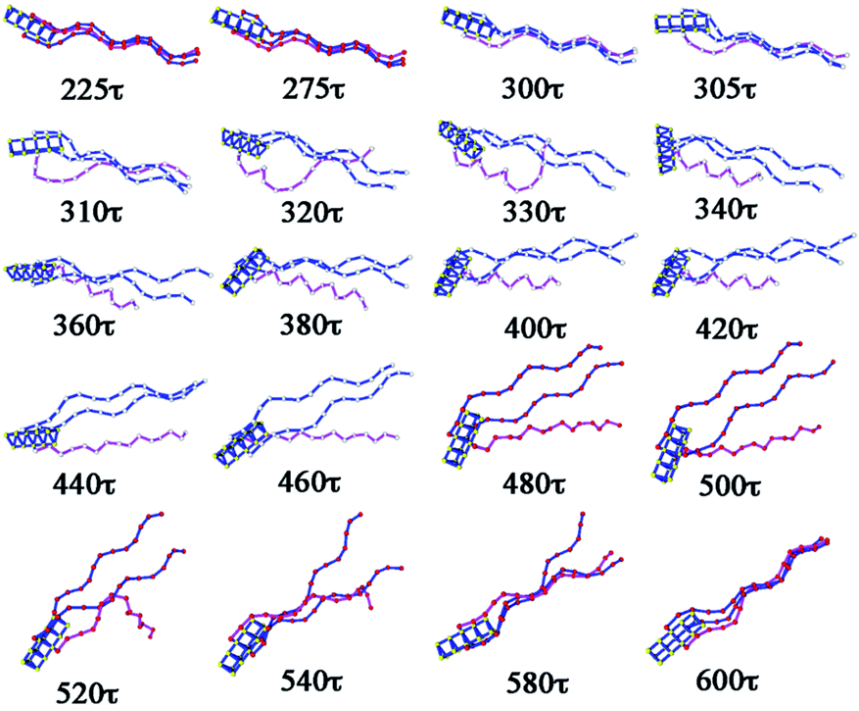

FIGURE 2.6: The run and tumble process of the hydrodynamic coarse-grained and beads-springs model of flagellated swimmers, proposed by Kong et al., 2015. τ is the unit of time used in the original time equivalent to 7.8×10^{-4}s. Polymorphic transformation is incorporated into the model. The CW rotation of the unbundling flagellum lasts for the period from 300τ to 500τ, in which the flagellum maintains in the semi-coiled state between 300τ and 400τ and becomes curly-1 from 400τ to 500τ. The figure is adapted with permissions from Kong et al., 2015, Soft Matter

2.3.5 Collective motion of swimmers

The various collective patterns of microswimmers' motility have already been discussed in section 1. Here, we will go into more detail about these collective phenomena and explain the theories behind them.

Swarming, clustering, and jamming

Swarming is a surface phenomenon as a precursor of biofilm. Swarming bacteria are often reported to adopt a different phenotype such that their aspect ratio is changed and they grow extra flagella (Kearns, 2010; Harshey, 2003; Kaiser, 2003; Kaiser, 2007; Tuson et al., 2013; Zhang et al., 2012). From the experimental observations,

the swarming motion is characterized by the coherent movement of densely packed clusters forming swirling patterns persisting for a few seconds (Ariel et al., 2013; Be'er et al., 2009; Be'er et al., 2013; Benisty et al., 2015; Chen et al., 2012; Darnton et al., 2010; Jeckel et al., 2019; Zhang et al., 2010; Zhang et al., 2009). Many literatures have reported varied physical aspects of swarming. Here, we want to emphasize the surface cell density and aspect ratio of cells. Be'er et al., 2020 proposed a phase diagram of swarming *Bacillus subtilis* mutants with different aspect ratios and different cell densities, shown in FIGURE 2.7(b). Be'er et al., 2020 also found that the collective speed of bacteria is monotonically promoted with density with a fixed aspect ratio, reflected in the phase diagram [FIGURE 2.7(b)]. It shows that there is a minimal surface density for cells to be mobile; cells are in the jamming phase because they cannot move efficiently at high density due to confinement (Wensink et al., 2012; Ariel et al., 2018). Also, the mean speed of cells is positively correlated with the aspect ratio in Be'er et al., 2020. Within intermediate surface density, we can characterize the phases for three situations: 1) The cells of a small aspect ratio move coherently in the swarm phase. 2) For long cells at relatively low density, they form small clusters (SC). 3) For long cells at relatively high density, large moving clusters (LCs) of size comparable to the system. Also, Be'er et al., 2020 reported different analysis methods to determine swarming, such as density distribution function and cluster size distribution, are shown in FIGURE 2.8. For short cells, the swarming phase is characterized by a power law decay with an exponential cutoff in cluster size distribution [FIGURE 2.8(a-b)] and a unimodal spatial distribution in surface density distribution (FIGURE 2.8e-f). For long cells at small density, a power law decay in cluster size distribution shows the presence of small clusters (SCs), and the mode of surface density distribution shifts towards smaller density [FIGURE 2.8(g-h)]. Lastly, for the long cells at higher density, the swarm is segregated into SCs and LCs, two peaks shown in surface density distribution [FIGURE 2.8(g-h)] and the presence of a peak at large cluster size with the size comparable to the system size is observed in cluster size distribution in FIGURE 2.8(c-d). The mean square displacement (MSD) of swarming bacteria was analyzed and shows that they perform super-diffusivity; however, the super-diffuse property diminishes at high density (Be'er et al., 2020).

Active turbulence

Similar to swarming, bacteria, tissue cells, filament/motor-protein mixtures show a collective behavior that consists of spatially and temporally random flow patterns and visually chaotic (FIGURE 1.14b), denoted as active turbulence nowadays (Wioland et al., 2013; Martinez et al., 2020; Guo et al., 2018b), however, active turbulence does not involve a phenotype change. The motion is similar to the traditional Kolmogorov-Kraichnan-type hydrodynamic turbulence (Kraichnan and Montgomery, 1980), except that it happens at very low Reynolds numbers. For microswimmers under confinement, active turbulence is often observed for a sufficiently large density of microswimmers according to the relation (Martinez et al., 2020):

$$\frac{\phi_c(H)}{\phi_c^\infty} \approx 1 + \frac{3}{10}(2\pi\frac{v\tau}{H}) + \frac{1}{5}(2\pi\frac{v\tau}{H})^2, \tag{2.72}$$

$\phi_c(H)$ is the confined critical volume fraction as the function of the height of confinement. v and τ are two set constants: bacterial swimming speed and average duration between two tumble events, respectively. ϕ_c^∞ is set to be $\phi_c^\infty = \phi_c(H = 400\mu m) \approx$

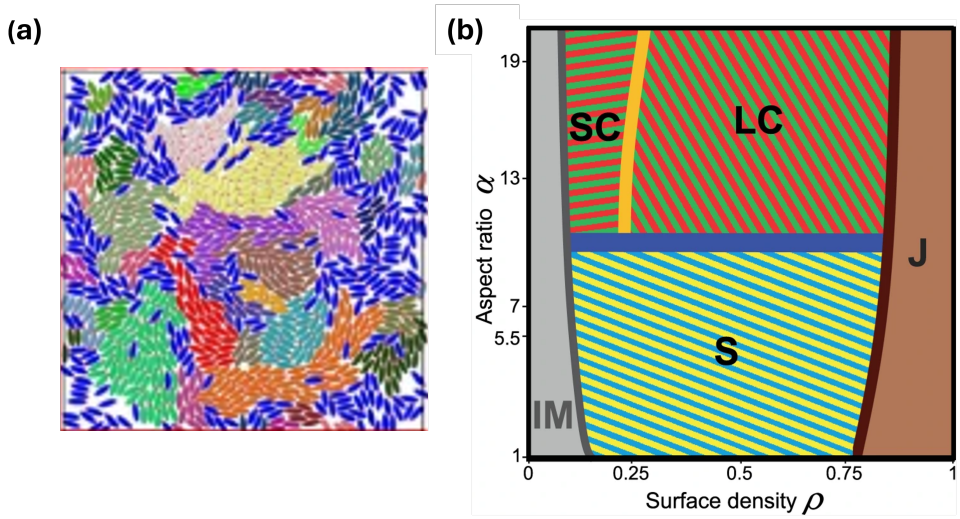

FIGURE 2.7: (a) Snapshot of monolayer swarming of spheroidal squirmers with the aspect ratio of 2. Colors label the cluster with different sizes. The clusters smaller and equal to 4 squirmers are labeled in blue; the clusters with sizes beyond 4 squirmers and various other random colors are used. (b) Phase diagram of aspect ratio and surface density, demonstrating 5 different phases: immotile (IM), swarming (S), small clusters (SCs), large clusters (LC), and jammed (J). In (a), the two swarming phases at the bottom show the difference between short and long cells. As shown in (b), the short cells move coherently. However, long cells are more likely to form the regions of small clusters (SCs) and large clusters (LCs). (a) is adapted from Qi et al., 2022, Communication Physics (Open Access). (b) is from Be'er et al., 2020, communication physics (Open Access).

0.75%, plotted in FIGURE 2.10. The equation is derived and explained from mean-field continuum kinetic theory (CKT). Active turbulence is due to hydrodynamic instability due to the negative viscosity increment (NVI) under confinement. The negative viscosity increment describes the situation that within a system of pusher suspensions at low shear, the alignment between swimmers enhances the applied shear stress on fluid, resulting in a decrease in viscosity with the volume fraction of swimmers. Note that pullers do not possess the NVI phenomenon. CKT can be used to estimate the relationship of viscosity with packing fractions in an infinite system. The stability analysis of the infinite system gives the dependence of instability eigenvalue on $k = 2\pi/H$, the perturbation wavelength (Hohenegger and Shelley, 2010; Saintillan, 2010).

Qi et al., 2022 laid out "minimal" criteria for whether a dense and visually chaotic system could be classified as active turbulence, including:

- At very low Reynolds numbers $Re \ll 1$(Wensink et al., 2012; Copeland and Weibel, 2009).
- Sufficiently high density of microswimmers with the average inter-swimmer distance smaller than the size of the swimmers (Be'er et al., 2020).
- Visually chaotic flow pattern with collective behavior at large scales (Alert, Joanny, and Casademunt, 2020; Bratanov, Jenko, and Frey, 2015; Doostmohammadi et al., 2017).

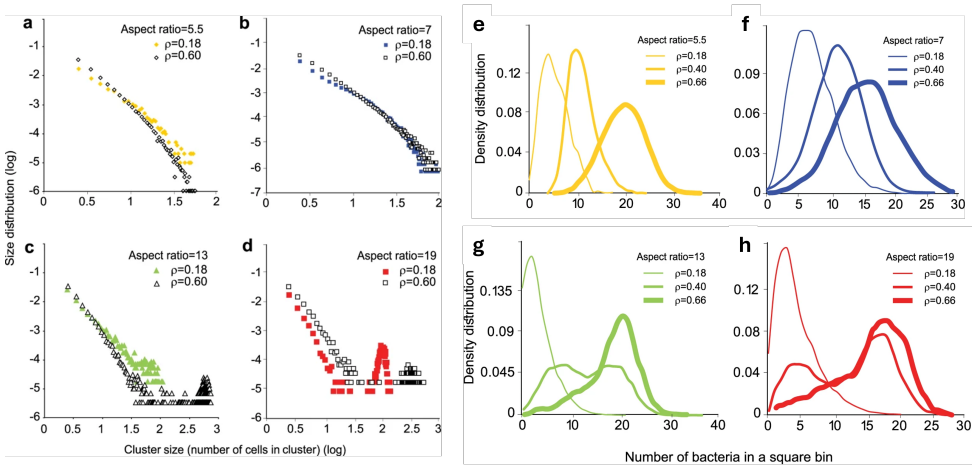

FIGURE 2.8: (a-d) Cluster size distribution of different aspect ratios and densities. (a-b) examples of short cells in the swarming phase, characterized by power law decay with an exponential cutoff. (c-d) Examples of long cells at low density show a power law decay, while at high density ($\rho = 0.6$), a peak exists, indicating the presence of a large cluster with a size comparable to the size of the system. (e-h) Surface density distribution of varied aspect ratios and densities with a 10×10 partition of the view area ($15 \times 15 \mu m$ bins). (e-f) Examples of small aspect ratios and swarming bacteria present an unimodal spatial distribution, and the mode increases with the mean surface density. (g-h) Examples of long cells, the swarm is segregated into SCs and LCs, with the peaks indicating different surface densities of different regions. The portion of SC and LC changes with the mean surface density. The figure is adapted from Be'er et al., 2020, communication physics (Open Access).

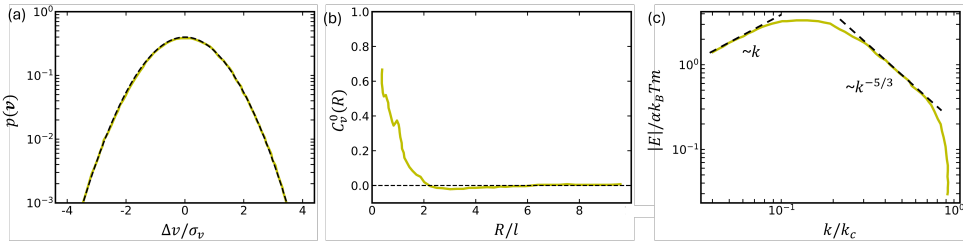

FIGURE 2.9: Analysis plots of a system of monolayer pusher squirmers undergoing active turbulence. (a) Velocity distribution of in-plane Cartesian components, normalized by the standard deviation δ_v. The black dashed curve is a fit of Gaussian of unit variance. (b) Normalized spatial velocity correlation function as shown in equation 2.3.5. The distance R is normalized by the length of the swimmer l. (c) Energy spectrum plot as a function of wave vector k and $k_c = \pi/(l/2)$. Power law fits are shown as dashed lines. Data of the plots are adapted from Qi et al., 2022, Community Physics (Open Access).

- A cluster size distribution of a power law decay with an exponential cut-off (Be'er et al., 2020), shown in FIGURE 2.8(a-b).
- The Cartesian velocity components of the microswimmers under active turbulence show a Gaussian distribution for the velocity distribution plot (Wensink et al., 2012; Dunkel et al., 2013), shown in FIGURE 2.9(a).

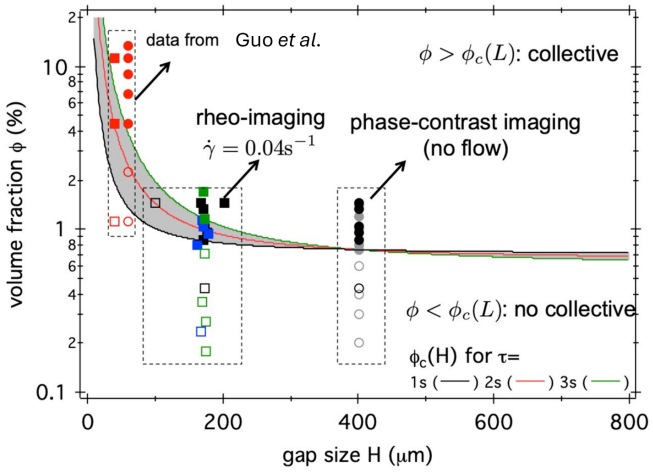

FIGURE 2.10: The relationship between the size of the confinement and the flow stability related to active turbulence. The red line shows the calculated confined critical volume fraction $\phi_c(H)$, shown in equation 2.3.5. $\phi_c(H)$ provides the boundary between the stable (below the boundary) and unstable (above) suspensions with different persistence time τ and with a speed of $15\mu ms^{-1}$. The experimental observations of flow with and without banding are shown as filled squares and open squares, respectively. The observations with or without a large correlation length scale are shown as filled circles or open circles, respectively; the data points based on rheo-imaging and phase-contrasting imaging without flow are demonstrated as squares and circles, respectively. The red data is from Guo et al., 2018a. The figure is adapted from Martinez et al., 2020, PNAS (Open Access).

- a velocity correlation function with a characteristic vortex size (It shows as the function becomes negative at an intermediate distance) (Wensink et al., 2012; Dunkel et al., 2013; Sokolov and Aranson, 2012). The normalised velocity correlation function is defined as (Wensink et al., 2012; Zhang et al., 2009; Dunkel et al., 2013; Chen et al., 2012):

$$C_v(\boldsymbol{R}) = \frac{< \sum_{i,j\neq i} \boldsymbol{v}_i(t) \cdot \boldsymbol{v}_j(t) \sigma(\boldsymbol{R} - |\boldsymbol{r}_i - \boldsymbol{r}_j|) >}{< \sum_{i,j\neq i} \sigma(\boldsymbol{R} - |\boldsymbol{r}_i - \boldsymbol{r}_j|) >}. \tag{2.73}$$

  And $C_v^0(R) = C_v(R)/c_0$, with $c_0 = \sum_i < \boldsymbol{v}_i^2 > /N$, and $R = |\boldsymbol{R}|$. N is the number of swimmers in the system and $\boldsymbol{v}_i$ is the velocity of each swimmer. The plot for a system undergoing active turbulence is shown in FIGURE 2.9(b).

- Energy spectrum with a peak at a k value indicating the characteristic vortex size. A power law decay $E(k)\ k^{-\kappa}, \kappa > 0$ for the length scale below the characteristic vortex size. The energy spectrum is written as:

$$E(k) = \frac{k}{2\pi} \int d^2 R e^{-i\boldsymbol{k}\cdot\boldsymbol{R}} C_v(\boldsymbol{R}). \tag{2.74}$$

  This expression is obtained from the Fourier transform of equation 2.3.5, the spatial velocity correlation function (Batchelor, 1953). Note that in FIGURE 2.9(c), the energy spectrum is plotted with a left-shifted $C_v(R)$ so that the decay begins at $R = 0$. For a system of bacterial suspensions, the scale of energy injection is the size of a microswimmer, yielding the maximum wavelength $k_c = \pi/(l/2)$.

Motility-Induced Phase Separation

MIPS is a phenomenon when self-propelled particles undergo phase separation where there are regions of high density ("liquid") and low density ("gas") (Thompson et al., 2011; Fily and Marchetti, 2012; Redner, Hagan, and Baskaran, 2013; Bialké, Löwen, and Speck, 2013; Levis and Berthier, 2014). Interestingly, self-propelled particles with pure repulsion could undergo MIPS; however, passive particles cannot without attraction interactions (Tailleur and Cates, 2008). Within MIPS, the speed of active particles decreases with the rise in the local density, destabilizing the uniform suspensions. Therefore, the suspension undergoes phase separation where there is a dilute gas phase and a dense liquid phase with lower motility due to higher density. It has been reported that the liquid region normally exists as an almost immobile cluster with a size comparable to the system (Wu-Zhang, Fedosov, and Gompper, 2024).

Theoretically, there are two critical ingredients for MIPS to happen for a system of active particles with the self-propulsion speed of $v(\boldsymbol{r})$ (Cates and Tailleur, 2015). The first ingredient is that the active particles move slowly, and they tend to accumulate, written as a master equation:

$$\dot{P}(\boldsymbol{r},\hat{\boldsymbol{e}}) = -\nabla[v(\boldsymbol{r})\hat{\boldsymbol{e}})P(\boldsymbol{r},\hat{\boldsymbol{e}})] + \Theta[P(\boldsymbol{r},\hat{\boldsymbol{e}})], \tag{2.75}$$

Here, $\hat{\boldsymbol{e}}$ represents the orientation unit vector of particles, and $\Theta[P(\boldsymbol{r},\hat{\boldsymbol{e}})]$ considers the orientation change of particles. For Brownian rotational motion, $\Theta[P] = D_r\nabla_{\hat{\boldsymbol{e}}}P$. For an isotropic system, the steady state solution for equation 2.3.5 is $P_{ss} \propto 1/v(\boldsymbol{r})$, and speed is dependent on the position. However, such dependence is absent for the systems at thermal equilibrium, as the speed of particles undergoing Brownian motion is purely dependent on the temperature.

Secondly, the dependence of v on local density ρ is crucial. In detail, the accumulation of particles due to slowing down of the speed, in turn, causes even more accumulation. This phenomenon commonly arises in some cases, such as by quorum sensing (Miller and Bassler, 2001) or by steric exclusion interactions. Let us consider a system of uniform density profile $\rho_0 \equiv c/v(\rho_0)$, where c is a constant. A perturbation of density in position $\boldsymbol{r}$ rewritten as $\delta\rho(\boldsymbol{r})$, leading to spatially varying speed as $\delta v(\boldsymbol{r}) = v[\rho_0 + \delta\rho(\boldsymbol{r})] - v[\rho_0] = v'(\rho_0)\delta\rho(\boldsymbol{r})$. Therefore, if $v(\rho)$ negatively correlates with ρ, leading to a negative value of $v'(\rho)$, so $\delta\rho(\boldsymbol{r})$ is in antiphase with $\delta v(\boldsymbol{r})$. The steady-state density would be:

$$\rho_0 + \delta\rho' = \frac{c}{v(\rho_0) + v'(\rho_0)\delta\rho} \approx \frac{c}{v(\rho_0)}(1 - \frac{v(\rho_0')}{v(\rho_0}\delta\rho) = \rho_0 - \rho_0\frac{v'(\rho_0)}{v(\rho_0)}\delta\rho. \tag{2.76}$$

The instability of the system comes from the perturbation of speed is larger than the initial density perturbation, written as $\delta\rho' > \delta\rho$, leading to

$$\frac{v'(\rho_0)}{v(\rho_0)} < -\frac{1}{\rho_0}. \tag{2.77}$$

This instability coincides with the condition for spinodal decomposition to happen, corresponding to the concavity of the effective free energy density function with the local density of the system (Cates and Tailleur, 2015). MIPS can be detected with a peak located at large cluster size in cluster size distribution shown in FIGURE 2.8(c-d)($\rho = 0.60$). In section 2.3.5, the phase diagram in FIGURE 2.3.5 shows that for the bacteria of large aspect ratio, they decompose into the regions of small clusters (SCs)

and large clusters (LCs), which is an example of MIPS phenomena.

2.4 Numerical Simulation Methods

As we have discussed in section 2.1.4, Navier-stokes equation is only analytically solvable under specific conditions with particular assumptions. Computational simulation allows us to have possible solutions for the systems which cannot be solved analytically with faster speed and greater precision. Because of this, computational simulations have been used as bench tests for theories; also as the tool to validate experimental results with a similar system setup. For the interest of soft active matter physics, we notice that the phenomena normally happens at a length-scale between microscopic and macroscopic, such length scale is namely mesoscopic. For mesoscopic hydrodynamic simulation methods, they have been used in varied occasions such as dynamic of microswimmers, the growth of tissue, polymer dynamics and the behaviour of vesicles and cells. Such simulation methods include lattice Boltzmann (LB) (Succi, 2001), multi-particle collision dynamics (MPC) (Malevanets and Kapral, 1999; Gompper et al., 2009), smoothed particle hydrodynamics (SPH) (Lucy, 1977; Monaghan, 1992), and dissipative particle dynamics (DPD) (Hoogerbrugge and Koelman, 1992; Español and Warren, 1995; Groot and Warren, 1997) and smoothed dissipative particle dynamics (SDPD) (Español and Revenga, 2003; Müller, Fedosov, and Gompper, 2014). LB methods model the microscopic dynamics of fluid particles, then the fluid's macroscopic behavior emerges from the collective dynamics of these particles. Compared to them, SPH is grid-free, it solves the Navier-Stokes equations of fluid motion by a Lagrangian approach, and the equations are expressed in terms of particle interactions. Due to its grid-free nature, it has advantages of simulating moving boundaries, complex geometry, and large deformations. The details of DPD and SDPD are shown in section 3.4.1 and section 3.5, respectively.

Chapter 3

Methods and Model

3.1 Vesicle-like membrane model

The membrane is represented by N_p particles connected by springs into a triangulated network. Shear elasticity of the squirmer membrane is supplied by the spring potential (Fedosov, Caswell, and Karniadakis, 2010):

$$U_{bond} = \frac{k_B T l_m}{4p} \frac{3x^2 - 2x^3}{1 - x} + \frac{k_p}{l}, \tag{3.1}$$

where $x = l/l_m \in (0, 1)$, l is the spring length, l_m is the maximum spring extension, p is the persistence length, k_p is the force coefficient, and $k_B T$ is the energy unit defined by the temperature T in the simulated system. The curvature elasticity that provides bending resistance is implemented through the discretization of the Helfrich bending energy (Helfrich, 1973) as

$$U_{bend} = \frac{\kappa}{2} \sum_i \sigma_i (H_i - H_0^i)^2, \tag{3.2}$$

where κ is the bending rigidity, σ_i is the area corresponding to vertex i in the membrane triangulation, H_i is the mean curvature at vertex i, and H_0^i is the spontaneous curvature at vertex i. The mean curvature is discretized as $H_i = \mathbf{n}_i \cdot \sum_{j(i)} \sigma_{ij} \mathbf{r}_{ij} / (\sigma_i r_{ij})$, where $\mathbf{n}_i$ is the unit normal at the vertex i, $\sigma_i = \sum_{j(i)} \sigma_{ij} r_{ij}/4$, $j(i)$ spans all vertices linked to vertex i, and $\sigma_{ij} = r_{ij}(\cot\theta_1 + \cot\theta_2)/2$ is the bond length in the dual lattice with θ_1 and θ_2 being the angles at the two vertices opposite to the edge ij in the dihedral. The spontaneous curvature H_0^i is set locally after the triangulation of the surface.

The area and volume conservation constraints are represented by the potential (Fedosov, Caswell, and Karniadakis, 2010):

$$U_{a+v} = \frac{k_a (A - A_0^{tot})^2}{2A_0^{tot}} + \sum_{m \in 1 \ldots N_t} \frac{k_d (A_m - A_0^m)^2}{2A_0^m} + \frac{k_v (V - V_0^{tot})^2}{2V_0^{tot}}, \tag{3.3}$$

where k_a, k_d, and k_v are the coefficients of global area, local area and volume conservation constraints, respectively. A and V are the instantaneous area and volume of the enclosed membrane, A_0^{tot} and V_0^{tot} are the targeted global area and volume which are defined by the spheroidal shape. A_m is the area of the m-th triangle (or face) within the triangulation, while A_m^0 is the targeted value. N_t is the number of triangles within the triangulated surface.

3.2 Spheroidal Squirmer model

A spheroidal squirmer model, whose surface is described by

$$\left(\frac{x}{b_x}\right)^2 + \left(\frac{y}{b_y}\right)^2 + \left(\frac{z}{b_z}\right)^2 = 1, \tag{3.4}$$

where b_z and $b_x = b_y$ are the major and minor radii of the spheroidal squirmer [see FIGURE 2.5(e)]. The orientational vector $\mathbf{e}$ of the squirmer is aligned with its major axis. The aspect ratio of the spheroidal shape is set to $b_z/b_x = 2$, which is similar to the aspect ratio of $2-3$ for the body of *E. coli* bacteria (Darnton et al., 2007). The squirmer surface is discretized by N_p particles connected by springs into a triangulated network. To maintain the spheroidal shape, the squirmer consists of a membrane-like surface with shear and curvature elasticity, and has constraints for its surface area and enclosed volume (Fedosov, Caswell, and Karniadakis, 2010; Fedosov, Noguchi, and Gompper, 2014). Details of the membrane model are described in section 3.1.

Locomotion of a spheroidal squirmer is imposed through the prescribed surface slip velocity which has already been mentioned in Section 2.3.3. However, the model we employed in the work has an extra term called rotlet dipole in the surface slip velocity, written as (Theers et al., 2018; Zöttl and Stark, 2018; Ishikawa, Simmonds, and Pedley, 2006; Pagonabarraga and Llopis, 2013):

$$\mathbf{u}_{sq} = -B_1(\mathbf{e}_\zeta \cdot \mathbf{e}_z)(1+\beta\zeta)\mathbf{e}_\zeta + \frac{3\lambda z_s \bar{r}_s}{r_s^5}\mathbf{e}_\varphi, \tag{3.5}$$

As mentioned before, $\mathbf{e}_z$, $\mathbf{e}_\zeta$, and $\mathbf{e}_\varphi$ are unit vectors in spheroidal (ζ, τ, φ) coordinates. The parameter B_1 determines self-propulsion speed of the squirmer, and the coefficient β defines different swimming modes of the squirmer, including a pusher ($\beta < 0$), a neutral swimmer ($\beta = 0$), and a puller ($\beta > 0$). The extra term in equation (3.5) defines a rotlet dipole with the strength λ, where $\mathbf{r}_s = (x_s, y_s, z_s)$, $r_s = |\mathbf{r}_s|$, $\bar{r}_s = \sqrt{x_s^2 + y_s^2}$ with the subscript s denoting points at the squirmer surface. The rotlet dipole mimics a counter-rotating flow field, e.g. of *E. coli* whose body and flagella bundle rotate in opposite directions (Hu et al., 2015a). To verify the correctness of squirmer-model implementation, the flow field generated by a squirmer has been compared with the corresponding analytical solution (Theers et al., 2016b), yielding a good agreement.

3.3 Bacterium Model

Our model of *E. Coli* has two parts: a rounded sphero-cylindrical cell body and N_{flag} left-handed helical flagella (see FIGURE 3.1). The cell body has its orientation vector aligned with x axis and b_x is the length of the half-major axis has the value of $b_x = 9$ in simulation units and the length of the semi-minor axis $by = b_z$, following the aspect ratio of $by/bx = 2-3$ for wild *E. Coli* (Darnton et al., 2007). The surface of the body is discretized by $N_v = 1278$ particles which are connected by non-linear elastic springs to form a membrane of a triangular network (section 3.1). As shown in FIGURE 3.1(b), the surface of the body has a shape that can be described by the formula:

$$\left(\frac{|x|}{b_x}\right)^{8.5} + \left(\frac{y}{b_y}\right)^2 + \left(\frac{z}{b_z}\right)^2 = 1 \tag{3.6}$$

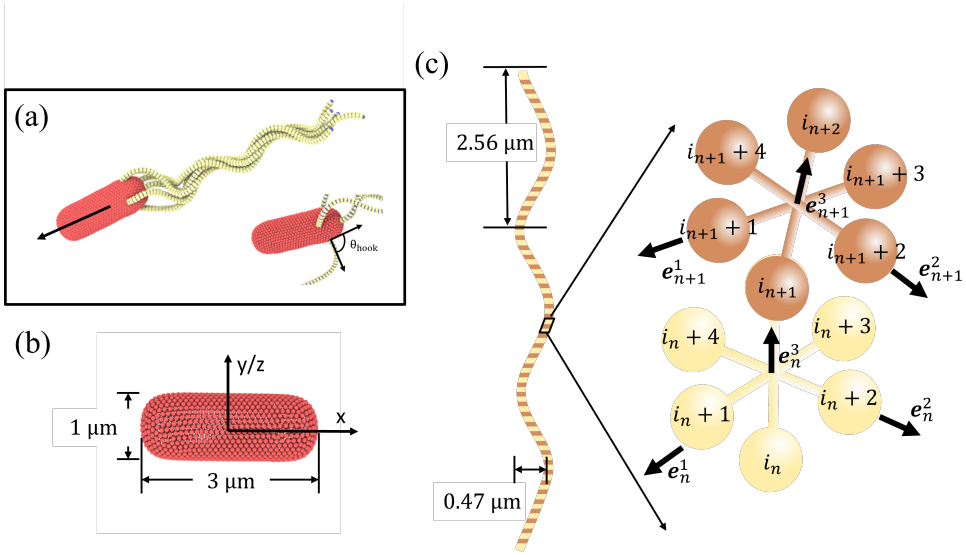

FIGURE 3.1: The model of *E. Coli*. (a) Overall model, composed of a prolate rounded sphero-cylindrical cell body (b) and 5 left-handed helical flagella (c). The black arrow labels the orientation vector of the body, aligning with the half-major axis of the body. The inset shows the angle (θ_{hook}) between the first a few sections of the flagellum and the body surface. The angle is initially set at 90◦. (b) Model of the spherocylindrical cell body with a length of $3\mu m$ and diameter of $1\mu m$. It is a triangular and tetrahedral membrane mesh consisting of 3178 particles and can be formed by the formula given in 3.6. (c) Model of the flagellum, a left-handed flagellum of three turns. It has a diameter of $0.47\mu m$ and a pitch length of $2.56\mu m$ and is made up of 76 segments. The model of flagellum is based on (Hu et al., 2015a).

The structure of flagellum is based on Hu et al., 2015a. The left-handed helical flagellum, as illustrated in FIGURE 3.1(c), was adapted from helical worm-like chain (Vogel and Stark, 2010; Yamakawa, 1997) to accommodate its combination with Dissipative Particle Dynamics (DPD). The flagellum comprises a total of $N_s = 76$ segments (3 helical turns) with a collective arrangement of 381 particles. Within each segment, six particles are organized in an octahedral structure, with an edge length represented by $a/\sqrt{2\pi}$. This arrangement forms 12 bonds along the edges and 3 bonds along the diagonals. The preferred bond lengths are $r_e = 0.06b_x/\sqrt{2\pi}$ for the edges and $r_e = 0.06b_x$ for the diagonals. The utilisation of an octahedral construction enables a direct depiction of the inherent twist present in the flagellum. Additionally, it facilitates the coupling of this twist with the forces exerted by the DPD fluid.

The contour of the flagellum is determined by the bonds $\mathbf{b}^3_n = \mathbf{r}_{i_n+1} - \mathbf{r}_{i_n}$, where n takes values from 1 to N. These bonds, along with $\mathbf{b}^1_n = \mathbf{r}_{i_n+1} - \mathbf{r}_{i_n+3}$ and $\mathbf{b}^2_n = \mathbf{r}_{i_n+2} - \mathbf{r}_{i_n+4}$, establish orthonormal triads $\{\mathbf{e}^1_n, \mathbf{e}^2_n, \mathbf{e}^3_n\}$ in which $\mathbf{e}^\alpha_n/|\mathbf{e}^\alpha_n|$ with $\alpha \in 1,2,3$. Also, here the $\mathbf{r}_{i_n}$ represents the positions of the backbone particles, while the $\mathbf{r}_{i_n+k}$ (with $k = 1,2,3,4$) represent the positions of particles lying in the plane perpendicular to the vector $\mathbf{e}^3_n$.

To capture the local elastic deformation of a flagellum, we transport the triad $\{\mathbf{e}^1_n, \mathbf{e}^2_n, \mathbf{e}^3_n\}$ to $\{\mathbf{e}^1_{n+1}, \mathbf{e}^2_{n+1}, \mathbf{e}^3_{n+1}\}$ along the chain. This process involves two steps: (i) First, we rotate $\{\mathbf{e}^1_n, \mathbf{e}^2_n, \mathbf{e}^3_n\}$ around $\mathbf{e}^3_n$ by a twist angle ϕ_n; followed by (ii) we rotate the twisted triad by a bending angle θ_n around the normal $\mathbf{n}_n = (\mathbf{e}^3_n \times \mathbf{e}^3_{n+1})/|\mathbf{e}^3_n \times$

$\mathbf{e}^3_{n+1}|$ to the plane defined by the contour bonds $\mathbf{b}^3_n$ and $\mathbf{b}^3_{n+1}$. Following these transformations, the elastic deformation energy can be determined, which has a formulae of:

$$U_{el} = \frac{1}{2}\sum_{\alpha=1}^{3} K^{\alpha}_{el} \sum_{n=1}^{N-1} (\Omega^{\alpha}_n - \Omega^{\alpha}_e)^2, \tag{3.7}$$

$K^1_{el} = k^2_{el}$ are bending strength and K^3_{el} is the twisting strength. $\mathbf{\Omega}_n = \Omega^1_n \mathbf{e}^1_n + \Omega^2_n \mathbf{e}^2_n + \Omega^3_n \mathbf{e}^3_n = \theta_n \mathbf{n}_n + \phi_n \mathbf{e}^3_n$ is the strain vector. The equilibrium geometry of the flagellum model is defined by Ω^{α}_n in equation 3.7 which can be used to impose a selected radius of the helix and its pitch length. This construction of the flagellum also allows the change of handness of the flagellum which is crucial in the tumbling process. This can be done by gradually switching the sign of Ω^1_e and Ω^2_e.

Each flagellum is attached to the body by making the first particle of the flagellum backbone to be part of the body discretization (see FIGURE 3.1). Also, to implement the rotation of flagellum, the motor torque $\mathbf{T}_m$ is decomposed into a force couple of $\mathbf{F}$ and $-\mathbf{F}$, exerting on particle $i_1 + 2$ and $i_1 + 4$, respectively ($\mathbf{T} = \mathbf{b}^2_1 \times \mathbf{F}$ with $\mathbf{F}$ anti-parallel to $\mathbf{b}^1_1$). Similarly, $\mathbf{F}$ and $-\mathbf{F}$ can also act on $i_1 + 1$ and $i_1 + 3$ ($\mathbf{T}_m = \mathbf{b}^1_1 \times \mathbf{F}$ with $\mathbf{F}$ parallel to $\mathbf{b}^1_1$). Therefore, the force is balanced to 0 on flagella. Also, swimming bacteria is normally torque-free as its cell body counter-rotates compared to its bundle rotation direction (Hu et al., 2015a). To achieve this, a torque of $-\mathbf{T}$ is applied to the head for every attached flagellum. We used the concept of angle potential to represent the hook. Angle potential defines the variation of angle between the first a few contour particles of flagellum with the area of the head surface around the flagellum attaching particle (θ_{hook}) [see FIGURE 3.1(a)]:

$$U_{hook} = K_{hook} \sum_{j(i)} \theta_{hook} - \pi/2)^2, \tag{3.8}$$

where K_{hook} is the potential strength, i is the anchoring particle at the body such that $\mathbf{r}_i = \mathbf{r}_{i_1}$, $j(i)$ spans all body vertices linked to vertex i, and θ^{hook}_j is the angle between vectors $\mathbf{r}_j - \mathbf{r}_i$ and $\mathbf{r}_{i_2} - \mathbf{r}_i$ [inset of FIGURE 3.1(a)]. Note that the preferred angle of anchoring orientation is $\pi/2$, imposing a perpendicular orientation of the flagellum to the body. The potential U_{hook} mimics the rigidity of a flagellum hook, which is an initial short part ($50 - 60$ nm in length) of the flagellum that is generally softer than the rest of the flagellum (Son, Guasto, and Stocker, 2013; Spöring et al., 2018). Thus, K_{hook} represents the bending stiffness of the physical hook of each flagellum of *E. coli*, and will be referred to as a hook rigidity further in text. Finally, excluded-volume interactions between different flagella, and between flagella and the body surface are implemented using the repulsive part of the Lennard-Jones (LJ) potential as

$$U_{LJ} = 4\epsilon_{LJ}\left[\left(\frac{\sigma_{LJ}}{r}\right)^{12} - \left(\frac{\sigma_{LJ}}{r}\right)^{6}\right] \tag{3.9}$$

This is for $r \leq 2^(1/6)\sigma$ and 0 for r otherwise. ϵ_{LJ} sets the strength of the potential, σ_{LJ} is the characteristic repulsion length and r defines the distance between two interacting particles of the repulsion. For both flagellum-flagellum and flagellum-body repulsion.

3.4 Dissipative Particle Dynamics (DPD)

3.4.1 Algorithm

DPD is often used to model fluids. It is a coarse-graining method that employs soft repulsive-only potentials on clusters of molecules called DPD particles. These DPD particles interact and move together in a Lagrangian manner (Koelman and Hoogerbrugge, 1993; Hoogerbrugge and Koelman, 1992). It has been applied to the simulations of colloids, polymer suspensions, liquids with interfaces, and other situtations.

Specifically, there are three types of pair-wise forces acting on each DPD particle (Groot and Warren, 1997):

- Purely repulsive conservative force $\mathbf{F}^C$.
- Dissipative force $\mathbf{F}^D$ acts to reduce the velocity difference between the particles in a pair.
- Random force $\mathbf{F}^R$ with the direction along the line connecting the centers of two particles in a pair.

Mathematically, for a system comprising N unit-mass particles, each particle has a position $\mathbf{r}_i$ and a velocity $\mathbf{v}_i$. Therefore, the force exerted on particle i by particle j $\mathbf{F}_{ij}$ is written as:

$$\mathbf{F}_{ij} = (F^C(r_{ij}) + F^D(r_{ij}) + F^R(r_{ij}))\hat{\mathbf{r}}_{ij} \tag{3.10}$$

Here, $\mathbf{r}_{ij} = \mathbf{r}_i - \mathbf{r}_j$, $r_{ij} = |r_{ij}|$ and $\hat{\mathbf{r}}_{ij} = \mathbf{r}_{ij}/r_{ij}$. Each force in particular can be written as:

$$F^C(r_{ij}) = \begin{cases} a(1 - r_{ij}/r_c) & r_{ij} < r_c \\ 0 & r_{ij} \geq r_c \end{cases} \tag{3.11}$$

$$F^D(r_{ij}) = -\gamma w^D(r_{ij})(\hat{\mathbf{r}}_{ij} \cdot \mathbf{v}_{ij}) \tag{3.12}$$

$$F^R(r_{ij}) = \sigma w^R(r_{ij})\xi_{ij} \tag{3.13}$$

Where a is conservative force coefficient (Pivkin, Caswell, and Karniadakis, 2011), r_c is the radius of the sphere of interactions. Also, ξ_{ij} is symmetric Gaussian random variable with zero mean and unit variance (Fan et al., 2006). They are independent regardless of different pairs and times. Also, $\xi_{ij} = \xi ji$ must be fulfilled to satisfy the conservation of momentum. ξ_{ij} together with $W^R(r_{ij})$ and $W^D(r_{ij})$ are related by fluctuation-dissipation theorem (Español and Warren, 1995), also $W^D(r_{ij}) = [W^R(r_{ij})]^2$, with $W^D(r_{ij})$ having formulae of

$$w^R(r_{ij}) = \begin{cases} (1 - r_{ij}/r_c)^s & r_{ij} < r_c \\ 0 & r_{ij} \geq r_c \end{cases} \tag{3.14}$$

Finally, σ is also subject to fluctuation-dissipation theorem (equation 2.43). It is written as:

$$\sigma^2 = 2\gamma k_B T \tag{3.15}$$

Where T is the system temperature and k_B is the Boltzmann constant (Español and Warren, 1995). s is the exponent of the random force. Finally, the dissipative force employs together with random force, sets the thermostat of the system, which maintains the temperature of the system to a desired value (Pivkin, Caswell, and Karniadakis, 2011).

The time evolution of each DPD particle follows the Newton's second law

$$\frac{d\mathbf{r}_i}{dt} = \mathbf{v}_i, \qquad m_i \frac{d\mathbf{v}_i}{dt} = \sum_{j \neq i} \left(\mathbf{F}^C(r_{ij}) + \mathbf{F}^D(r_{ij}) + \mathbf{F}^R(r_{ij}) \right), \tag{3.16}$$

where m_i is the mass of particle i. Time integration is performed using the velocity-Verlet algorithm.

3.4.2 Boundary conditions with walls

In the cases where solid walls present in a simulation box, solid walls are modelled by frozen DPD particles within a layer of thickness r_c (the cutoff radius for DPD interactions). with the same number density as that for the DPD fluid. To prevent wall penetration by fluid particles, a reflective surface is placed at the fluid-solid interface, where bounce-back reflection of fluid particles is enforced. No-slip BCs at the walls are imposed by the dissipative interaction between fluid and frozen-wall particles, and through the bounce-back reflection at the interface.

To restrict the motion of squirmers or *E. Coli* between the two walls, the particles forming the simulated objects are subject to the repulsive Lennard-Jones (LJ) potential

$$U_{LJ}(r) = 4\epsilon_{LJ} \left[\left(\frac{\sigma_{LJ}}{r} \right)^{12} - \left(\frac{\sigma_{LJ}}{r} \right)^{6} \right] \tag{3.17}$$

at the fluid-solid interface. Here, ϵ_{LJ} is the potential strength, σ_{LJ} sets a characteristic repulsion length, and r is the distance to the wall. Note that only the repulsive part of the LJ potential is considered by setting the cutoff distance to $2^{1/6}\sigma_{LJ}$.

3.5 Smoothed Dissipative Particle Dynamics (SDPD)

SDPD combines the advantages of two simulation techniques: DPD and SPH. Compared to DPD, which considers three forces for particle intetractions to mimic fluid properties and behavior, SDPD directly solves the complete Navier-stokes equation (equation 2.22) by discretizing the field variables such as pressure and density of the fluid, as in SPH method. The similarity between DPD and SDPD is that both methods include thermal fluctuations. However, SDPD is often considered as an improved DPD technique because it allows us to input the transport properties directly and produces an appropriate scaling of thermal fluctuation with the size of fluid particles(Español and Revenga, 2003). Despite all the advantages, one of the drawbacks of SDPD is that SDPD is more expensive computationally than DPD simulation method. SDPD has been applied in various cases: polymers in suspensions (Litvinov et al., 2008), margination of leukocytes (Fedosov, Peltomäki, and Gompper, 2014) and red blood cells in the tube flow (Fedosov et al., 2014). Mueller *et al.* proposed a new SDPD variation but taking account the conservation of angular momentum (Müller, Fedosov, and Gompper, 2014) which was not considered in the original SDPD algorithm(Español and Revenga, 2003). In the DPD algorithm (section 3.4.1), the direction of all forces aligns with the line connecting the center of two pair particles, naturally conserving local and global momentum. However, for SDPD, as we will discuss in more detail in the following text, two of the forces between a particle pair, the dissipative force ($\boldsymbol{F}^D$) and the random force ($\boldsymbol{F}^R$), no longer align the axis connecting the center of two particles. Therefore, the local and

global angular momentum is not conserved. The lack of angular momentum conservation may result in an asymmetric stress tensor, leading to wrong simulation results. Also, it has been found that it is crucial to consider the conservation of angular momentum in some cases, such as a Taylor-Couette flow with two types of non-mixing fluids(Götze, Noguchi, and Gompper, 2007). In the following text, we will derive the new approach of SDPD with the conservation of angular momentum. The derivation below is from Müller, Fedosov, and Gompper, 2014.

Firstly, for a field $g(\boldsymbol{r})$ with $\boldsymbol{r}$ being the position vector in a field, we can obtain its convolution integral with a kernel function $W(\boldsymbol{r}, h)$ to have the field variable $\tilde{g}(\boldsymbol{r})$:

$$\tilde{g}(\boldsymbol{r}) = \int_V g(\boldsymbol{r}')W(\boldsymbol{r} - \boldsymbol{r}', h)dV', \tag{3.18}$$

Where h is the smooth length. The kernel function $W(\boldsymbol{r} - \boldsymbol{r}', h)$ has to satisfy a few conditions: 1) it must be differentiable; 2) $\int_V W(\boldsymbol{r} - \boldsymbol{r}', h)dV'$ has to be normalized; 3) $lim_{h\to 0}W(\boldsymbol{r} - \boldsymbol{r}', h) = \delta(\boldsymbol{r} - \boldsymbol{r}')$. The integral can be discretized as

$$\tilde{g}(\boldsymbol{r}) \approx \sum_{j=1}^{N} \frac{m_j}{\rho(\boldsymbol{r}_j)} g(\boldsymbol{r}_j)W|\boldsymbol{r} - \boldsymbol{r}'|, h), \tag{3.19}$$

Here, we consider the integral is discretized into a small volumes of fluid j with a mass of m_j and at the position of $\boldsymbol{r}_j$. There are N such points in total within the volume V, and h is the smoothing radius. In the following text, the notation of $\rho(\boldsymbol{r}_j) = \rho_j$, $g(\boldsymbol{r}_j) = g_j$, and $W(|\boldsymbol{r} - \boldsymbol{r}'|, h) = W_{ij}$. Also, we define the particle density ρ_i as:

$$\rho_i = \sum_j m_j W_{ij}. \tag{3.20}$$

Therefore, the particle density can be calculated as the sum of the neighboring fluid particles within a cutoff radius of h. For the pressure field, a similar approach can be followed and discretized as SPH formalism. As an example, in the work by Müller, Fedosov, and Gompper, 2014, they performed SDPD simulations with a kernel function of the Lucy function:

$$W(r) = \frac{105}{16\pi h^3}(1 + 3\frac{r}{h})(1 - \frac{r}{h})^3, \tag{3.21}$$

This leads to $F(r) = 315/4\pi h^5(1 - r/h)^2$. Also, the equation of state is chosen as

$$p = p_0(\frac{\rho}{\rho_0})^\alpha + b. \tag{3.22}$$

The parameters of a, b, and p_0 can be freely chosen, and ρ_0 sets the reference density, defining with p_0 following the equation $c^2 = p_0\alpha/\rho_0$ where c is the speed of the sound in the medium.

Navier-stokes equation with a spin term can be written as (Condiff and Dahler, 1964):

$$\rho\frac{d\boldsymbol{u}}{dt} = -\nabla p + (\eta + \eta_r)\nabla^2\boldsymbol{u} + (\frac{\eta}{3} + \zeta - \eta_r)\nabla\nabla\cdot\boldsymbol{u} + 2\eta_r\nabla\times\omega, \tag{3.23}$$

Similar to the definitions in equation 2.22 except that we have a spin term (the last term on the right), we define a rotational viscosity η_r. In the spin term, ω is the spin angular velocity. This term properly balances translational and rotational friction

interactions (Müller, Fedosov, and Gompper, 2014).

With the Newton's second law $m_i d\boldsymbol{v}_i/dt = \boldsymbol{F}_i$, by discretizing the Navier-stokes equation (equation 3.5), we can define the forces similarly as defined in DPD:

$$\boldsymbol{F}_{ij}^{C} = (\frac{p_i}{\rho_i^2} + \frac{p_j}{\rho_j^2}) F_{ij} \boldsymbol{r}_{ij}, \tag{3.24}$$

$$\boldsymbol{F}_{ij}^{D} = -(\frac{5\eta}{3} + 3\eta_r - \zeta)\frac{F_{ij}}{\rho_i\rho_j}\boldsymbol{v}_{ij} - 5(\frac{\eta}{3} - \eta_r + \zeta)\frac{F_{ij}}{\rho_i\rho_j}\hat{\boldsymbol{e}}_{ij}(\hat{\boldsymbol{e}}_{ij}\cdot\boldsymbol{v}_{ij}), \tag{3.25}$$

$$\boldsymbol{F}_{ij}^{ROT} = -2\eta_r\frac{F_{ij}}{\rho_i\rho_j}\boldsymbol{r}_{ij}\times(\boldsymbol{\omega_i} + \boldsymbol{\omega_j}), \tag{3.26}$$

Where p_i is the particle pressure, $F_{ij} = |\boldsymbol{F_{ij}}|$ and $\hat{\boldsymbol{e}}_{ij} = \boldsymbol{r}_{ij}/|\boldsymbol{r}_{ij}|$. Similarly to the conservative force and dissipative force in the DPD algorithm, here, the conservative force ($\boldsymbol{F}_{ij}^{C}$) controls the local pressure field so it maintains the liquid local structure; the dissipative force ($\boldsymbol{F}_{ij}^{D}$) provides translational friction and reduces the velocity difference of particle pairs. The new force, rotational force ($\boldsymbol{F}_{ij}^{ROT}$), acts as a dissipative force on the rotational velocity of particle pairs. The random force can be calculated by balancing the translational and rotational dissipative forces to satisfy the fluctuation-dissipation theorem. Then we get:

$$\boldsymbol{F}_{ij}^{R} = (\sigma_{ij}^{a} d\bar{w}_{ij}^{S} + \sigma_{ij}^{b}\frac{1}{3}tr[dw_{ij}]\mathbb{1})\cdot\frac{\hat{\boldsymbol{e}}_{ij}}{dt}, \tag{3.27}$$

$$\gamma_{ij}^{a} = (\frac{20\eta}{3} - e\zeta)\frac{F_{ij}}{\rho_i\rho_j}, \tag{3.28}$$

$$\gamma_{ij}^{b} = (17\zeta - \frac{40\eta}{3})\frac{F_{ij}}{\rho_i\rho_j}. \tag{3.29}$$

Also, dw is a matrix of independent Wiener increments (Español, 1998) and $\sigma_{ij}^{a,b} = 2\sqrt{k_B T\gamma_{i,j}^{a,b}}$. One note is that the friction coefficients $(\gamma_{ij}^{a} + 2\gamma_{ij}^{b})/3)$ and γ_{ij}^{a} have to be positive, it restricts the range where these equations can be applied to $2\eta/3 \geq \zeta \geq 5\eta/3$. With the dissipative coefficients, we can simplify the writing of the three forces above:

$$\boldsymbol{F}_{ij}^{C} = (\frac{p_i}{\rho_i^2} + \frac{p_j}{\rho_j^2}) F_{ij} \boldsymbol{r}_{ij}, \tag{3.30}$$

$$\boldsymbol{F}_{ij}^{D} = -\gamma_{ij}^{a}(\boldsymbol{v}_{ij} + \frac{\hat{\boldsymbol{e}}_{ij}(\hat{\boldsymbol{e}}_{ij}\cdot\boldsymbol{v}_{ij})}{3}) - \frac{2\gamma_{ij}^{b}}{3}\hat{\boldsymbol{e}}_{ij})(\hat{\boldsymbol{e}}_{ij}\cdot\boldsymbol{v}_{ij}), \tag{3.31}$$

$$\boldsymbol{F}_{ij}^{ROT} = -\gamma_{ij}^{a}\frac{\boldsymbol{r}_{ij}}{2}\times(\omega_i + \omega_j). \tag{3.32}$$

One of the simplifications given in Müller, Fedosov, and Gompper, 2014 is that $\gamma_{ij}^{a} = \gamma_{ij}^{b} = \gamma_{ij}$ and $\sigma_{ij}^{a} = \sigma_{ij}^{b} = \sigma_{ij}$, then we have:

$$\gamma_{ij} = \frac{20\eta}{7}\frac{F_{ij}}{\rho_i\rho_j}, \tag{3.33}$$

$$\sigma_{ij} = 2\sqrt{k_B T\gamma_{ij}}. \tag{3.34}$$

where $\zeta = 20\eta/21$. The position and velocity are updated with velocity-verlet algorithm (Allen and Tildesley, 1991). Also, for the angular velocity, we have

$$\dot{\omega}_i = \sum_j \frac{1}{I_j} \boldsymbol{T}_{ij}. \tag{3.35}$$

Here, $\boldsymbol{T}_{ij}$ is the torque acting on particle i by particle j with a moment inertia of I_j and $\boldsymbol{T}_{ij} = 1/2\boldsymbol{r}_{ij} \times \boldsymbol{F}_{ij}$.

Chapter 4

Collective behavior of squirmers in thin films

Bacteria in biofilms form complex structures and can collectively migrate within mobile aggregates, which is referred to as swarming. This behavior is influenced by a combination of various factors, including morphological characteristics and propulsive forces of swimmers, their volume fraction within a confined environment, and hydrodynamic and steric interactions between them. In our study, we employ the squirmer model for microswimmers and the dissipative particle dynamics method for fluid modeling to investigate the collective motion of swimmers in thin films. The film thickness permits a free orientation of non-spherical squirmers, but constraints them to form a two-layered structure at maximum. Structural and dynamic properties of squirmer suspensions confined within the slit are analyzed for different volume fractions of swimmers, motility types (e.g., pusher, neutral squirmer, puller), and the presence of a rotlet dipolar flow field, which mimics the counter-rotating flow generated by flagellated bacteria. Different states are characterized, including a gas-like phase, swarming, and motility-induced phase separation, as a function of increasing volume fraction. Our study highlights the importance of an anisotropic swimmer shape, hydrodynamic interactions between squirmers, and their interaction with the walls for the emergence of different collective behaviors. Interestingly, the formation of collective structures may not be symmetric with respect to the two walls. Furthermore, the presence of a rotlet dipole significantly mitigates differences in the collective behavior between various swimmer types. These results contribute to a better understanding of the formation of bacterial biofilms and the emergence of collective states in confined active matter.

The Chapter is organised as follows. Section 4.1 contains all necessary details about the employed methods and models, including parameters used in simulations. In Section 4.2.1, structural properties of squirmer suspensions are analysed, including cluster size distribution, position and orientation of squirmers within the slit, and the radial distribution function. Dynamic properties are characterized in Section 4.2.2, where effective rotational diffusion, mean-squared displacement, and the average speed of squirmers are presented. The main results are discussed in Section 4.3, with short conclusions.

4.1 Methods and models

We consider a spheroidal squirmer model, the detail is shown in section 3.2.

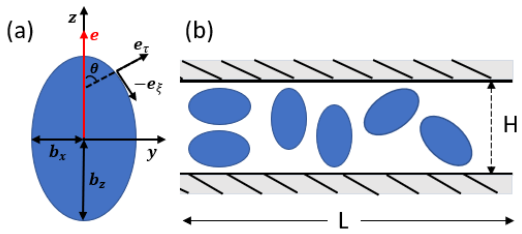

FIGURE 4.1: Schematic of the simulation setup. (a) Sketch of a spheroidal squirmer model. The orientation vector **e** is aligned with the squirmer's major axis z, and b_x and $b_z = 2b_x$ denote minor and major radii of the spheroidal shape. $\mathbf{e}_\tau$ and $\mathbf{e}_\zeta$ represent the local normal and tangential unit vectors, respectively. (b) Several squirmers within a slit of thickness H. Note that $H > 2b_z$, so that the squirmers can freely rotate within the slit and form a two-layered structure. L is the size of the simulation domain in the periodic dimensions perpendicular to the slit height.

4.1.1 Boundary conditions

The suspension of squirmers is confined between two walls in the h direction, while periodic BCs are applied along the other two perpendicular-to-h directions. Fluid flow is modeled by the dissipative particle dynamics (DPD) method (Hoogerbrugge and Koelman, 1992; Español and Warren, 1995), which is a particle-based hydrodynamics simulation technique (see section 3.4.1 for details). The presence of the wall is modelled as DPD frozen particles, and their interaction with other particles, such as fluid or squirmer particles is laid out in section 3.4.2.

Squirmers are submerged within a DPD fluid, and also filled by DPD fluid particles due to their membrane-like representation. The membrane surfaces of all suspended squirmers serve as a boundary separating DPD particles inside and outside of the membranes. This is achieved through the reflection of fluid particles at the membrane surfaces from inside and outside. Note that the dissipative and random forces between the internal and external fluid particles are deactivated, and only the conservative force is employed to maintain uniform fluid pressure across the membranes. To enforce the slip velocity $\mathbf{u}_{sq}$ at the squirmer surface, the dissipative interaction (see section 3.4.1) between the squirmer particles and those of the surrounding fluid is altered as follows

$$\mathbf{F}^D(r_{ij}) = -\gamma W^D(r_{ij})(\hat{\mathbf{r}}_{ij} \cdot \mathbf{v}^*_{ij})\hat{\mathbf{r}}_{ij}, \qquad \mathbf{v}^*_{ij} = \mathbf{v}_i - \mathbf{v}_j + \mathbf{u}^i_{sq}, \tag{4.1}$$

where $\hat{\mathbf{r}}_{ij} = (\mathbf{r}_i - \mathbf{r}_j)/r_{ij}$, $r_{ij} = |\mathbf{r}_i - \mathbf{r}_j|$, $\mathbf{u}^i_{sq}$ is the slip velocity at the position of squirmer particle i, while j corresponds to an outer-fluid DPD particle. Furthermore, the friction coefficient γ between fluid and squirmer particles is properly adjusted (Fedosov, Caswell, and Karniadakis, 2010) to ensure the imposition of $\mathbf{u}_{sq}$ at the squirmer surface.

4.1.2 Simulation setup and parameters

The simulation setup corresponds to a domain of dimensions $L \times H \times L$, where $L = 28b_z$ and $H = 2.5b_z$ ($b_z = 4$ in simulations), see FIGURE 4.1(b). The number density of fluid particles is $n_f = 320/b_z^3$, with a particle mass $m = 1$. The energy unit is $k_BT = 1$. DPD parameters for the interactions between fluid particles and between fluid and wall particles are $a = 200k_BT/b_z$, $\gamma = 80\sqrt{mk_BT}/b_z$

($m = 1$ and $k_BT = 1$ in all simulations), $s = 0.15$, and $r_c = b_z/4$. Furthermore, friction coupling of squirmers to fluid flow is performed using DPD parameters $a = 0$, $\gamma = 100\sqrt{mk_BT}/b_z$, $s = 0.1$, and $r_c = 0.175b_z$. These together yield a fluid dynamic viscosity of $\eta = 403.2\sqrt{mk_BT}/b_z^2$. The time step for integration is $1.25 \times 10^{-3} b_z \sqrt{m/k_BT}$.

The membrane-like representation of spheroidal squirmers has $N_v = 1024$, and the shear modulus $\mu_0 = 1.44 \times 10^5 k_BT/b_z^2$, the bending modulus $\kappa = 250k_BT$, the area-constraint coefficients $k_d = 1.6 \times 10^3 k_BT/b_z^2$ and $k_a = 8 \times 10^3 k_BT/b_z^2$, the volume-constraint coefficient $k_v = 3.2 \times 10^4 k_BT/b_z^3$, the total area $A_0^{tot} = 5.36b_z^2$, and the total volume $V_0^{tot} = 1.05b_z^3$. Excluded-volume interactions between different squirmers and between squirmers and the walls are implemented through the LJ potential with parameters $\epsilon_{LJ} = k_BT$ and $\sigma_{LJ} = 0.125b_z$. The computed three-dimensional rotational diffusion coefficient around the major axis of a spheroid without confinement is $D_R = 3.28 \times 10^{-4}\sqrt{k_BT/m}/b_z$, which is close to the theoretical prediction of $D_R = 3.52 \times 10^{-4}\sqrt{k_BT/m}/b_z$ (Theers et al., 2016b). To present simulation results, the half length b_z of the semi-major axis is chosen as a length scale, and the characteristic rotational time $\tau_R = 1/D_R$ as a time scale. In all simulations, the activity parameter B_1 is fixed at $56.8b_zD_R$. We have verified that the swimming velocity of a single squirmer is $U_0 = 45.5b_zD_R$, in agreement with the theoretical prediction (Theers et al., 2016b). Using these values, we can define a dimensionless Péclet number $Pe = U_0/(2b_zD_R) \approx 28.4$. Furthermore, the Reynolds number $Re = 2b_zU_0mn_f/\eta \approx 0.03$ is small enough to eliminate possible inertial effects.

Different volume fractions $\phi = 4N_{sq}\pi b_x b_y b_z/(3L^2H) \in \{0.18, 0.35, 0.44, 0.56\}$ are considered, corresponding to different numbers of squirmers $N_{sq} \in \{228, 456, 576, 720\}$. The three values of active stress $\beta \in \{-5, 0, 5\}$ represent simulation systems with pusher, neutral, and puller swimmers, respectively. Finally, we also consider two values of the non-dimensional rotlet dipole strength $\tilde{\lambda} = \lambda/(b_z^4 D_R) \in \{0, 133.5\}$. For $\tilde{\lambda} = 133.5$, a single squirmer moves in a circular trajectory at a wall with a radius of approximately $2b_z$. For comparison, the rotlet dipole strength of $\tilde{\lambda} \in \{0, 561.1\}$ has been used in Qi et al., 2022, where squirmers were confined to a single layer. All simulations are first run for a time of at least $1.5\tau_R$ to reach a steady state, and afterwards various structural and dynamical characteristics of the system are measured during the time $1.5\tau_R$.

4.1.3 Mapping to experimental systems

Squirmer parameters used in simulations can also be mapped to the properties of real swimmers. In the far-field approximation, the hydrodynamic field of a microswimmer is dominated by its force-dipole strength $\chi = f_d l_d/(8\pi\eta)$ (Solon et al., 2015; Drescher et al., 2011; Lauga and Powers, 2009), where f_d and l_d are the characteristic force and length of the dipole. The active stress β of a spheroidal squirmer can be expressed as (Theers et al., 2016b)

$$\beta = -\frac{\chi}{U_0(b_z^2 - b_x^2)} \frac{[3\tau_0 + (1 - 3\tau_0^2)\coth^{-1}\tau_0][\tau_0 - (\tau_0^2 - 1)\coth^{-1}\tau_0]}{2/3 - \tau_0^2 + (\tau_0^2 - 1)\coth^{-1}\tau_0}. \tag{4.2}$$

Average properties of *E. coli* bacteria swimming in water correspond to $U_0 = 29$ μm/s, $f_d = 0.42$ pN, $l_d = 1.9$ μm, $b_z = 1.5$ μm, $b_x = 0.5$ μm, and $\eta = 10^{-3}$ Pa·s (Drescher et al., 2011; Hu et al., 2015a; Darnton et al., 2007), resulting in $\beta \approx -3$. Note that a direct comparison is possible only in the far-field limit, while the near-field flow of each swimmer depends on its geometric and propulsion details.

4.2 Results

In our investigation, we analyze the collective structural and dynamical properties of swimmer ensembles in thin fluid films as a function of volume fraction ϕ and squirmer characteristics of active stress β and rotlet dipole strength $\tilde{\lambda}$. Snapshots of the emergent structures are displayed in FIGURE 4.2. We characterize these phases through the analysis of cluster sizes and radial distribution functions of the squirmers. Furthermore, the distribution of squirmers along the h-direction (perpendicular to the walls) and their orientation are considered to distinguish a two-layered arrangement with an average orientation within the $x-z$ plane from the stacked packing with the orientation perpendicular to the walls. Finally, dynamical properties, such as velocity distribution, and effective rotational and translational diffusivities, are computed to characterize squirmer motility within collective states.

An important question for any two-layered structure is to which extent the two layers interact with and affect each other. The snapshots in FIGURE 4.2 nicely demonstrate that the correlation between the two layers strongly depends on volume fraction and strength of the rotlet dipole. Without rotlet dipole, i.e. for $\tilde{\lambda} = 0$, the layer correlation is very weak for small ϕ, but becomes very significant for large ϕ, where the clusters in the top and bottom layers are essentially in registry. With strong rotlet dipole, i.e. for $\tilde{\lambda} = 133.5$, the situation is very different, as there is hardly any visible correlation between the two layers.

Previous studies of structure formation of artificial and biological microswimmers in two- and three-dimensional systems (Elgeti, Winkler, and Gompper, 2015; Qi et al., 2022; Bechinger et al., 2016; Bialké, Speck, and Löwen, 2012; Levis and Berthier, 2014) report the existence of various phases, including

- a gas of small clusters, where the distribution of swimmers is homogeneous and dynamic clusters are formed by a few swimmers;
- large clusters or motility-induced phase separation (MIPS), where the cluster size is often comparable with the size of the entire system; such large clusters are nearly immobile;
- swarming and flocking, which is characterized by the collective locomotion of dense swimmer clusters with swirling and streaming patterns.

A similar behavior is found in our system (see FIGURE 4.2); however, the possibility of the formation of two distinct layers at the walls gives rise to novel structures and dynamics.

4.2.1 Structural properties

Cluster size distribution

The cluster-size distribution function $\mathcal{N}(n)$ is calculated as

$$\mathcal{N}(n) = \frac{1}{N_{sq}} n p(n), \tag{4.3}$$

where $\mathcal{N}(n)$ represents the fraction of squirmers belonging to clusters of size n, and $p(n)$ denotes the number of clusters of size n. The distribution is normalized, such that $\sum_n \mathcal{N}(n) = 1$. Different squirmers belong to the same cluster when the nearest

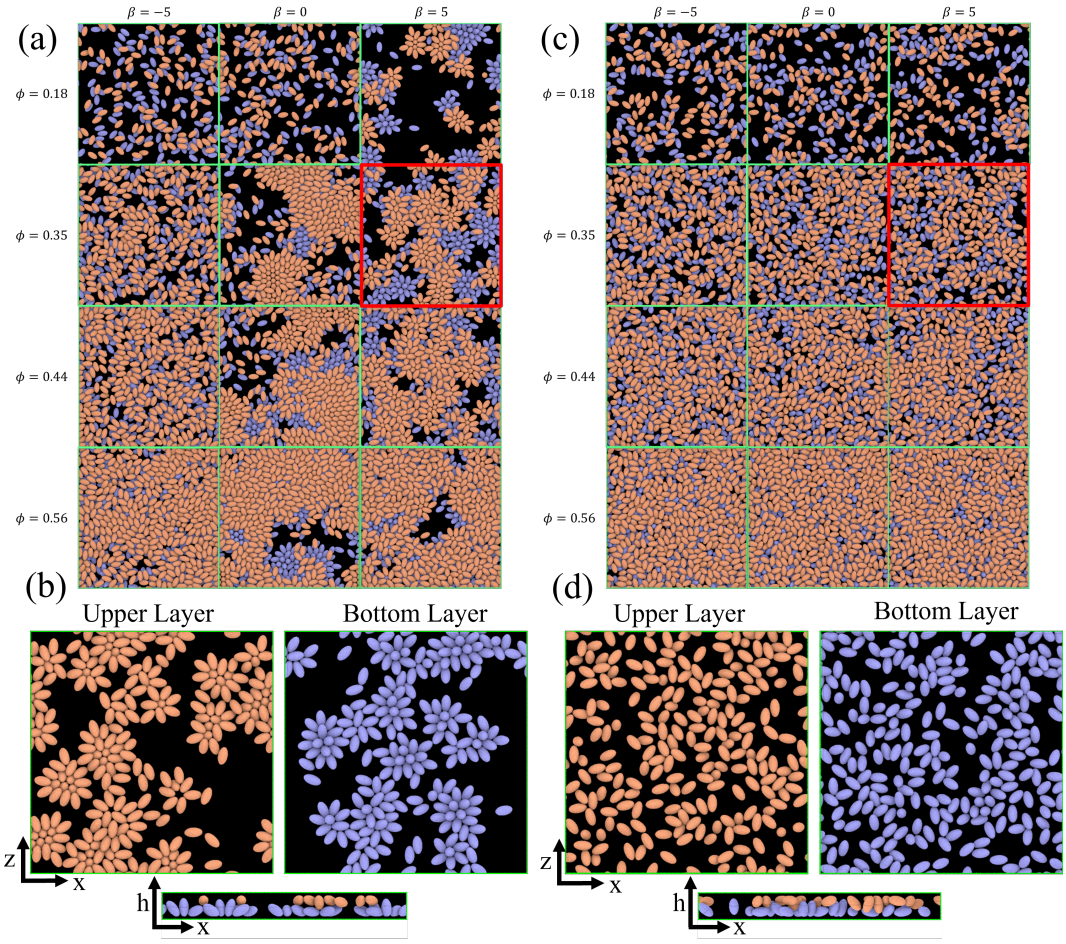

FIGURE 4.2: Snapshots of the emergent structures for different active stresses β, volume fractions ϕ, and rotlet dipole strengths $\tilde{\lambda}$. (a) Simulated structures for $\tilde{\lambda} = 0$, $\phi = 0.18$ and 0.35, and $\beta \in \{0, \pm 5\}$. Squirmers in the upper (bottom) half of the slit are colored in orange (blue). See also corresponding Movies S1 - S6. (b) Squirmer structures within the upper and bottom layers of the simulated system for $\phi = 0.35$, $\beta = 5$, and $\tilde{\lambda} = 0$. See also Movie S6. (c) Snapshots of the simulated systems for $\tilde{\lambda} = 133.5$, $\phi = 0.35$ and $\beta \in \{0, \pm 5\}$. See also Movies S7 - S9. (d) Squirmer structures within the upper and bottom layers of the slit for $\phi = 0.35$, $\beta = 5$, and $\tilde{\lambda} = 133.5$. Squirmers belong to the upper (orange) or bottom (blue) layers, when the h-coordinate of their center of mass is in the upper or lower half of the slit, respectively. See also Movie S9.

surface-to-surface distance d_s between them satisfies $d_s/b_z < 0.25$. The average cluster size $\langle n \rangle$ is then (Levis and Berthier, 2014):

$$< n >= \sum_n n\mathcal{N}(n). \tag{4.4}$$

The cluster-size distribution is used to distinguish the different collective phases (Levis and Berthier, 2014; Be'er et al., 2020) mentioned above. For the gas of small clusters, $\mathcal{N}(n)$ exhibits an exponential decay, as shown in FIGURE 4.3(a) for $\phi = 0.18$. For MIPS or large clusters, a bimodal distribution of $\mathcal{N}(n)$ is observed, with the second peak at large n signaling the presence of large clusters, see FIGURE 4.3(b,c)

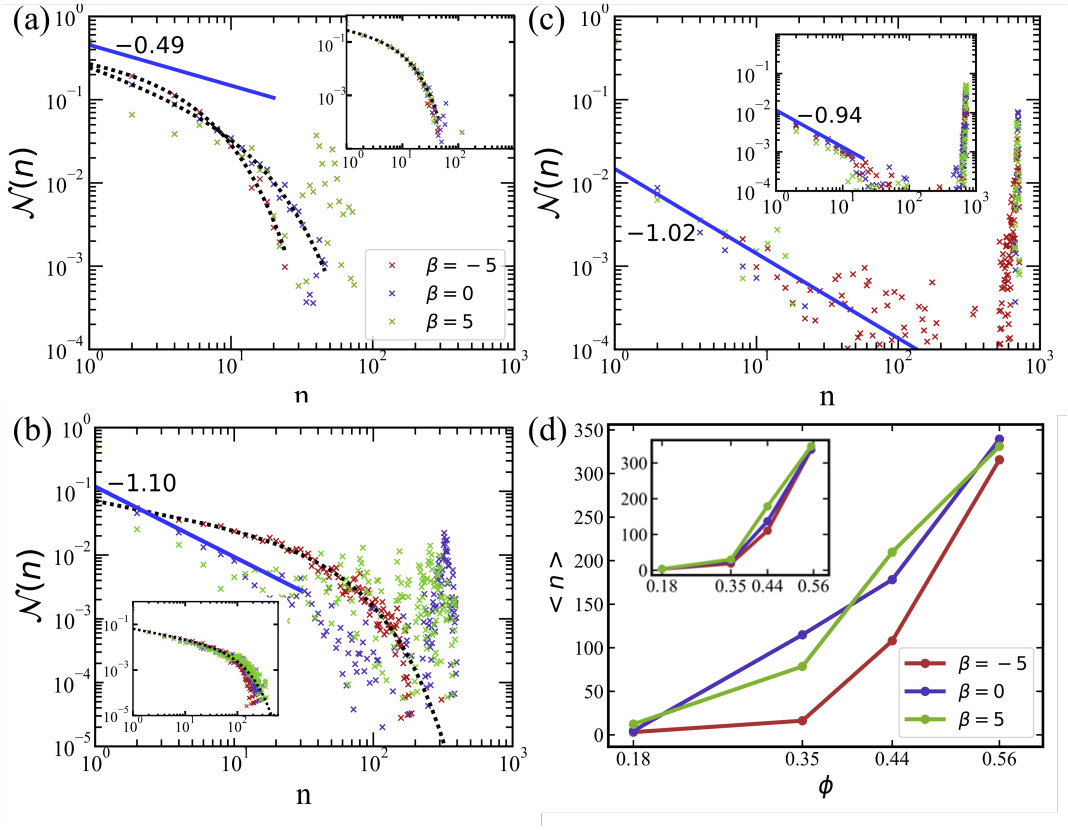

FIGURE 4.3: Cluster size distributions for different volume fractions of squirmers. (a) $\phi = 0.18$, (b) $\phi = 0.35$, and (c) $\phi = 0.56$. The curves with different colors represent various swimming modes: pusher with $\beta = -5$ (red), neutral with $\beta = 0$ (blue), and puller with $\beta = 5$ (green). The blue solid lines are the power-law fits, while the black-dotted lines are the fits using equation (4.5) with the parameters shown in Table 4.1. (d) The average cluster size for various conditions as a function of volume fraction. The average cluster size is calculated using equation (4.4). All plots are for the simulations without rotlet dipole ($\tilde{\lambda} = 0$), while the insets show data from the corresponding simulations with $\tilde{\lambda} = 133.5$.

for $\phi = 0.35$ and $\phi = 0.56$. Finally, swarming can be characterized by a power-law decay of $\mathcal{N}(n)$ with an exponential cutoff and without the presence of a distinct peak (Alarcón, Valeriani, and Pagonabarraga, 2017; Qi et al., 2022). This implies a slow decline of cluster sizes over a broad range, compared to the fast decay for a gas of small clusters.

The described characteristics of different phases can be extracted by fitting $\mathcal{N}(n)$ with the function (Alarcón, Valeriani, and Pagonabarraga, 2017)

$$f(x) = Ax^{-\gamma} \exp^{-x/\alpha}, \tag{4.5}$$

where A, γ, and α are the fitting parameters. Table 4.1 presents these parameters for different simulated conditions.

For $\phi = 0.18$, the simulated systems exhibit a homogeneous gas-like phase, except for the case of pullers ($\beta = 5$) without rotlet dipole ($\tilde{\lambda} = 0$), shown in FIGURE 4.2(a). Here, the exponential term dominates, as can be seen well in FIGURE 4.3(a). At low packing fractions of squirmers, there is a limited chance for

ϕ	β	$\tilde{\lambda}$	A	α	γ	phase
0.18	−5	0	0.33	5.07	0.19	gas
0.18	0	0	0.26	13.1	0.57	gas
0.18	5	0	0.09	–	0.49	MIPS
0.18	−5	133.5	0.32	7.1	0.4	gas
0.18	0	133.5	0.31	7.61	0.43	gas
0.18	5	133.5	0.34	8.55	0.54	gas
0.35	−5	0	0.07	49.4	0.4	swarming
0.35	0	0	0.1	–	1.1	MIPS
0.35	5	0	0.05	–	0.99	MIPS
0.35	−5	133.5	0.07	45	0.45	swarming
0.35	0	133.5	0.07	72.5	0.58	swarming
0.35	5	133.5	0.07	90	0.62	swarming
0.44	−5	0	0.04	–	0.89	MIPS
0.44	0	0	0.02	–	0.93	MIPS
0.44	5	0	0.03	–	1.28	MIPS
0.44	−5	133.5	0.03	–	0.62	MIPS
0.44	0	133.5	0.03	–	0.69	MIPS
0.44	5	133.5	0.03	–	0.83	MIPS
0.56	−5	0	0.01	–	1.02	MIPS
0.56	0	0	0.03	–	1.64	MIPS
0.56	5	0	0.01	–	0.81	MIPS
0.56	−5	133.5	0.01	–	0.9	MIPS
0.56	0	133.5	0.01	–	0.94	MIPS
0.56	5	133.5	0.01	–	1.04	MIPS

TABLE 4.1: Parameters of the cluster size distributions, obtained from fitting the simulation result with equation (4.5), for various packing fractions ϕ, active stresses β, and dimensionless rotlet dipole strengths $\tilde{\lambda} = \lambda/(b_z^4 D_R)$. A "−" sign in the α-column indicates that the exponential term in equation (4.5) is omitted, so that the fitting function becomes $f(x) = Ax^{-\gamma}$. The last column provides the classification of different simulation cases into the defined phases.

squirmer collisions, leading to a gas-like phase, compare also FIGURE 4.2. For $\beta = 5$ at $\phi = 0.18$, $\mathcal{N}(n)$ resembles a bimodal distribution, indicating the existence of large clusters ($n \approx 60$), whose formation is primarily governed by the attractive hydrodynamic field around pullers.

Swarming-like behavior is observed in several cases at $\phi = 0.35$, characterized by the relatively large values of α and moderate values of $\gamma \in [0.4, 0.7]$, indicating the dominance of the power-law term in equation (4.5). Note that for the cases of neutral swimmers and pullers (without rotlet dipole), the value of γ is close to unity, and $\mathcal{N}(n)$ exhibits a bimodal distribution in FIGURE 4.3(b), suggesting the presence of a MIPS phase. For even larger volume fraction $\phi = 0.56$, FIGURE 4.3(c) shows a prominent peak in $\mathcal{N}(n)$ at large n for all cases, which is the main characteristic for the MIPS phase. This is also confirmed in Table 4.1 through γ values close to unity. At large packing fractions, steric interactions between squirmers dominate due to crowding, so that the differences in $\mathcal{N}(n)$ for different swimming modes nearly disappear.

For squirmers without rotlet dipole ($\tilde{\lambda} = 0$), the swimming mode affects their collective behavior when the volume fraction is small enough, i.e. $\phi \lesssim 0.4$. In this

case, the local hydrodynamic flow field generated by the squirmers is relevant for cluster formation and dynamics, in agreement with previous studies (Theers et al., 2018; Qi et al., 2022). However, when the rotlet dipole is activated ($\tilde{\lambda} = 133.5$), differences in $\mathcal{N}(n)$ for various active stresses β nearly disappear, as displayed in the insets of FIGURE 4.3. With rotlet dipole, we obtain the gas phase at $\phi = 0.18$, swarming at $\phi = 0.35$, and MIPS at $\phi = 0.56$, independently of active stress – see also FIGURE 4.2(c). Note that the systems with $\phi = 0.56$ are very crowded, and MIPS is more difficult to recognize for $\tilde{\lambda} = 133.5$ in FIGURE 4.2(c) than for $\tilde{\lambda} = 0$ in FIGURE 4.2(a). Additional simulations (not shown) indicate that the suspension of squirmers with $\tilde{\lambda} = 133.5$ transits from swarming to the MIPS at $\phi \approx 0.4$.

The average cluster size $\langle n \rangle$ as a function of ϕ is shown in FIGURE 4.3(d). For $\phi \gtrsim 0.18$, $\langle n \rangle$ increases rapidly with increasing volume fraction of squirmers for all β and λ values. The simulation systems with different active stresses result in a similar range of average cluster sizes for both rotlet dipole strengths.

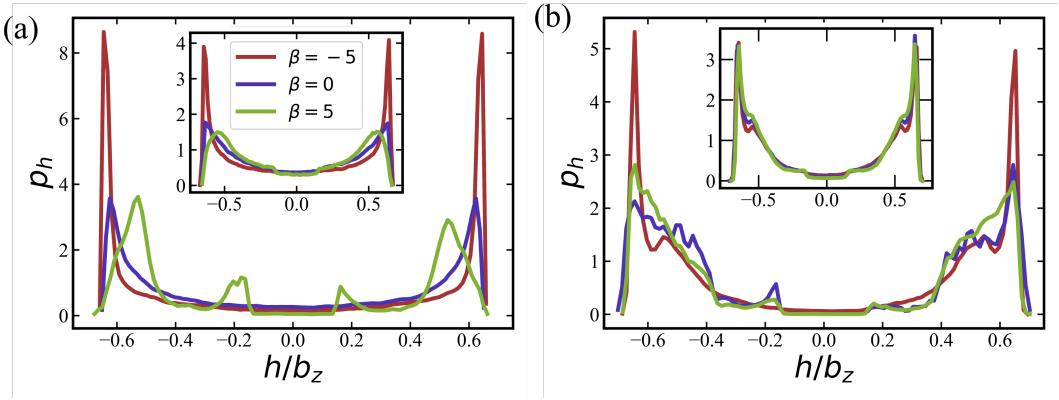

FIGURE 4.4: Distributions p_h of the squirmers' centre-of-mass position along the slit height for volume fractions (a) $\phi = 0.18$ and (b) $\phi = 0.56$. The walls are located at $h/b_z = \pm 1.25$. Colors indicate the swimming modes: pusher with $\beta = -5$ (red), neutral with $\beta = 0$ (blue), and puller with $\beta = 5$ (green). Main figures are for the simulations without rotlet dipole $\tilde{\lambda} = 0$, while the insets show the corresponding simulations with rotlet dipole $\tilde{\lambda} = 133.5$.

Squirmer distribution between the walls

Figure 4.4 shows time-averaged distributions p_h of the squirmers' center-of-mass position along the h direction between the two confining walls. Note that the symmetry of the distributions is a result of time averaging, while the number of squirmers at each wall might be different at any instant of time. However, during the course of the simulations, squirmers switch frequently between the walls (see section 4.2.2), and the localization of all squrimers at a single wall has never been observed. The distributions in FIGURE 4.4 indicate that the squirmers exhibit a distinct affinity for the walls, especially in the case of pushers, as indicated by the pronounced peaks at $h/b_z \approx \pm 0.6$. This phenomenon is primarily attributed to the well-known wall-trapping effect, which is on the one hand due to motion, steric interactions, and slow reorientation (Li and Tang, 2009; Volpe et al., 2011; Elgeti and Gompper, 2013), on the other hand due to hydrodynamic attraction (Berke et al., 2008; Lauga and Powers, 2009; Drescher et al., 2011).

Pushers ($\beta = -5$) exhibit a distinctive two-layered structure with the orientation parallel to the walls, which is reminiscent of *E. coli* behavior in *in vitro* observations (Frymier et al., 1995; Junot et al., 2022). For pushers, the far-field flow re-orients the squirmers parallel to the wall (Berke et al., 2008; Lauga and Powers, 2009; Drescher et al., 2011). Furthermore, the elongated spheroidal body of the squirmers favors their orientation parallel to the walls (Vigeant et al., 2002; Spagnolie and Lauga, 2012). For pullers ($\beta = 5$), FIGURE 4.4(a) show two small peaks at $h/b_z \approx \pm 0.2$ at small volume fraction $\phi = 0.18$, which indicates a nearly perpendicular orientation with respect to the walls [see also corresponding conformations in FIGURE 4.2(b)]. Note that the far-field flow generated by pullers favors such a perpendicular-to-the-wall orientation (Berke et al., 2008; Lauga and Powers, 2009; Drescher et al., 2011), while the spheroidal shape promotes parallel-to-the-wall orientation. Thus, pullers in FIGURE 4.4(a) show their major peaks in p_h at $h/b_z \approx \pm 0.5$, such that their most probable orientation has about 40 degree angle with respect to the walls [see also FIGURE 4.5(a)]. p_h for neutral swimmers at $\phi = 0.18$ is close to that for pushers.

At the higher volume fraction of $\phi = 0.56$, differences in p_h for the three swimming modes significantly diminish, and all cases essentially show a two-layered structure, see FIGURE 4.4(b). Note that the two peaks in p_h at $h/b_z \approx \pm 0.6$ become broader than those for $\phi = 0.18$, which can be attributed to an increasing importance of steric interactions at large volume fractions, such that close packing introduces a larger deviation to the two-layered structure. Insets in FIGURE 4.4 demonstrate that the activation of rotlet dipole mitigates the influence of active stress on p_h, in agreement with the results for the cluster-size distribution in Section 4.2.1.

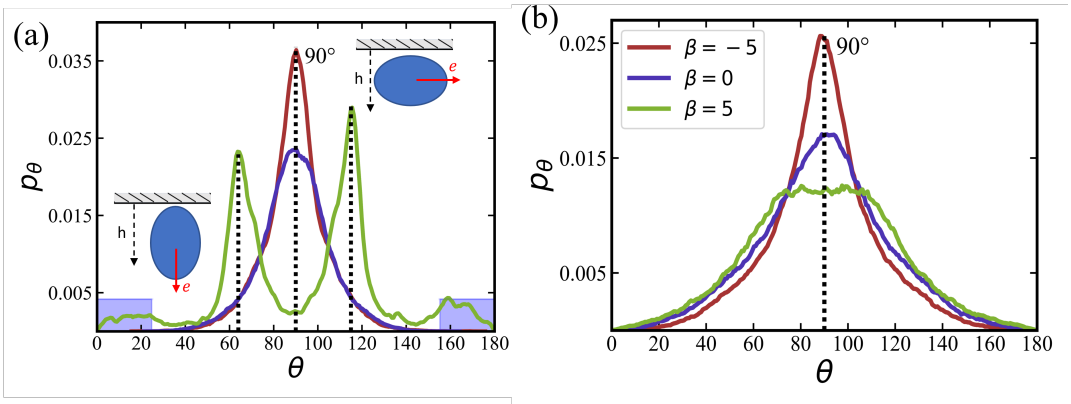

FIGURE 4.5: Orientational distribution p_θ of squirmers, where the angle θ is between the swimmer orientation vector and the h axis (wall normal axis). $\theta = 0$ and $\theta = 180$ correspond to the orientation perpendicular to the walls, while $\theta = 90$ represent the orientation parallel to the walls, see the insets. p_θ is presented for $\phi = 0.18$ with the rotlet dipole strength (a) $\tilde{\lambda} = 0$ and (b) $\tilde{\lambda} = 133.5$. The three different β values correspond to pushers ($\beta = -5$), neutral swimmers ($\beta = 0$), and pullers ($\beta = 5$). The shaded blue areas in (a) mark the angle ranges $[0, 25]$ and $[155, 180]$ used to compute the fraction of squirmers with a perpendicular orientation to the walls.

Squirmer orientation in the slit

The orientational distribution function $p_\theta(\theta)$ of the angle of the squirmer orientation vector **e** with the wall normal (h axis) are presented in FIGURE 4.5. A perpendicular orientation to the walls corresponds to $\theta = 0$ and $\theta = 180$, a parallel-to-the-wall orientation to $\theta = 90$. Figure 4.5(a) shows that pushers and neutral swimmers with $\tilde{\lambda} = 0$ at $\phi = 0.18$ are primarily oriented parallel to the wall, in agreement with the results in FIGURE 4.4(a). In contrast, pullers show several peaks at $\theta \approx 20^o$ & 160^o (small peaks) and $\theta \approx 60^o$ & 120^o (large peaks), which correspond to a nearly perpendicular-to-the-wall orientation and a tilted orientation with about 40^o angle to the walls, respectively [compare also snapshots in FIGURE 4.2(b)]. These results are consistent with the position distributions p_h discussed in Section 4.2.1.

Figure 4.5(b) shows p_θ for a non-zero rotlet dipole ($\tilde{\lambda} = 133.5$) at $\phi = 0.18$, which again demsontrates a significant reducuction of differences between different swimming modes due to the rotlet dipole. In particular, for all β, a single peak in p_θ centered around 90^o is observed, confirming the preferred squirmer orientation parallel to the walls, as illustrated in FIGURE 4.2(d). As the volume fraction of squirmers increases, the dominant role of steric interactions also leads to a diminished effect of different swimming modes (even for $\tilde{\lambda} = 0$) with the formation of a two-layered structure.

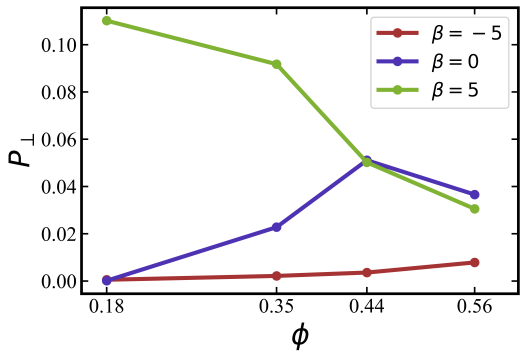

FIGURE 4.6: Probability $P_\perp$ of squirmers to be aligned with the h axis (i.e., wall normal vector) for different volume fractions and swimming modes at $\tilde{\lambda} = 0$. Data for pushers with $\beta = -5$ (red), neutral squirmers with $\beta = 0$ (blue), and pullers with $\beta = 5$ (green). The probability is calculated by integrating the orientation distributions in FIGURE 4.5(a) over the ranges [0, 25] and [155, 180] degrees.

The probability $P_\perp$ of squirmers to be oriented nearly perpendicular to the walls is displayed in FIGURE 4.6 for different values of β as a function of ϕ. The probability is computed by integrating the orientation distributions over the ranges $[0, 25^o]$ and $[155^o, 180^o]$, as indicated by the blue shaded areas in FIGURE 4.5(a). At low ϕ, the probability of perpendicular orientation to the walls is zero for pushers and neutral squirmers, while $P_\perp \approx 0.11$ for pullers. This simply confirms the tendency of pushers and neutral swimmers to align with the walls, due to their hydrodynamic interactions with the walls. Interestingly, the majority of pullers does not have a perpendicular-to-the-wall orientation, despite of such predictions for a single puller (Berke et al., 2008; Lauga and Powers, 2009). This is due to collective effects between pullers, which will be discussed in Section 4.2.1 below.

As the volume fraction of squirmers increases, $P_\perp$ for pullers decreases because steric interactions between squirmers become dominant, forcing the formation of a

two-layered structure, as discussed above. For neural squirmers, $P_\perp$ first increases with increasing ϕ, but then closely follows $P_\perp$ for pullers when $\phi \gtrsim 0.4$. For pushers, there is only a slight increase in $P_\perp$ with increasing ϕ. Nevertheless, we expect that for large volume fractions $\phi \gtrsim 0.6$, orientational differences between squirmers with various swimming modes essentially disappear.

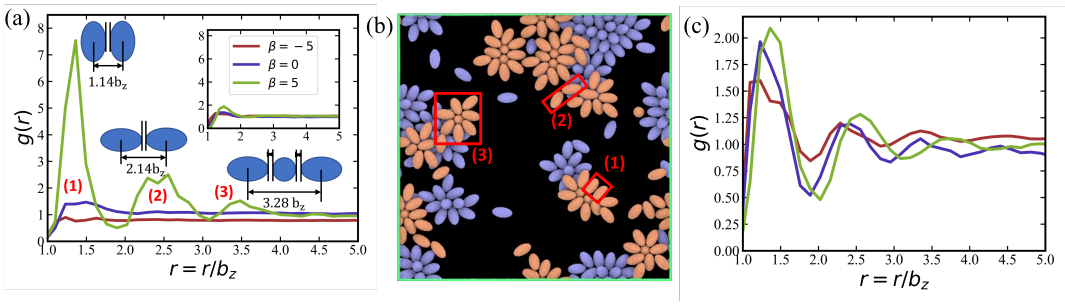

FIGURE 4.7: (a) 2D radial distribution function $g(r)$ of squirmers with $\phi = 0.18$ and $\tilde{\lambda} = 0$, for pushers (red), neutral squirmers (blue), and pullers (green). The locations of peaks of $g(r)$ for pullers correlate well with local structural arrangements illustrated next to the peaks. The inset presents the corresponding $g(r)$ functions for $\tilde{\lambda} = 133.5$ and the same ϕ. (b) Snapshot of the simulated system for $\phi = 0.18$, $\tilde{\lambda} = 0$, and $\beta = 5$, which illustrates the most frequent squirmer structures, see also Movie S3. (c) $g(r)$ of squirmers for $\phi = 0.56$ and $\tilde{\lambda} = 0$. The legend for the curves is the same as in (a).

2D radial distribution function parallel to the walls

To characterize the internal structure of the suspension of squirmers along the walls, we compute the 2D radial distribution function

$$g(r) = \frac{M}{N_{sq}^2} \left\langle \sum_i \sum_{j \neq i} \delta(\boldsymbol{r} - \boldsymbol{r}_{ij}) \right\rangle, \tag{4.6}$$

where $\boldsymbol{r}_{ij}$ is the vector between two centers of mass of squirmer pairs, and $M = A/(2\pi r)$ is a normalization factor (A is the area of the considered 2D plane) such that $g(r) \to 1$ for $r \to \infty$. Note that $g(r)$ is calculated in 2D within the $x - z$ plane, where the measurements are performed within the two layers (upper and lower halves of the slit) separately. This is a reasonable simplification due to the prevalence of a two-layered structure as shown in FIGURE 4.4.

Figure 4.7(a) presents $g(r)$ for different swimming modes at low volume fraction $\phi = 0.18$ and without rotlet dipole, $\tilde{\lambda} = 0$. Only the suspension of pullers with $\beta = 5$ exhibits pronounced peaks in $g(r)$, which represent the most frequent structural elements illustrated in FIGURE 4.7(b). The existence of structure for pullers, but not for pushers and neutral squirmers, is primarily related to the fact that pullers form large clusters already at $\phi = 0.18$, while the other squirmer types yield a gas-like phase, see Table 4.1. Interestingly, the x-y perspective plot in FIGURE 4.2(b) shows that pullers frequently form flower-like arrangements with one or two squirmers oriented perpendicular to the walls and surrounded by several "petal" squirmers [also illustrated in FIGURE 4.7(b)]. These structures form due to the attractive flow field generated by pullers, which slide along the walls until they collide and form the flower-like structures through the attractive hydrodynamic interactions. When the

rotlet dipole is turned on at $\phi = 0.18$ [see the inset in FIGURE 4.7(a)], the suspension of pullers becomes gas-like and thus looses its internal structure.

Figure 4.7(c) shows $g(r)$ at the high volume fraction $\phi = 0.56$, where several peaks are observed for all squirmer types. At this high volume fraction, all squirmer suspensions are in MIPS phase (see Table 4.1), so that large clusters are present with an internal fluid structure. Furthermore, due to the dominance of steric interactions, radial distribution functions are again very similar for different β, indicating that the internal structure is nearly independent of the swimming mode at large ϕ.

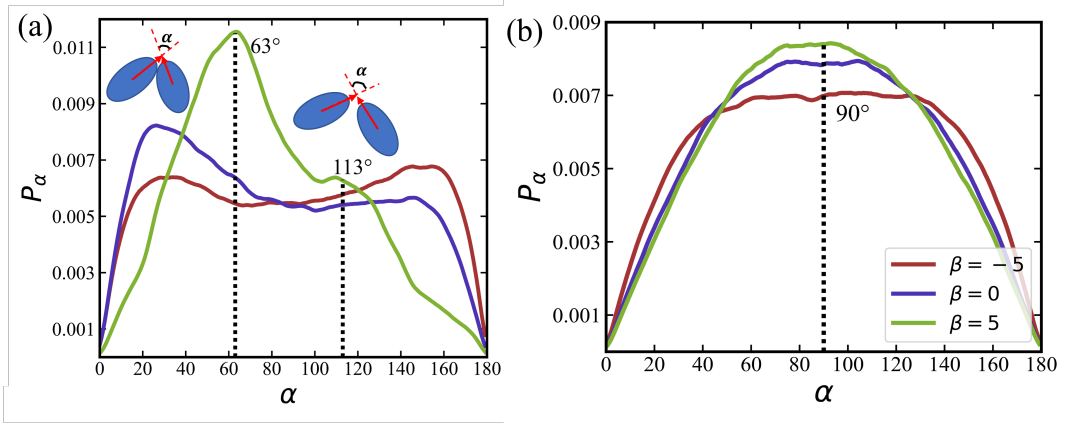

FIGURE 4.8: Distribution p_α of relative angle between two neighboring squirmers for different swimming modes at $\phi = 0.18$. α is the angle between orientation vectors of a pair of squirmers, whose separation is smaller than $3b_z$. (a) p_α for the case of no rotlet dipole ($\tilde{\lambda} = 0$), with the insets illustrating configurations of squirmers at the two peaks with $\alpha \approx 63^o$ and $\alpha \approx 113^o$. (b) Relative angle distribution for $\tilde{\lambda} = 133.5$.

Angle between two neighboring squirmers

Previous simulation studies (Theers et al., 2016b; Kyoya et al., 2015) for a monolayer of squirmers in a thin fluid between two walls have analyzed the angles between pairs of squirmers for different swimming modes. Theers et al. (Theers et al., 2016b) report that pairs of pullers tend to adopt a fixed relative angle after their initial encounter, which is equal to approximately 45^o. The stable angle formation does not occur for neutral squirmers and pushers. Similarly, Kyoya et al. (Kyoya et al., 2015) suggest that neutral squirmer pairs tend to align with each other, puller pairs assume a stable angle between them in the range of 0^o to 90^o, and pusher pairs do not show any order and swim away from each other after a brief encounter.

We calculate distributions p_α of the relative angle α between orientation vectors of two neighboring squirmers within a defined cutoff radius as

$$p_\alpha = \frac{1}{N_{sq} C} \left\langle \sum_i \sum_{j \neq i}^{|\boldsymbol{r}_j - \boldsymbol{r}_j| \leq 3b_z} \delta(\alpha - \alpha_{ij}) \right\rangle, \tag{4.7}$$

where and C is the normalization factor so that the integral of p_α is equal to unity. Figure 4.8(a) shows the distribution p_α for various β at $\phi = 0.18$. p_α for pullers displays two peaks located at $\alpha \approx 63^o$ and $\alpha \approx 113^o$, where the former value is not far from 45^o found for a monolayer of squirmers in Theers et al., 2016b. Notably, the

peak at $\alpha \approx 63^o$ is quite prominent, since it represents the flower-like arrangements illustrated in FIGURE 4.7(b). However, the distribution for pullers spans a wide range of relative angles. Neutral squirmers and pushers yield broad and nearly flat distributions, indicating that no stable structures are present. The existence of two small peaks at $\alpha \approx 25^o$ and $\alpha \approx 155^o$ suggests that pushers and neutral squirmers tend to swim parallel to each other, which is consistent with previous predictions for a squirmer pair (Ishikawa, Simmonds, and Pedley, 2006; Götze and Gompper, 2011).

The distribution of p_α for an active rotlet dipole with $\tilde{\lambda} = 133.5$ is shown in FIGURE 4.8(b). For all β values, p_α is centered at $\alpha \approx 90^o$, indicating that hydrodynamic interactions favor the perpendicular orientation between squirmer pairs. Note that for pushers, the central region in p_α is flatter than that for pullers and neutral squirmers.

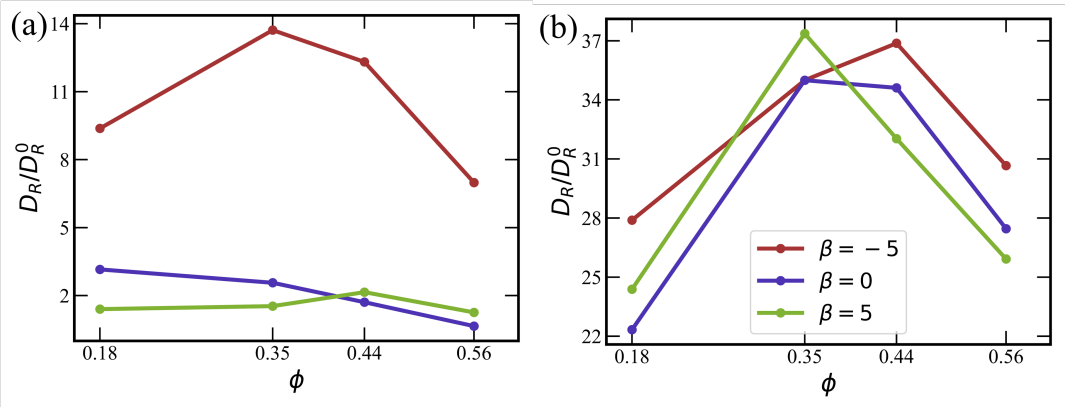

FIGURE 4.9: Effective rotational diffusion D_R as a function of ϕ for (a) $\tilde{\lambda} = 0$ and (b) $\tilde{\lambda} = 133.5$. D_R is obtained by fitting auto-correlation functions of squirmer orientation using equation (4.8), and normalized by the rotational diffusion D_R^0 of a spheroid. Data for pushers (red), for neutral squirmers (blue), and for pullers (green).

4.2.2 Dynamical properties

Effective rotational diffusion coefficient

To characterize the rotational properties of squirmers, we compute their effective rotational diffusion coefficient D_R, obtained by fitting the auto-correlation function of squirmer orientation

$$< \mathbf{e}(t) \cdot \mathbf{e}(t + \Delta t) >= e^{-D_R \Delta t}, \tag{4.8}$$

where $< \cdots >$ denotes the average over all squirmers and all times in the simulated system. Here, the exponential decay applies for small $\Delta t \lesssim 1/D_R$. FIGURE 4.9 shows the dependence of D_R on ϕ, β, and λ. In most cases, $D_R/D_R^0 > 1$, indicating that the rotational dynamics of squirmers within a suspension is enhanced in comparison with the rotational diffusion D_R^0 of a spheroid in an unconfined system. This is due to hydrodynamic interactions between squirmers, and their collisions during motion. Only for the case of $\beta = 0$, $\phi = 0.56$, and $\tilde{\lambda} = 0$, rotational diffusion is reduced, $D_R < D_R^0$, which is likely due to the crowding of squirmers at large volume fractions [compare FIGURE 4.2(a)].

Figure 4.9(a) ($\tilde{\lambda} = 0$) shows that the enhancement of rotational diffusion coefficient for pushers is significantly larger than for pullers and neutral squirmers. This occurs due to repulsive hydrodynamic interactions between pushers (Theers et al., 2016b; Kyoya et al., 2015), which lead to the enhanced scattering between squirmers. The dependence of D_R on ϕ first exhibits an increase, followed by a maximum and subsequent decrease. With increasing ϕ, the collision rate between squirmers increases, resulting in the enhancement of D_R. However, at large ϕ, squirmer clustering and the transition to the MIPS phase take place [compare FIGURE 4.2(a)], so that the effective rotational diffusion is significantly slowed down.

Noteworthy is the difference in D_R for $\tilde{\lambda} = 0$ and $\tilde{\lambda} = 133.5$ in FIGURE 4.9(a) and (b), respectively, where the enhancement for squirmers with rotlet dipole is at least a factor three larger than that without. Interestingly, squirmers with $\tilde{\lambda} = 133.5$ switch between the two layers (i.e. migrate from one wall to the other) much more frequently than squirmers with $\tilde{\lambda} = 0$, which will be discussed in section 4.2.2. The ability of interchange between the two layers increases significantly the effective rotational diffusion. The D_R curves for $\tilde{\lambda} > 0$ are similar for different swimming modes β, in agreement with the structural characteristics for suspensions of squirmers with the rotlet dipole, as discussed in section 4.2.1 above.

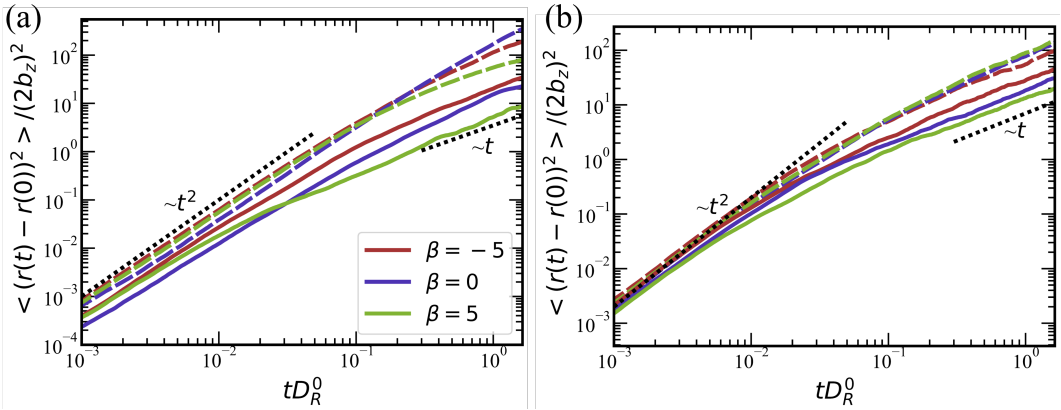

FIGURE 4.10: Mean-squared displacement of squirmers for $\phi = 0.18$ (dashed lines) and $\phi = 0.56$ (solid lines) (a) without the rotlet dipole $\tilde{\lambda} = 0$ and (b) with the rotlet dipole $\tilde{\lambda} = 133.5$. Curves for pushers are in red, for neutral squirmers in blue, and for pullers in green. Black dotted lines indicate power-laws $\sim t^2$ in the ballistic regime and $\sim t$ in the diffusive regime.

Mean-square displacement

The mean-square displacement of squirmers for various conditions are shown in FIGURE 4.10. The motion is ballistic at short times, with a quadratic time-dependence, and diffusive at long times, with $< (r(t) - r(0)) >^2 \sim t$, as expected. For $\phi = 0.18$ and $\tilde{\lambda} = 0$, pullers yield the lowest effective diffusivity, followed by neutral squirmers and pushers, because the suspension of pullers at these conditions is already in the MIPS phase (see Table 4.1). The effective diffusivity of squirmers at $\phi = 0.56$ is lower than at $\phi = 0.18$ due to crowding and the formation of large clusters.

The transition from the ballistic to the diffusive regime for $\tilde{\lambda} = 0$ in FIGURE 4.10(a) occurs around $tD_R^0 \simeq 0.2 - 0.5$. Theoretically, this transition should take place around $tD_R \simeq 1$ (Romanczuk et al., 2012), which is consistent with the values of $D_R/D_R^0 \simeq 2$ in FIGURE 4.9(a). Note that the ballistic-to-diffusive transition for

squirmers with rotlet dipole occurs at $tD_R^0 \gtrsim 0.1$, which is also consistent with the values of $D_R/D_R^0 \simeq 10$ in FIGURE 4.9(b). Furthermore, mean-square-displacement curves for $\tilde{\lambda} = 133.5$ in FIGURE 4.10(b) are similar to each other for various β at a fixed volume fraction, confirming once more that the rotlet dipole nearly offsets the effects of different swimming modes.

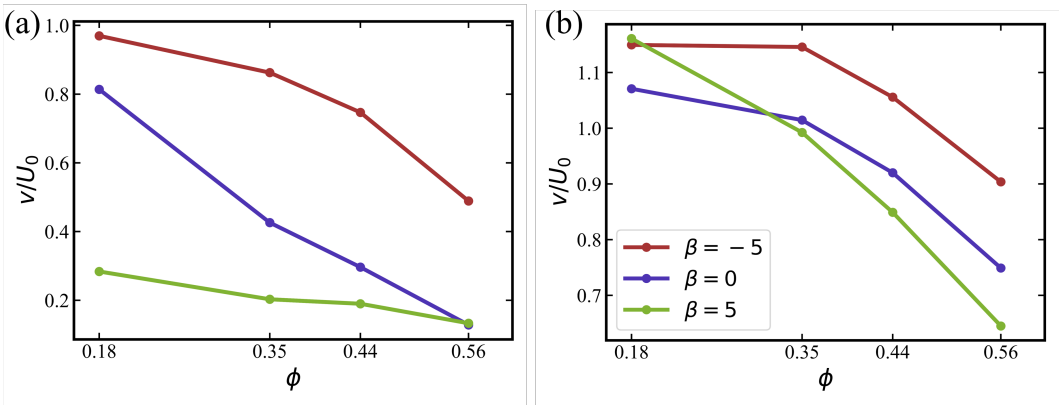

FIGURE 4.11: Average squirmer speed $\bar{v}$ as a function of ϕ for (a) $\tilde{\lambda} = 0$ and (b) $\tilde{\lambda} = 133.5$. The speed is normalized by the swimming speed U_0 of a squirmer in an unconfined system. Data for pushers (red), for neutral squirmers (blue), and for pullers (green).

Average squirmer speed

To further characterize the mobility of squirmers for different conditions, we also study the average squirmer speed $\bar{v}$. For a single squirmer i, the instantaneous swim speed is calculated as

$$v_i(t) = |\mathbf{r}_i(t + \Delta t) - \mathbf{r}_i(t)|/\Delta t, \tag{4.9}$$

with time interval $\Delta t = 0.022/D_R$ (significantly smaller than $1/D_R$), during which a free squirmer moves a distance b_z. $\bar{v}$ is then obtained by an ensemble and time average as a function of the volume fraction ϕ.

As shown in FIGURE 4.11, pushers are the most mobile, displaying the largest average speed $\bar{v}$ among all squirmer types. For the case without rotlet dipole in FIGURE 4.11(a), $\bar{v}$ decreases with increasing ϕ due to crowding at large volume fractions and the transition to MIPS or clustering regime. For all studied β values, the average speed of squirmers is below U_0, which is the speed of a single squirmer in an unconfined system.

The average speeds of squirmers with rotlet dipole in FIGURE 4.11(b) are larger than those with $\tilde{\lambda} = 0$. Furthermore, the decay in $\bar{v}$ for $\tilde{\lambda} = 133.5$ with increasing ϕ is slower than for $\tilde{\lambda} = 0$. Interestingly, for $\phi \lesssim 0.4$, the average speed of squirmers with rotlet dipole is slightly larger than U_0, indicating motility enhancement due to interactions with the walls. An increased mobility near walls was reported previously for pushers without rotlet dipole (Kyoya et al., 2015; Lintuvuori et al., 2016; Spagnolie and Lauga, 2012). The results in FIGURE 4.11 confirm that the presence of rotlet dipole enhances the mobility of squirmers and delays the transition to MIPS as a function of ϕ.

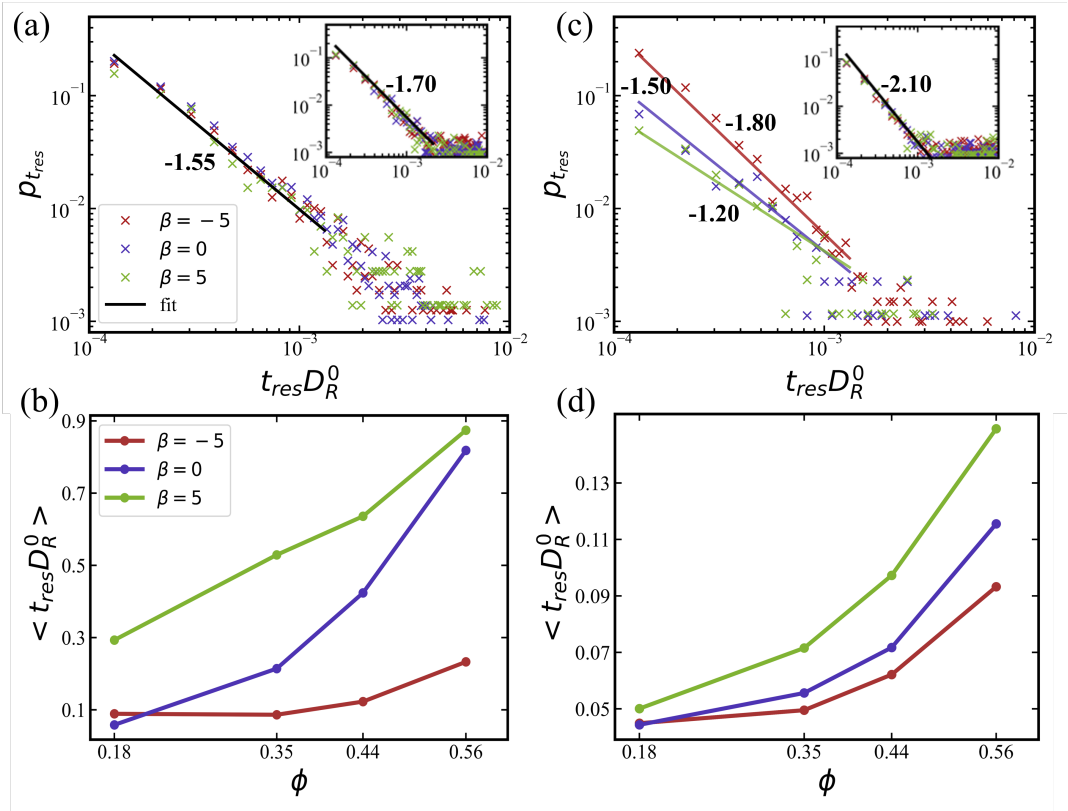

FIGURE 4.12: Distributions of squirmer residence times t_{res} within one of the layers for (a) $\phi = 0.18$ and (c) $\phi = 0.56$ without rotlet dipole ($\tilde{\lambda} = 0$). Symbol colors represent different swimming modes: pusher with $\beta = -5$ (red), neutral with $\beta = 0$ (blue), and puller with $\beta = 5$ (green). The lines are power-law fits with the exponents indicated. Insets in (a) and (c) show the distributions $p_{t_{res}}$ for simulations with rotlet dipole ($\tilde{\lambda} = 133.5$). Average residence times $\langle t_{res} \rangle$ as a function of volume fraction for different squirmers (b) without rotlet dipole and (d) with rotlet dipole.

Migration between the two layers

Due to the dominance of two-layered squirmer structures for nearly all conditions (see FIGURE 4.4), an interesting quantity is the switching frequency of individual squirmers between the layers. The switching frequency is inversely proportional to the squirmer residence time t_{res} defined as the time during which a squirmer remains within one of the layers before switching to the other one. Figure 4.12(a,c) presents the distributions $p_{t_{res}}$ of residence times for $\phi = 0.18$ and $\phi = 0.56$. For short residence times, $p_{t_{res}}$ exhibits a power-law behavior which is shown by the power-law fits with exponents indicated. Note that the distributions $p_{t_{res}}$ have very long tails, but the data for long residence times are noisy due to limited statistics. For $\phi = 0.18$, distributions of t_{res} appear to be similar to each other for different swimming modes, at least for short residence times. For $\phi = 0.56$, the differences in $p_{t_{res}}$ are clearly visible, and pushers yield the lowest exponent in comparison to neutral squirmers and pullers.

In fact, it is more informative to look at average residence times $\langle t_{res} \rangle$, which are shown in FIGURE 4.12(b,d) for simulations without and with rotlet dipole. Pushers display the lowest values of $\langle t_{res} \rangle$ in comparison to the other two swimming modes,

regardless of the rotlet dipole strength. This means that pushers have the highest switching frequency, which is consistent with previous studies (Ishimoto and Gaffney, 2013; Theers et al., 2016b; Schaar, Zöttl, and Stark, 2015; Lintuvuori et al., 2016; Zöttl and Stark, 2018) showing that the residence of pushers near a wall is unstable due to local hydrodynamic interactions which orient them slightly away from the wall. The average residence time increases with increasing ϕ for all squirmer types due to significant crowding at large ϕ, which limits the migration between the two layers. Pullers possess the largest average residence times, which is consistent with their preferred orientation toward a wall (see section 4.2.1) as well as with the formation of stable flower-like structures (see section 4.2.1). It is likely that switching between the two layers for pullers is facilitated by squirmer collisions, rather than occurring spontaneously.

Finally, for squirmers with a rotlet dipole ($\tilde{\lambda} = 133.5$), average residence times are about one order of magnitude lower than for squitmers without rotlet dipole. Therefore, the presence of rotlet dipole significantly destabilizes the residence of squirmers near walls, and thereby enhances their switching frequency between the two layers. It is also consistent with an enhanced motility of squirmers with rotlet dipole, as shown in FIGURE. 4.9 and 4.11.

4.3 Discussion and conclusions

In this study, we have performed mesoscale hydrodynamic simulations of a confined system of squirmers in a thin fluid film between two parallel walls, in order to better understand the intricate interplay between hydrodynamic and steric interactions and their impact on the collective behavior of squirmers. In contrast, previous studies that considered hydrodynamic interactions between swimmers have mainly focused on quasi-2D systems (i.e., a monolayer of squirmers) (Theers et al., 2018; Qi et al., 2022; Kyoya et al., 2015; Alarcón, Valeriani, and Pagonabarraga, 2017; Zöttl and Stark, 2014; Yoshinaga and Liverpool, 2017; Blaschke et al., 2016) or 3D systems with periodic boundary conditions (Ishikawa and Pedley, 2007; Delmotte et al., 2015; Ishikawa, Locsei, and Pedley, 2008; Evans et al., 2011; Alarcón and Pagonabarraga, 2013). The considered film thickness is large enough to allow the formation of two-layered structures. This situation is of interest when the formation of a biofilm, which starts from a monolayer of bacteria, proceeds toward the development of further layers. In particular, an interesting question is whether bacteria can spontaneously leave the surface layer.

By systematically varying relevant parameters, such as the volume fraction of squirmers, their active stress, and their rotlet dipole strength, we show the emergence of different structures and phases (FIGURE 4.2). As expected, at low volume fractions of squirmers, the system is in a gas-like phase. As ϕ is increased, a swarming state is observed, with the formation of mobile clusters with a wide range of sizes. The elongated shape of squirmers is essential for the emergence of these swarming clusters, as it provides an alignment interaction, which has been observed previously for self-propelled rods, spheroids, and semi-flexible filaments (Peruani, Deutsch, and Bär, 2006; Theers et al., 2018; Duman et al., 2018). Swarming clusters form at intermediate values of ϕ for pushers and squirmers with the rotlet dipole. The absence of the swarming state for pullers with $\tilde{\lambda} = 0$ suggests that attractive hydrodynamic interactions between swimmers suppress the formation of swarming clusters.

At large enough volume fractions, a single large cluster of squirmers emerges, surrounded by a few mobile swimmers (see FIGURE 4.2(a) at $\phi = 0.44$ or 0.56), indicating formation of MIPS. Pullers exhibit MIPS already at low volume fraction, $\phi \approx 0.18$, while neutral squirmers and pushers require larger volume fractions, in agreement with previous studies (Theers et al., 2018; Kyoya et al., 2015). Our simulations also suggest that hydrodynamic interactions suppress motility-induced clustering and phase separation, in agreement with previous reports (Theers et al., 2018; Matas-Navarro et al., 2014) for particles with aspect ratios not far from unity. Note that the suspension of pushers at $\phi = 0.56$ does not show a transition to the state of active turbulence, because the strength of the induced force dipole is likely too weak (Stenhammar et al., 2017; Martinez et al., 2020).

An interesting aspect of our investigation is the interplay of simultaneous hydrodynamic and steric interaction both between squirmers and of squirmers with the confining walls, and its effect on the collective behavior. In particular, pullers favor a nearly perpendicular orientation with the walls, resulting in the formation of flower-like clusters [FIGURE 4.2(b)] at low volume frations, where pullers first slide along the surface, and upon collisions form a structure with a single puller oriented nearly perpendicular to the wall surrounded by a few petal pullers. This leads to the nucleation of clusters for pullers already at low ϕ, promoting MIPS at low ϕ. Pushers and neutral squirmers favor an orientation parallel to the walls, which does not significantly hinder their mobility. Therefore, pushers can frequently switch between the layers of a two-layer structure, substantially delaying the formation of large clusters with increasing ϕ. Thus, a colony of pusher-like swimmers (e.g., *E. coli*) should be able to spontaneously switch from an initial monolayer structure to a multi-layered configuration. Recent experiments (Junot et al., 2022) suggest that *E. coli* bacteria also employ tumbling (i.e., active turning due to the rotation reversal of one of its flagella) to leave a surface, indicating that the aspect ratio of a swimmer is very important for its interaction with the wall. In our simulations, $b_z/b_x = 2$, which is somewhat smaller than that for *E. coli*.

For all studied cases, there is a clear preference for the two-layered structure. Only pullers at $\phi \lesssim 0.25$ show partial preference for the perpendicular-to-the-wall orientation due to their hydrodynamic interactions with the walls. Pushers and neutral squirmers display mostly parallel-to-wall alignment.

Our comprehensive simulations reveal that the the effect of a rotlet dipole is to offset the effect of active stress, characterized by β, to a large extent. Even at relatively low volume fractions, the presence of a rotlet dipole of dimensionless strength $\tilde{\lambda} \neq 0$ nearly eliminates differences in the behavior of pullers, neutral squirmers, and pushers. With the rotlet dipole, squirmers assume a parallel-to-the-wall orientation and therefore, remain mobile up to moderate volume fractions, frequently switching between the two layers. This enhancement of layer switching can be attributed to the rotational flow field of rotors, which implies an induced motion around their center of mass. Furthermore, the rotlet dipole leads to a circular trajectories of squirmers near the walls (Lauga et al., 2006; Hu et al., 2015b), which further contributes to the mobility of squirmers within the confinement. In our study, a single squirmer with $\tilde{\lambda} = 133.5$ circles at the wall with a radius of approximately $2b_z$. However, the circling motion near a wall is difficult to detect at higher volume fractions due to frequent squimer-squirmer scattering. As a result, the effective rotational diffusivity of squirmers with rotlet dipole is approximately one order of magnitude larger than that for squirmers with $\tilde{\lambda} = 0$. Thus, swimmers with rotlet dipole are expected to spontaneously initiate multi-layered structures within a biofilm.

Finally, we would like to discuss some limitations of our study. Despite the fact

that the squirmer model can produce various swimming modes, the near-field flow of real microswimmers, like bacteria, is unavoidably species-specific, arising from body shape, the geometry and dynamics of propelling flagella, and the ability to navigate (e.g., *E. coli* tumbling). Furthermore, steric interactions between microswimmers including their flagella are likely different from interactions between idealized spheroidal shapes. However, modeling of swimmers with explicit appendages (Hu et al., 2015b) is computationally expensive, significantly limiting the number of simulated swimmers in a study. Therefore, the direct comparison of our simulation results with experiments requires some calibration, including the aspect ratio of squirmers, and the strengths of active stress and rotlet dipole. Furthermore, biofilms *in vivo* are generally bound by a solid wall and an air-water interface, in contrast to the two solid walls in our study. The air-water interface is deformable and such simulations are beyond the scope of our work. However, our setup with the two non-slip walls may capture qualitatively the collective behavior of bacteria in porous media and microfluidic devices (Keymer et al., 2006; Bhattacharjee and Datta, 2019; Frangipane et al., 2019). Future work should also consider thicker films to bridge these results with those from three-dimensional periodic systems (Ishikawa and Pedley, 2007; Delmotte et al., 2015; Ishikawa, Locsei, and Pedley, 2008; Evans et al., 2011; Alarcón and Pagonabarraga, 2013).

Chapter 5

E. coli Characteristics on Run and Tumble Behavior

A huge variety of existing microorganisms motivates fundamental studies of their behavior with a possibility to construct their mimics. A prominent example is *E. coli* bacterium which employs several helical flagella for propulsion to explore the environment and seek for nutrition. This type of bacteria alternates between run (direct swimming) and tumble (change in the swimming direction) phases to navigate within a fluidic environment. Even though the run-and-tumble behavior of *E. coli* seems to be simple, physical properties and mechanisms that enable this dynamics are still poorly understood. We establish a detailed *E. coli* model, which is coupled to fluid flow described by the dissipative particle dynamics method, and investigate its run-and-tumble behavior. Different *E. coli* characteristics, including body and flagella geometry, flagella bending rigidity, the number of flagella and their arrangement at the body, and the strength of applied torque to each flagellum, are considered. In particular, the rigidity of a hook (the short part of a flagellum which connects it directly to the motor), polymorphic transformation (spontaneous change in flagella helicity) of flagella, and their arrangement at the body surface strongly influence the run-and-tumble behavior. As a result, the developed model helps us better understand physical mechanisms which govern *E. coli* dynamics, yielding the run-and-tumble behavior that compares well with available experimental observations. This model can further be used to explore the behavior of *E. coli* in more complex realistic environments.

In our work, we establish a detailed model of *E. coli* and investigate its run-and-tumble behavior in comparison to available experimental observations. We show that the body geometry strongly affects the balance between rotational frequencies of the body and flagella bundle, which may significantly limit successful tumbling of *E. coli*. Furthermore, both the polymorphic transformation and the stiffening of the hook of tumbling flagella play important roles in an efficient change of the swimming direction. In particular, they govern the efficient separation of tumbling flagella from the bundle. Our model helps us better understand the importance of different *E. coli* characteristics for the run-and-tumble behavior, which agrees well with experimental observations. In fact, this model should be thought of as a set of different *E. coli* models, since we show that different number of flagella and their random placement at the body can produce a variety of *E. coli* behaviors, which is also the case in experiments. This model can further be used to investigate *E. coli* behavior in complex environments, such as near surfaces and in complex geometries.

5.1 Methods and models

The details of the bacterium model is shown in section 3.3. Fluid flow is modeled by the dissipative particle dynamics (DPD) method detailed in section 3.4.1.

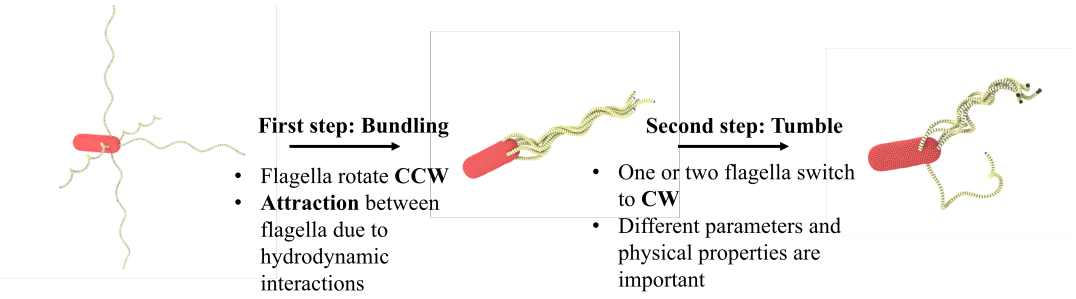

FIGURE 5.1: The workflow of simulations in our work.

5.2 Simulation setup and parameters

We define a length scale as the length of the major half-axis b_x ($b_x = 9$ in simulation units), a time scale τ ($\tau = 132$ in simulation units) as the period of bundle rotation, and an energy scale as k_BT ($k_BT = 1$ in all simulations). Simulations are performed in a domain with dimensions $8.33b_x \times 11.56b_x \times 11.56b_x$. Each simulation contains a single bacterium and 2.4×10^6 fluid particles with a number density of $n_d = 2.16 \times 10^3 b_x^{-3}$. DPD parameters for the interactions between fluid particles and between fluid particles and wall particles are $a = 540k_BT/b_x$, $\gamma = 225\sqrt{mk_BT}/b_x$ ($m = 1$ and $k_BT = 1$), $s = 0.15$ and $rc = 0.11b_x$. Frictions between the *E. Coli* and fluid particles or wall particles is simulated by DPD interactions with the parameters of $a = 0$, $\gamma = 360\sqrt{mk_BT}/b_x$, $s = 0.1$ and $r_c = 0.09b_x$. These yield a fluid dynamic viscosity of $\eta = 1225.53\sqrt{mk_BT}/b_x^2$. The simulations are run for a total duration of approximately 113.64τ, and the time step Δt of integration is $2.27 \times 10^{-5}\tau$.

The body of *E. coli* is discretized by $N_v = 1278$ particles. The corresponding surface has a shear modulus of $\mu_0 = 8.1 \times 10^4 k_BT/b_x^2$ and the bending modulus $\kappa = 100k_BT$. The area and volume constraints assume $k_d = 8.1 \times 10^4 k_BT/b_x^2$, $k_a = 4.05 \times 10^4 k_BT/b_x^2$, and $k_v = 3.65 \times 10^5 k_BT/b_x^3$, with the body area $A_0^{tot} = 4.21b_x^2$ and the body volume $V_0^{tot} = 0.62b_x^3$. In simulations, we set $K_{el}^3 = 10^4 k_BT$, which is large enough to prevent significant twisting of flagella during rotation. $K_{el}^1 = K_{el}^2$ are set in the range between $2 \times 10^3 K_BT$ and $5 \times 10^4 K_BT$, corresponding to bending stiffnesses $K_{flag} = K_{el}^1 b_x$ between $1.7 \times 10^{-23}\ Nm^2$ and $4.2 \times 10^{-22}\ Nm^2$. These values are within the range of experimentally measured bending stiffnesses $10^{-24} - 10^{-21} Nm^2$ (Hu et al., 2015a). Furthermore, $\Omega_e^1 = 0.122$, $\Omega_e^2 = -0.027$, and $\Omega_e^3 = -0.217$, defining a left-handed helix in equilibrium with a radius of $0.23\mu m$ and a pitch length of $2.56\mu m$ (Darnton et al., 2007). Each flagellum consists of $N_s = 76$ segments, resulting in three helical turns. A basic *E. coli* model has five flagella, with one attached at one body end and four attached symmetrically to the side closer to the end [see Fig. 5.3(a)].

Excluded-volume interactions between the body and flagella or between different flagella are implemented through the LJ potential with parameters $\epsilon_{LJ} = k_BT$ and $\sigma_{LJ} = 0.07b_x$. Coupling between the *E. coli* model and fluid flow results in a haracteristic Reynolds number $Re = b_x m n_d v/\eta \approx 0.01$. The value is small enough

to neglect inertial effects. Here, $v \approx 5.22 \times 10^{-3}\sqrt{K_B T/m} = 0.077 b_x \tau^{-1}$ is the swimming speed of *E. coli*.

Simulations are carried out in two steps (see FIGURE 5.1). In the first step, *E. coli* with initially unbundled flagella (all rotating anti-clockwise) is let to swim and form a tight bundle due to hydrodynamic attraction between them (Kim and Powers, 2004; Reichert and Stark, 2005; Kim et al., 2003; Kim et al., 2004). In the second step, we alternate between the run phase with all flagella rotating anticlockwise and the tumble phase when one or two pre-selected flagella switch to the clockwise rotation through altering the torque direction. The run phase takes about 18.9τ and the tumble phase approximately 12.6τ, so that the duration of each simulation corresponds to approximately 3 tumble events. Note that the time scale τ depends on the applied torque to each flagellum, which is set to $T_m = 300 k_B T$. In most simulations, the pre-selected tumbling flagella are also subject to polymorphic transformation, where the flagellum helicity is changed from left-handed to right-handed. The polymorphic transformation is implemented such that the parameters Ω_n^1 and Ω_n^2 are changed from their original values (representing a left-handed helix) to the same magnitudes with the opposite sign (representing a right-handed helix) in a linear fashion during time 0.76τ. When the tumble phase is over, the tumbling flagella are again subject to anti-clockwise rotation and the reverse polymorphic transformation (from a right-handed to a left-handed helix), leading to the formation of flagella bundle.

To compare simulation results with experimental observations, we assume the body length of $3\mu m$ and the body diameter of $1\mu m$ (Darnton et al., 2007). The period of bundle rotation during *E. coli* run is $\tau = 6.7 \times 10^{-3} s$ with a rotation frequency of 150 Hz (Darnton et al., 2007), which allows us to relate simulation and physical time scales. This means that each simulation corresponds to a duration of $0.76s$, with the run and tumble times of approximately 0.13 s and 0.08 s, respectively. Note that the run time of 0.13 s is shorter than typical *E. coli* run times of about 1 s, which has been selected to reduce computational cost, since we primarily focus on *E. coli* tumbling. However, the time of 0.13 s is long enough to form a tight flagella bundle after a tumbling event. Ambient conditions correspond to a temperature of $T = 20^o$ C with the fluid viscosity of $\eta = 10^{-3} Pa \cdot s$. Table 5.1 compares the properties of simulated and real *E. coli*.

Property	Simulation	Experiment	Reference
Body length (μm)	3.0	2.5 ± 0.6	Darnton et al., 2007
Body width (μm)	1.0	0.9 ± 0.6	Darnton et al., 2007
Flag. contour length (μm)	8.9	8.3 ± 2.0	Lee et al., 2018a
Flag. pitch length (μm)	2.6	2.2	Lee et al., 2018a
Flag. helix radius (μm)	0.2	0.2	Lee et al., 2018a
Flag. bending stiffness (Nm^2)	10^{-22}	$10^{-24} - 10^{-21}$	Hu et al., 2015a
Mean run time (s)	0.13	1.0	Zhang et al., 2023; Korobkova et al., 2004
Mean tumble time (s)	0.08	0.14 ± 0.08	Zhang et al., 2023; Korobkova et al., 2004

TABLE 5.1: *E. coli* parameters used in simulations and measured experimentally with the corresponding references.

5.3 Experimental setup

The lagrangian tracking device used in the experiments comprises of two superimposed stages mounted on an inverted microscope. The horizontal (x, y) position is controlled mechanically, and the $z-$position is adjusted using a piezo-electric mover. A targeted fluorescent particle is visualized within a "trapping area" using

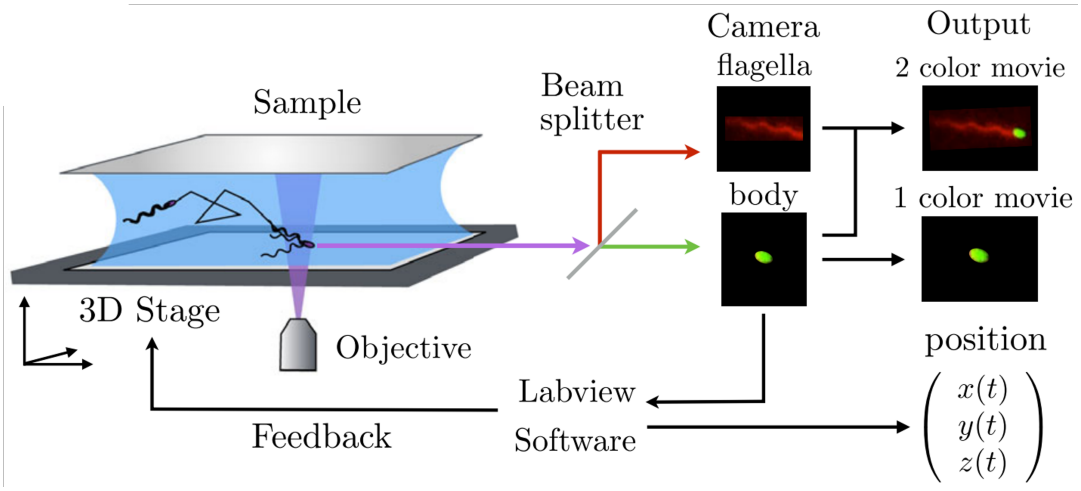

FIGURE 5.2: Schematics of the Lagrangian tracking system, allowing tracking 3D fluorescent objects using one or two color channel. Illustration is adapted with permission from Junot et al., 2022, Physical Review Letters.

a CCD camera. To synchronize image acquisition with stage movements, the stages and camera are triggered by a National Instruments TTL trigger module. The acquired images are transferred to a Labview program, which processes the data. The program records the current x, y, and z positions and directs the mechanical and piezoelectric stages to adjust accordingly, ensuring that the particle remains within the "trapping area" and in focus (Darnige et al., 2017).

Furthermore, two-color fluorescence imaging was conducted using an inverted epifluorescence microscope (Zeiss Observer Z1, equipped with a C-Apochromat $63 \times 1.2W$ objective). To prevent signal overlap and emission leakage, we engineered an *E. coli* strain (AD62) with distinct fluorescence in the body (green) and flagella (red). A dual-color LED light source (Zeiss Colibri 7) and a dichroic image splitter (Hamamatsu) were utilized to project two monochrome images onto separate regions of the camera chip. The microscope stage movement was computer-controlled to maintain the selected bacterium in focus, with images (1024×1024 pixels) captured at 80 frames per second using a Hamamatsu ORCA-Flash 4.0 C11440 camera. The green and red images were subsequently superimposed to generate a movie depicting the tracked bacterium and its flagella bundle. Due to photobleaching, flagella imaging is limited to approximately one minute, but the timing of the second color channel's application can be controlled to visualize flagella dynamics as needed (Junot et al., 2022).

The bacterial suspension is prepared according to the following protocol. Bacteria are inoculated in $10mL$ of Luria Broth (LB) containing ampicillin at a concentration of $100g/mL$ and incubated overnight at $30°C$. Subsequently, 100 µL of this culture is transferred into $10mL$ of Tryptone Broth (TB) and incubated for several hours until the bacteria reach the early stationary phase. The bacterial cells are then harvested by centrifugation, and the supernatant is discarded. The pellet is resuspended in $1mL$ of Berg Motility Buffer (BMB: $6.2mM\ K_2HPO_4$, $3.8mM\ M_2PO_4$, $67mM\ NaCl$, and $0.1mM\ EDTA$) containing $10\mu L$ of Alexa Fluor 647 dye (prepared as a $5mg/mL$ stock solution in DMSO). The suspension is gently shaken for 2 hours. Following incubation, the cells are washed by centrifugation and removal of the supernatant. Finally, the bacterial pellet is resuspended in BMB containing PVP (with

$0.08g/mL$ L-serine) to maintain the activity of bacteria and to inhibit bacterial division.

5.4 Results

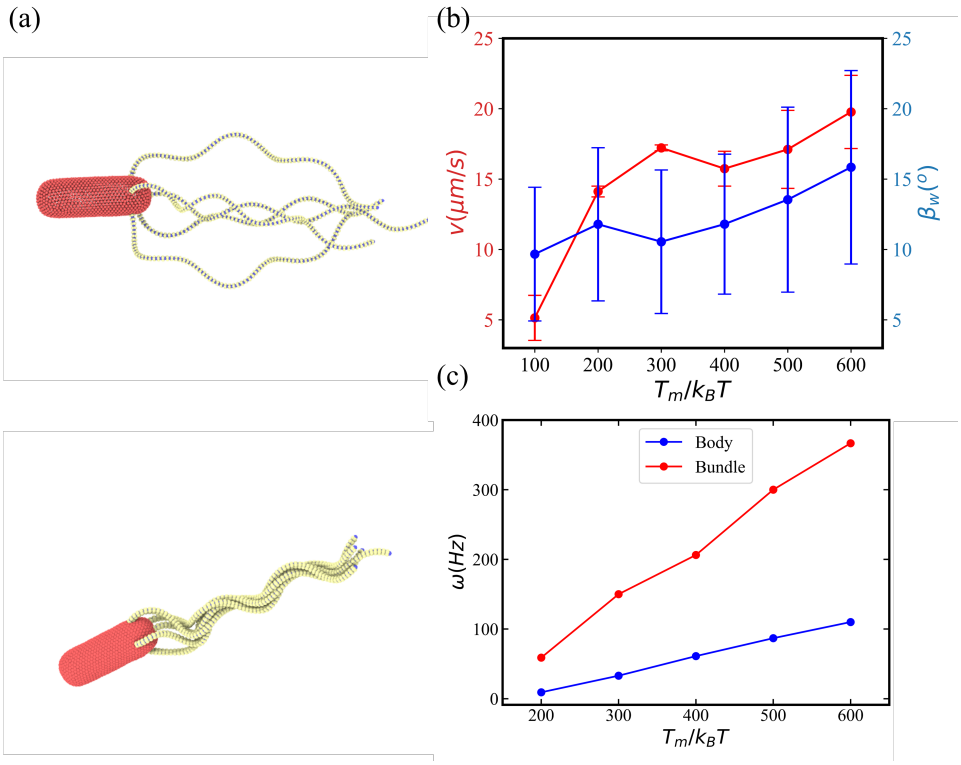

FIGURE 5.3: An *E. coli* model with 5 flagella for different values of torque. (a) Snapshots of *E. coli* for the applied torques $T_m = 100k_BT$ (top) and $T_m = 300k_BT$ (bottom) with a poorly formed and tight flagella bundle, respectively. (b) Average swimming speed v and wobbling angle β_w as a function of applied torque T_m. The swimming speed is computed from a fixed-time displacement and the wobbling angle is defined as the angle between the orientation vector of the body and the axis of flagella bundle during forward swimming (i.e., run phase). (c) The function of rotation frequencies of the body and the bundle with torque.

5.4.1 Run phase

Flagella bundle formation

As seen in the first step of FIGURE5.1, due to the hydrodynamic attraction induced by anticlockwise-rotating left-handed helices, the flagella naturally bundle together (Kim and Powers, 2004; Reichert and Stark, 2005; Kim et al., 2004). In this process, two properties of the *E. Coli* model plays a crucial role here: torque (T_m) and hook strength(K_{hook}), both are in the unit of k_BT. For small torques applied, hydrodynamic interaction forces are relatively weak and the formation of the bundle may not take place. FIGURE 5.3(a) illustrates two snapshots of *E. coli* with $T_m = 300k_BT$ and $T_m = 100k_BT$, where a tight bundle is formed or does not form, respectively. Our

simulation suggests that tight bundle forms when $T_m \gtrsim 200k_BT$. The tightness of the bundle also depends on the bending stiffness of flagella, so that a finite elasticity is necessary of its formation (Kim and Powers, 2004). The strength of hook is also important for the bundle formation, such that stiff enough hooks may prevent the formation of a bundle due to a preferred perpendicular orientation of flagella with respect to the body surface. This is consistent with experimental measurements that the hook is significantly softer than the rest of flagella (Brown et al., 2012; Lee et al., 2018b; Nguyen and Graham, 2018).

Effect of torque

To quantify the run behavior, we measured swimming speed (v) and wobbling angle (β_w) of *E. Coli*. Swimming speed (v) is computed as the displacement per time unit, formulated as:

$$\mathbf{v} = \frac{\mathbf{r}(t_0 + \Delta t) - \mathbf{r}(t_0)}{\Delta t} \tag{5.1}$$

where $\mathbf{v}$ is the average velocity and $v = |\mathbf{v}|$. $\mathbf{r}$ is the position of the model at a particular time. Δt is the time difference. In our measurements of speed, $\Delta t = 22.8\tau$ (0.15 s) and the value is averaged over three measurements. Wobbling, a precession motion of the body axis around the swimming direction. To characteristise this, we define a wobbling angle as the angle between the body long axis and the axis of the bundle. The angle is calculated for each time frame and averaged over a period of body rotation. FIGURE 5.3(b) shows the relationship of swimming speed v and wobbling angle β_w with torque. The increasing trend of swimming speed v with torque T_m is expected since the torque directly relates to the rotation frequencies [see FIGURE 5.3(c)], impacting swimming speed.

If torque is the only quantity affecting the swimming speed, the plot should be fairly linear, contradicting with the results. The non-linear trend can be explained by a decrease in wobbling angle of *E. Coli* with torque shown in FIGURE 5.3(b). A non-wobbling *E. Coli* can have its body swimming in a fashion of a straight line, leading to faster speeds compared to the ones with wobbling. v increases fast from 5 $\mu m/s$ at $T_m = 100k_BT$ to 15 $\mu m/s$ at $T_m = 200k_BT$ because of a tight bundle at the larger torque value. When $T_m > 200k_BT$, the increase in velocity is moderate and near linear as a function of torque. However, the wobbling angle also increases with increasing torque, which is expected to lead to an increased fluid resistance. Due to changes in β_w, an increase in the swimming speed may not necessarily be linear as a function of applied torque.

For the model of *E. Coli* with 5 flgella, we set the value of torque as $300k_BT$, a swimming speed of $17.22\mu m/s$ id reported in FIGURE 5.3, compared to $29 \pm 6\mu m/s$ measured in experiments(Darnton et al., 2007). This difference is firstly due to finite size effect of simulation domains, because the modeled bacterium interacts hydrodynamically with itself through periodic boundary conditions. Extra simulations suggest that the value of swimming speed positively correlates with the size of the simulation box. Secondly, the propulsion strength is reduced because the thickness of simulated flagella is larger than that in experiments, as we cannot resolve the thickness of $20nm$ due to high computational cost in our simulation model. Also, the speed can be tuned up easily by increasing the value of the torque exerted on the flagella, as shown in FIGURE 5.3(b). However, with a different value of torque, the parameters for a successful tumble behavior needs to be re-adjusted. Therefore, to save computational resources, we did not tune the speed of *E. Coli*.

For the rotation frequency ω of body and bundle [FIGURE 5.3(c)], they increase linearly with T_m, suggesting β_w does not significantly affect the rotation frequency of the body. In our simulations, for the model with $T_m = 300k_BT$, the rotation frequency of body is 33 Hz, while 150 Hz for the flagella bundle, agreeing well the experimentally measured values are 23 ± 8 and 131 ± 31 Hz, respectively (Darnton et al., 2007). Therefore, we consider the model of 5 flagella with $T_m = 300k_BT$ as the base model in the following context.

Effect of number of flagella

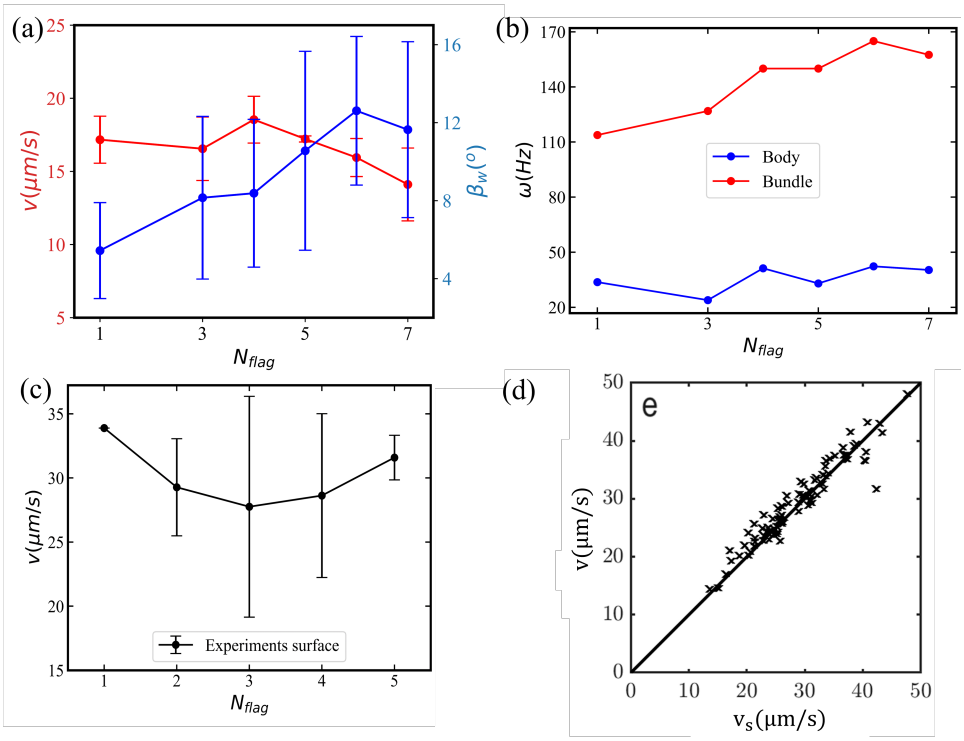

FIGURE 5.4: Plots of dynamical properties of *E. Coli* with a number of flagella, $N_{flag} = 1 - 7$ (except 2) under the same value of torque $T_m = 300k_BT$. (a) The plotting of swimming speed (defined in equation 5.1) and wobbling angle (The angle between the body axis and the bundle axis of *E. Coli* when it swims with the number of flagella. (b) The relationship between the rotation frequency of body and bundle with the number of flagella. In all models, the arrangement of flagella is the same by putting one flagellum along the long axis of the body, with others evenly spreading around on the same circumference of the body surface. (c) Swimming speed of *E. coli* near a surface obtained from experiments. (d) Function of swimming speed near surfaces (v_s) and swimming speed in bulk (v) from experiments.

Experimental observations reported that the number of flagella on *E. Coli* varies (typically around 2 - 7). To test whether the number of flagella affect dynamical characteristics in run stage, we alter the number of the flagella attached on the body from 1 to 7 (except 2). In all models, we keep the arrangement of the flagella the same by putting one flagellum along the long axis of the body, with others evenly spreading around on the same circumference of the body surface. The model of 2 flagella cannot be included, because it cannot satisfy the arrangement as described. Also, the torque is set to be $300k_BT$. FIGURE 5.4(a) shows the measurements of

speed v and wobbling angle β_w with the number of flagella N_{flag}. A possible reason explaining why swimming speed decreases with the number of flagella could be explained by the presence of wobbling, shown in the same FIGURE, *E. Coli* with more flagella has stronger wobbling motion, resulting in a slower speed.

FIGURE 5.4(b) demonstrates the relationship of rotational frequencies of the body and bundle with the number of flagella. The rotational frequency of body is almost independent of number of flagella, while there is a slight increase in the rotational frequency of bundle.

Experimental studies [FIGURE 5.4(d)] have suggested that the swimming speed of wild-type *E. Coli* near surfaces (v_s) and in bulk (v) are almost the same. FIGURE 5.4(c) shows the swimming speed of *E. Coli* near a surface, measured in expriments. The swimming speed near a surface is almost independent of the number of flagella. A simple theoretical argument to support this observation is that the number of flagella only affects the thickness of the formed bundle. Since the propulsion strength would be expected to decrease weakly as a function of the bundle thickness, this effect might be very difficult to reliably measure. Furthermore, it not clear whether the overall output power of *E. coli* increases with the number of flagella or not. In simulations, it is the case since each flagellum is driven by a constant torque of $T_m = 300 k_B T$. Nevertheless, an increased output power with increasing number of flagella has nearly negligible effect on the swimming speed.

5.4.2 Tumble phase

In this section, we will illustrate how different physical properties of *E. Coli* can vary its tumble behavior. We qualitatively compare the tumble behavior of our model with the experiment observations by Turner, Ryu, and Berg, 2000, and then an experimentally-calibrated model will be selected.

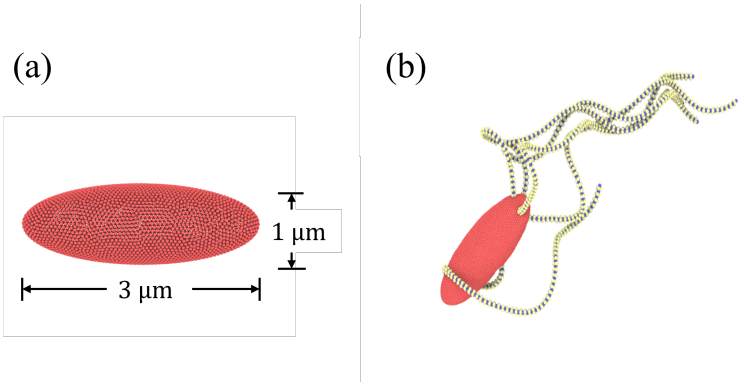

FIGURE 5.5: *E. coli* model with a spheroidal body. (a) Dimensions of the body with a spheroidal shape. (b) Illustrative snapshot of a bacterium during tumbling. Here, $N_{flag} = 5$, $K_{flag} = 2.7 \times 10^5 k_B T b_x$, $K_{hook} = 500 k_B T$, and $T_m = 300 k_B T$.

Body shape: spheroidal v.s. sphero-cylindrical

Initially, we tried a model with the spheroidal body. This body was generated in the same way as described before except that it has a formula of:

$$\left(\frac{x}{b_x}\right)^2 + \left(\frac{y}{b_y}\right)^2 + \left(\frac{z}{b_z}\right)^2 = 1 \tag{5.2}$$

In Sec 5.4.1, we explained that the relative rotation frequency between the flagella bundle and the body of *E. Coli* is purely geometric-dependent. Here, compared to the sphero-cylindrical body shown in FIGURE3.1, the *E. Coli* model with the spheroidal shape has a body rotational frequency of $38Hz$ and a bundle rotational frequency of $75Hz$, because the angles of flagellar attachment is and fluid frictions on the body are different. The ratio between bundle and body rotation frequencies significantly affects bacterium tumbling behavior. The ratio is close to 2 for spheroidal body which is too small compared to 5 from the experiment data (Darnton et al., 2007). Therefore, the body is rotating in a relatively fast speed compared to the bundle due to the small difference in the rotational frequencies of the body and bundle. As seen in FIGURE 5.5, the clockwise rotating flagellum can wrap around the body. To improve this, we changed the body to the shape formulated as equation 3.6.

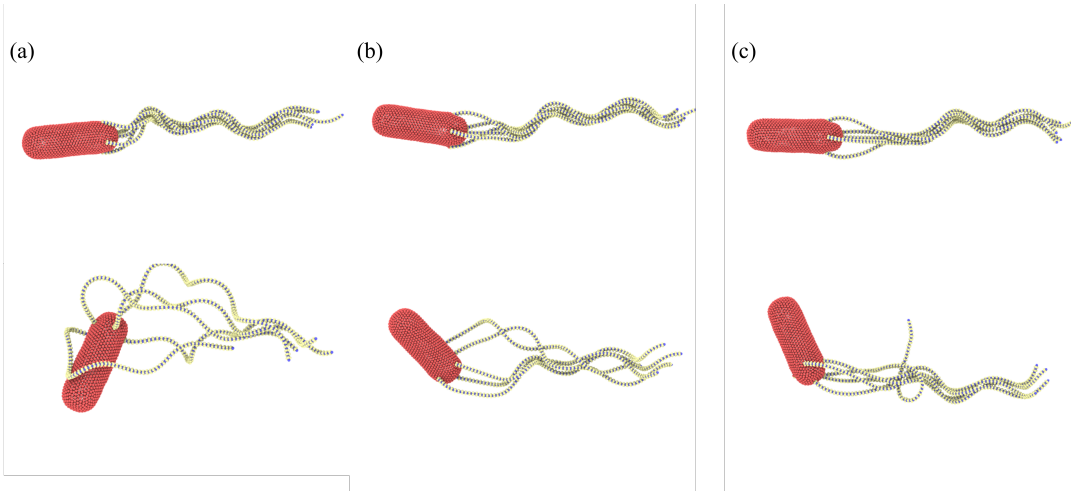

FIGURE 5.6: *E. coli* model with different flagella structure. (a) No linear initial section with full three turns left-handed helices. (b) An initial section of 10 segments (13% of the contour length). (c) An initial section of 20 segements, accounting for 26% of the contour length. The first row of snapshots represent run phase while the second row represents tumble behavior. Here, $N_{flag} = 5$, $K_{flag} = 2.7 \times 10^5 k_B T b_x$, $K_{hook} = 500 k_B T$, and $T_m = 300 k_B T$.

Straight initial section of flagella

Flagellum structure is also important in the process of bundling and unbundling (Kim and Powers, 2004; Reichert and Stark, 2005; Kim et al., 2003; Kim et al., 2004). Here, we tested the effect of a straight section of flagella (no helicity) near the body-attaching point. FIGURE 5.6 compares the run and tumble phases of *E. coli* models with a varying length (from 0% to about 26% of the contour length) of the linear flagellum section. We can observe that the linear sections of flagella help flagella stay bundled together while the pre-selected flagellum tries to flip out during tumbling. On the other hand, the clockwise rotating flagellum could not easily leave the bundle, when the initial straight section has a length of $10 - 20$ segments ($13 - 26\%$ of the contour length). The results suggest that the tumbling flagellum could leave the bundle more easily when there is a large differences between the tumbling flagellum and the bundle. For the flagella without an initial straight section, during tumbling, the clockwise-rotating flagellum has rotation through the whole flagellum, facilitating its leaving from the counterclockwise-rotating bundle.

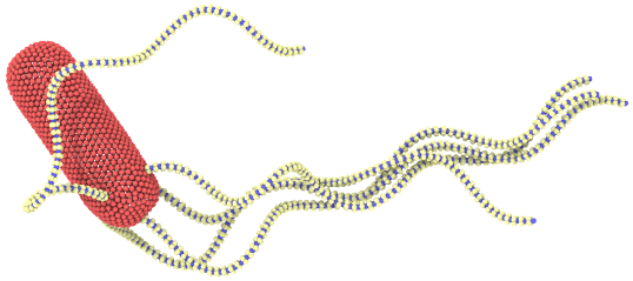

FIGURE 5.7: The tumble behavior of the *E. Coli* model with polymorphic transformation of the flagellum. At the begining and the end of a tumble process, the tumbling flagellum changes its rotating direction while changes its handedness (the change of handedness is called polymorphic transformation). Here, $N_{flag} = 5$, $K_{flag} = 2.7 \times 10^5 k_B T b_x$, $K_{hook} = 200 k_B T$, and $T_m = 300 k_B T$.

Polymorphic transformation

Several literature have reported the phenomenon that the flagella of a wild-type *E. Coli* undergo the polymorphic transformation when it tumbles (Darnton et al., 2007; Turner, Ryu, and Berg, 2000; Berg, 2004). As mentioned in the Introduction, while one or two flagella start to rotate clockwise in the beginning of a tumble, the helicity of the tumbling flagellum changes from the normal state (left-handed) to the state with right-handed helicity and finally back to the normal state at the end of the event. In our model, we implemented the transformation by changing the original values of Ω_n^1 and Ω_n^2 to the oppositely signed values during a time of 0.76τ.

Comparing FIGURE 5.7 and FIGURE 5.6(a) at bottom (without polymorphic transformation, we can observe that the polymorphic transformation can help the tumbling flagellum quickly leave the bundle and, thus does not interrupt the tightness of the bundle. The reasons why polymorphic transformation facilitates the escaping of a tumbling flagellum are following: A clockwise rotating flagellum that leaves the bundle without polymorphic transformation exerts a propulsion force in the opposite-to-swimming direction, which competes with the propulsion force of the bundle. Since the propulsion forces from a single flagellum and a flagella bundle are comparable (supported by nearly independence of the swimming speed of *E. coli* on the number of flagella in FIGURE 5.4), their counter-action in case of no polymorphic transformation of the tumbling flagellum leads to a significant slow-down of the bacterium, and thus, a partial disappearance of the bundle. However, in the case of polymorphic transformation, propulsion forces from the tumbling flagellum and the bundle act in a similar direction, so that the bacterium does not significantly lose its speed, maintaining a tight confirmation of the bundle. Furthermore, we find that the tumbling flagellum with polymorphic transformation hydrodynamically repels the counter-rotating bundle, further facilitating its efficient escape from the bundle.

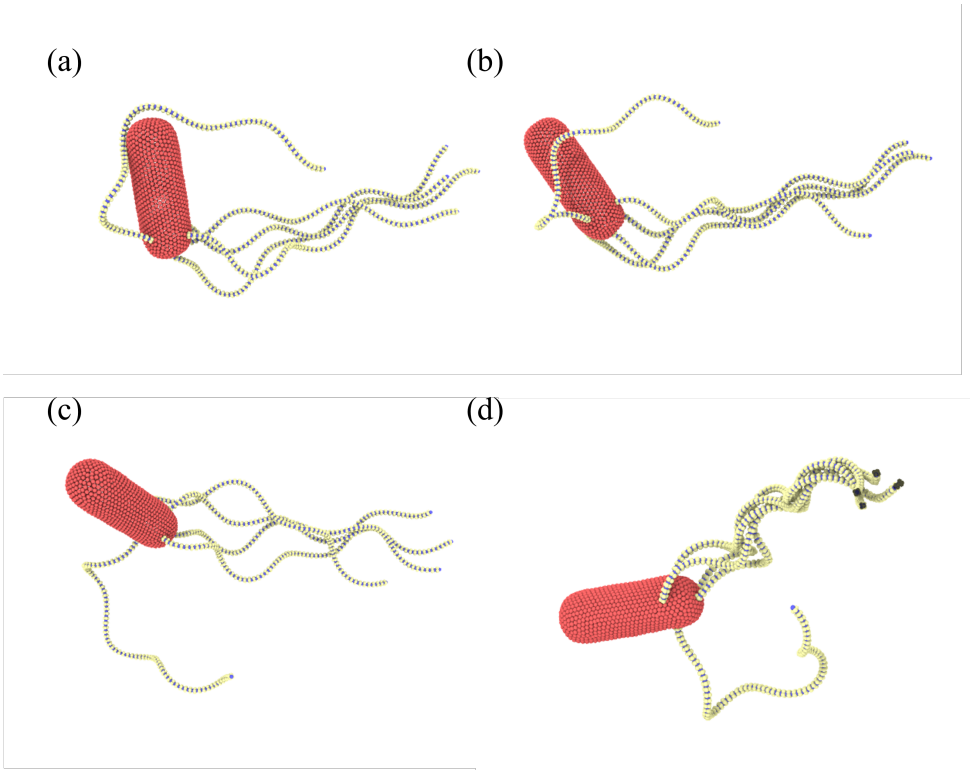

FIGURE 5.8: The tumble behavior of the models with different set of hook strength K_{hook}. (a) all flagella have a hook strength of $K_{hook} = 100k_BT$. (b) all flagella have a hook strength of $K_{hook} = 200k_BT$. (c) all flagella have a hook strength of $K_{hook} = 500k_BT$. (d) The model with adaptive hook strength. The pre-selected flagellum (the flagellum that rotates clockwise during a tumble event) has a hook strength of $500k_BT$ and other flagella $100k_BT$. In all cases, polymorphic transformation of the per-selected flagellum is implemented. Here, $N_{flag} = 5$, $K_{flag} = 2.7 \times 10^5 k_BTb_x$, and $T_m = 300k_BT$.

Hook stiffening

FIGURE 5.8 shows the tumble results of the models with different combinations of hook strength. FIGURE5.8 (a-c) presents the tumbling results of the models without hook stiffening. We can observe that during tumble, the higher the hook strength is, the easier the tumbling flagellum leaves the bundle and the looser the bundle formed by other flagella is. Some literature (Zhang et al., 2023; Nord et al., 2022) suggests that the hook of a tumbling flagellum could get stiffened during the tumbling process. This is because the hook must be stiff enough so that the filament can come out from the bundle and point to other directions while the hook must be compliant enough to form a coherent bundle during the run stage (Zhang et al., 2023). To achieve this, We therefore combine the cases shown in (a) $K_{hook} = 100k_BT$ and (c) $K_{hook} = 500k_BT$ into (d) where the 'hook stiffening' is applied. In (d), the K_{hook} of the per-selected flagellum is $500k_BT$ while others $100k_BT$. By doing this, the tumbling flagellum can easily leave the bundle and the bundle can remain tight.

The reasons that we do this are: 1) The high hook strength of the tumbling flagellum makes the first a few contour particles of flagellum stay at 90° with the surface of the body around the attaching point (equation 3.3). When the flagellum rotates clockwise, its rotation pulls the flagellum out of the bundle, which can be imagined through a rotating cable with torsional and bending rigidity. Also, the hook rigidity

drives the tumbling flagellum toward a perpendicular-to-the-body orientation that is favorable for a proper tumbling. However, hook stiffness can also be not too large, as it would then may prevent the formation of a tight bundle. 2) As other flagella have small K_{hook}, they can easily bend towards the flagella attaching points on the body surface. Therefore, the soft hook of the flagella and the attractive hydrodynamic interactions (left-handed helices rotating anti-clockwise) help the formation of a coherent bundle.

FIGURE 5.8(d) shows a tumbling behavior of a *E. Coli* with a coherent bundle and a good separation of the tumbing flagella to the bundle. Therefore, hook stiffening of the tumbling flagella helps a *E. Coli* tumbling.

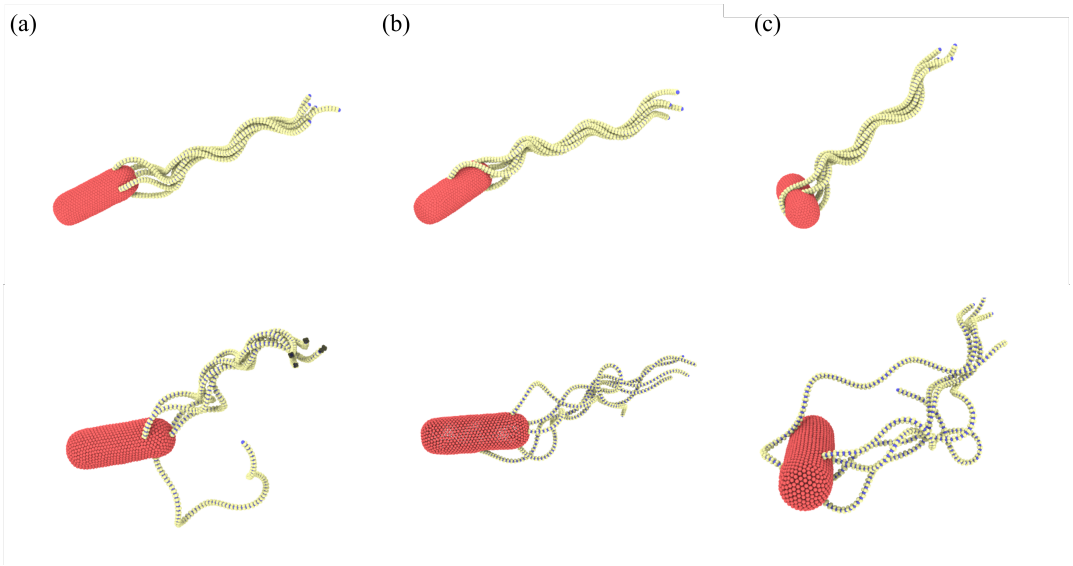

FIGURE 5.9: *E. Coli* models with different arrangements of flagella. The total number of flagella is $N_{flag} = 5$ for all three examples. (a) The *E. Coli* model with a symmetrical arrangement of flagella. 1 flagellum is attached along the long axis of the body, the other 4 symmetrically distributed around the body, separated by 90°. (b) The attaching point of the flagella on the body are randomly distributed on the second half of the body. (c) The attaching point of the flagella are randomly distributed on the whole body. The first row shows the run behavior and the second shows the tumble behavior. In all three models, $K_{flag} = 2.7 \times 10^5 k_B T b_x$, $T_m = 300 k_B T$, and the hook rigidity of the tumbling flagellum is $500 k_B T$ with polymorphic transformation, and the others with $K_{hook} = 100 k_B T$.

Flagella arrangement

Due to the peritrichous nature of *E. Coli* (Zhang et al., 2023), we also investigated different arrangements of flagellar attachment on the body. FIGURE 5.9 show three different arrangement of flagella. In each case, the number of the flagella is 5. The symmetric placement of flagella we used so far [see FIGURE 5.9(a)] leads to a persistent run dynamics of the bacterium with a moderate wobbling of the body, as shown in FIGURE 5.3(b). The symmetric model exhibits tumbling that compares well with experimental observations. A model with flagella randomly attached within the rear half of the body in FIGURE 5.9(b) exhibits a comparable run phase, but does not always reproduce successful tumbling, as the tumbling flagellum does not always leave the bundle quickly enough. Finally, a random distribution of flagella

attachment points on the whole body results in a strong wobbling of the body [see FIGURE 5.9(c)] with a reduction in the swimming speed. For this model, the tumble phase is also not well controlled, such that the change in the swimming direction ranges from small to large angles. As a result, it is difficult to generalize the run and tumble behavior of *E. coli*, when flagella are randomly distributed over the whole body. Interestingly, experimental observations indicate that all types of flagella arrangements are possible, though the majority of bacteria have them often clustered near one end of the body.

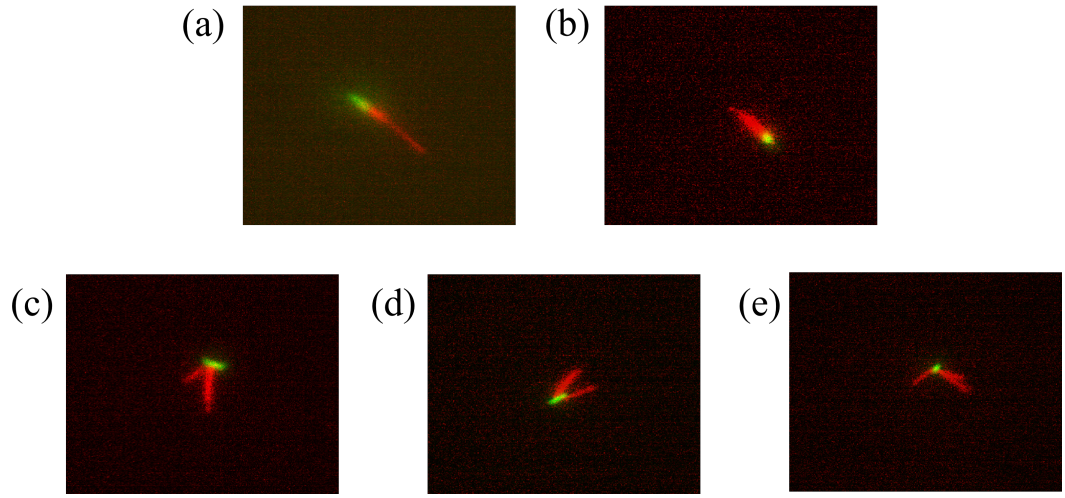

FIGURE 5.10: Several experimental snapshots of *E. coli* strain AD62 with a mutation allowing to express a green fluorescent protein (GFP) on its body and to use Alexa 647 (red color) for its flagella. (a) & (b) Snapshots of *E. coli* during run phase, which compare well to the simulation snapshots in FIGURE 5.9. (c) - (e) Snapshots of *E. coli* during tumble phase, which can be compared to those in FIGURE 5.9 and 5.11.

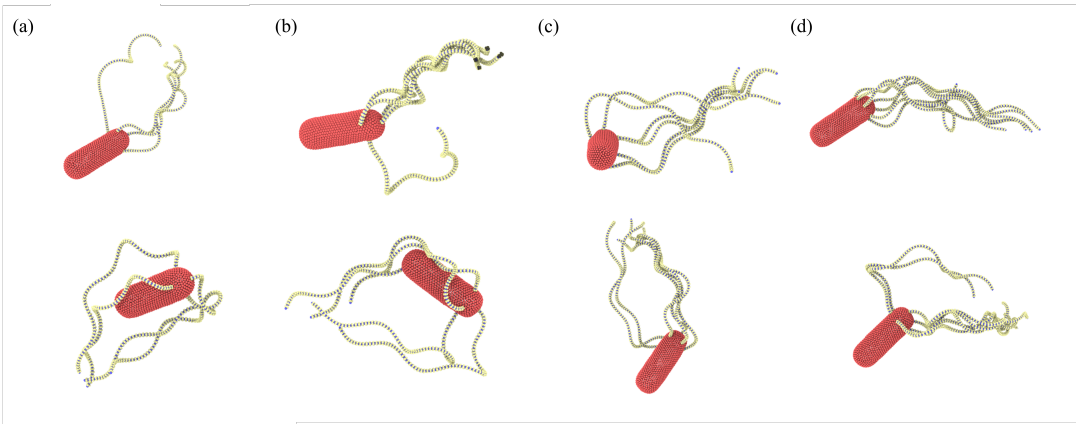

FIGURE 5.11: Models of different number of flagella. (a) $N_flag = 4$, (b) $N_flag = 5$, (c) $N_flag = 6$ (d) $N_flag = 7$. The first row shows the case where only one tumbling flagellum and the second row presents the tumble behavior of the models with two tumbling flagellum.

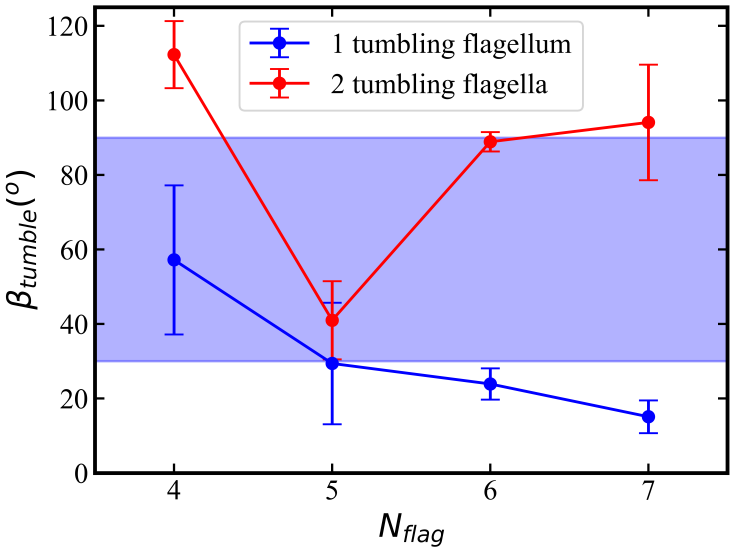

FIGURE 5.12: Function of tumble angle (β_{tumble}) of the *E. Coli* model with numbers of flagella (see snapshots in FIGURE 5.11). The blue and read lines indicate the case of 1 or 2 tumbling flagellum/flagella. The blue shade indicates the range of tumble angle measured experimentally (Darnton et al., 2007). The tumble angle β_{tumble} is defined as the angle between the orientation vector of the body of a bundled *E. Coli* in the beginning and at the end of a tumble event.

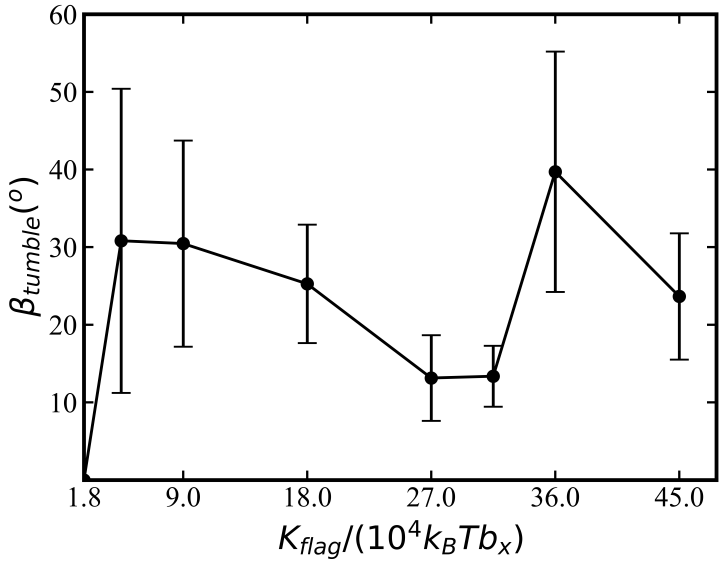

FIGURE 5.13: Function of tumble angle β_{tumble} with different bending stiffness of flagella K_{flag}. Only the cases where one tumbling flagellum are included. $N_{flag} = 5$. The tumble angle is defined as the angle between the orientation vector of the body of a bundled *E. Coli* in the beginning and at the end of a tumble event. Each data point is averaged over three tumble events.

5.4.3 Comparisons to experiments

Our simulation show that the model with the implemented features of rounded-cylindrical body, full-helix flagella, polymorphic transformation, hook stiffening and

symmetrical arrangement of the flagella can successfully mimic the tumble behavior of wild-type *E. Coli in vitro*, shown in Turner, Ryu, and Berg, 2000. FIGURE 5.10 shows several snapshots from experiments (the experiments setup is shown in FIGURE 5.2), which resemble well the simulation snapshots in FIGURE 5.9 and 5.11, since most of the snapshots show two branches of flagella while tumbling. Despite the fact that we often used a symmetric placement of flagella at the body in simulations, random distribution of flagella attachment points can easily be adopted to reproduce the variety of *E. coli* tumbling dynamics in experiments. However, it is difficult to systematically characterize the tumbling behavior for various flagella arrangements.

Available experimental observations also show that two flagella may be involved in the tumble phase instead of a single one, though it occurs less often. FIGURE 5.11 compares snapshots of tumbling *E. coli* models with one (the top row) and two (the bottom row) tumbling flagella for different N_{flag}. Even though the tumbling behavior is qualitatively similar for the cases with one and two tumbling flagella, we can also observe some differences. The major difference is that changes in the body and bundle orientations are more pronounced when two tumbling flagella are activated in comparison to a single one. This is not entirely surprising, since two tumbling flagella exert larger torques on the body, enhancing dynamic changes in its orientation.

In FIGURE 5.12, the relationship of the tumble angle with the number of flagella is plotted and compared to experimentally measured range by Darnton et al., 2007. We define the tumble angle as the angle between the orientation vector of the body (see FIGURE 3.1(a)) of a bundled *E. Coli* before and after a tumble event. FIGURE 5.12 shows a decreasing trend of β_{tumble} with N_{flag} when there is only one tumbling flagellum. As N_{flag} increases, it becomes more difficult for the tumbling flagellum to leave the bundle [see Fig. 5.11(d)]. Furthermore, a bundle with more flagella better controls the direction of the body, allowing smaller changes in its orientation. As shown in FIGURE 5.12, the *E. coli* model with two tumbling flagella exhibits larger tumble angles than that with one tumbling flagellum. However, in this case β_{tumble} behaves non-monotonically as a function of N_{flag}. Note that most of the tumble angles in simulations lie within the range of $30^\circ - 90^\circ$ experimentally observed values (Turner, Ryu, and Berg, 2000; Darnton et al., 2007; Berg and Brown, 1972; Taute et al., 2015), which is indicated by the blue shaded area in FIGURE 5.12.

Since experimental measurements of flagella bending rigidity yields a rather wide range of $10^{-24} - 10^{-21} Nm^2$ (Hu et al., 2015a), we have also considered the possible effect of K_{flag} on the tumble angle β_{tumble}, shown in FIGURE 5.13. Simulations indicate that *E. coli* with $K_{flag} = 1.8 \times 10^4 k_B T b_x$ does not exhibit a significant tumble behavior with $\beta_{tumble} \approx 0$. Then, β_{tumble} first decreases starting from relatively soft flagella with $K_{flag} = 4.5 \times 10^4 k_B T b_x$ and to $K_{flag} = 2.7 \times 10^5\ k_B T b_x$. For even larger K_{flag}, an increase in β_{tumble} is observed. Note that in the limit of rigid flagella, no bundle formation due to hydrodynamic interactions would be possible (Kim and Powers, 2004).

5.5 Discussion and conclusions

In this work, our main goal was to develop a realistic and flexible *E. coli* model and to address the question: which physical properties of *E. coli* govern its run-and-tumble behavior. We have identified a few parameters which strongly affect *E. coli* swimming behavior, including the shape of the body and flagella, polymorphic

transformation of flagella, dynamic hook stiffening, and the arrangement of flagella on the body. It is a proper combination of these characteristics that makes *E. coli* an excellent swimmer which can efficiently explore the surrounding environment.

We illustrate the importance of the ratio between the rotational frequencies of the body and the flagellar bundle in section 5.4.2. In experiments, the ratio is close to $1/5$ of wild-type *E. Coli* (Turner, Ryu, and Berg, 2000). The spheroidal shape of the body we proposed first has a ratio of the body and bundle rotation frequency of $1/2$. As a result, tumbling flagella that leave the bundle may wrap around the body due to its fast rotation, significantly limiting the ability of a bacterium to change direction. Therefore, for the sphere-cylindrical body, the ratio of $1/5$ between the body and bundle rotation frequencies is small enough so that the fast rotation of the bundle for a fast swimming speed does not automatically impose a fast rotation of the body, which would be problematic for the tumbling phase. Also, as demonstrated in FIGURE 5.3, torque is another important factor in achieving the right ratio of rotational frequencies of the body and the flagellar bundle. More than that, if torque is too small, ($T_m \lesssim 200 k_B T$), the flagellar bundles formed are not tight due to weak hydrodynamic interactions, resulting in a poor propulsion ability of *E. coli*. Therefore, an efficient tumble behavior relies on the geometric characteristic of the body and flagella, the magnitude of the applied torque of the actuating motors.

Section 5.4.2 demonstrates another important physical aspect – "polymorphic transformation" of the tumbling flagella. When tumbling starts, the tumbling flagella changes its helicity from left-handed to right-handed while rotating clockwise. The hydrodynamic field of a right-handed helix rotating clockwise helps the tumbling flagella propel in a direction close to the swimming direction so they can pull out quickly and does not disturb the bundle formed by other counterclockwise rotating flagella, presented in FIGURE 5.7. Also, the different helicity and rotating direction of the tumbling flagella and the other enable a repulsive flow field, further facilitating the tumbling flagella's escape from the bundle.

Another important aspect for an efficient tumbling behavior of *E. Coli* is the bending stiffness of the hook. The hook must be soft enough to aid flagella in bending towards the base to form a bundle during the run stage, while it must be stiff enough to let the tumbling flagella move away from the bundle during tumbling. The experimental work suggested by Zhang *et al.* (Zhang et al., 2023) provides evidence that the bending stiffness of the hook is higher when flagella rotate clockwise compared to anti-clockwise rotation. This idea was implemented in the model, and we have shown that the tumbling flagella can pull out more efficiently with a stiff hook while other flagella stay in a tight bundle during tumbling due to soft hooks (FIGURE 5.8). Furthermore, the preference for a perpendicular orientation of flagella with respect to the body surface due to the hook bending stiffness affects its dynamics. Let us imagine a cable with torsional rigidity mounted perpendicular to a surface and bent along the surface. Rotation of this cable at the base would result first in pulling it along the surface due to torsional resistance until it bends enough near the base to allow the full rotation at the base. Note that if the mounting angle of the cable is not restricted (i.e., flexible attachment), the cable base would be aligned with the surface, and its rotation at the base would simply lead to the rotation of the whole cable without any pulling effect. Similarly, tumbling flagella attached to the cylindrical side of the body are first pulled out of the bundle if the hook is not too soft, facilitating their escape from the bundle. Thus, these two effects (hook stiffening and initial pulling of tumbling flagella) provided by the bending stiffness of the hook aid in the successful escape of the tumbling flagella from the bundle.

In Section 5.4.2, we discussed the tumbling behavior of different arrangements of

flagella. FIGURE 5.9(c) presents the tumbling behavior of *E. Coli* when the flagellar location on the body is randomized, leading to a very large wobbling angle when it swims. This large wobbling angle complicates the tumbling. Also, through our project, we found it very hard to systematically study the effect of different flagellar arrangements, as there are infinite possibilities, and we only have limited computational resources. Therefore, even though experimental studies suggest a peritrichous nature of *E. Coli*, we report a base model with $N_{flag} = 5$ symmetrically placed flagella at one of the body ends for simplicity. Furthermore, the behavior of *E. coli* should be considered statistically since each tumbling event is different, even for the base model with symmetrically placed flagella. For instance, a few tumbling attempts are not even successful, as the tumbling flagellum was not able to leave the bundle, see FIGURE 5.11(d).

This model has the potential to address some questions of *E. Coli* behavior in complex environments, where experimental observations may not be detailed enough to propose corresponding physical mechanisms. For example, a recent experimental study by Junot et al., 2022 suggests that tumbling is the dominant escape mechanism for wild-type *E. Coli* to leave a non-slip wall. However, the underlying physical mechanism is still unclear. Also, another interesting phenomenon of *E. Coli* swimming near surfaces in a circular fashion still needs to be further investigated by the scientific community.

Chapter 6

Hydrodynamics of Surface Escape by Tumbling *E. Coli*

As mentioned in section 2.3.4, "wall entrapment" has been observed for *E. Coli*-like swimmers. However, the origin of this phenomenon is unclear. Some researchers think it is from a statistical effect of steric interactions, while others propose that it is purely hydrodynamics-induced. Another relevant question is how *E. Coli*-like bacteria escape from surfaces, which raises interest in the scientific community. From the biological perspective, the exploration of space for nutrition is essential for bacterial survival, and their survival chance is minimized if they can only stay near surfaces. Various theories have been proposed, as discussed in section 2.3.4. Our work is based on the analysis and conclusion made in Junot et al., 2022 who proposed that tumbling is the dominant escape mechanism. Based on this assumption, in this chapter, we study how *E. Coli* uses tumbling as the primary mechanism to escape. We performed simulations using the *E. Coli* model described in chapter 5 confined between two non-slip walls. Similar to Junot et al., 2022, the same definition of the surface region is employed as the distance from the body centroid of the *E. Coli* to the wall smaller than $3\mu m$. Similar analysis was performed for comparison, and we conclude that the orientation of a *E. Coli* after tumbling affects the escaping rate. The chapter is structured as follows. Section 6.1 includes all necessary details about the methods and models employed. In Results (section 6.2), three analyses are performed, including the distribution of escape angle (section 6.2.1), distribution of number of tumbles required to escape (section 6.2.2), and distribution of unbundling disoriented pitch angle (section 6.2.3). The main results are discussed in section 6.3 with a conclusion.

6.1 Methods and models

The model of *E. Coli* has been detailed in section 3.3. As shown in FIGURE 6.1, the bacterium model is confined between two non-slip walls in h direction, with periodic boundary conditions applied along the other two directions perpendicular to h. Fluid flow is modeled by the dissipative particle dynamics (DPD) method, detailed in section 3.4.1. The implementation of the non-slip boundary conditions is discussed in section 3.4.2.

6.1.1 Simulation setup and parameters

The length scale (b_x) and the time scale (τ) are defined in the same way as in section 5.2 with $b_x = 9$ and $\tau = 132$ in simulation units, and $b_x = 1.5\mu m$ and $\tau = 1/150s$ in real units. The simulation box is a domain of dimensions $L_x \times H \times L_z$, where

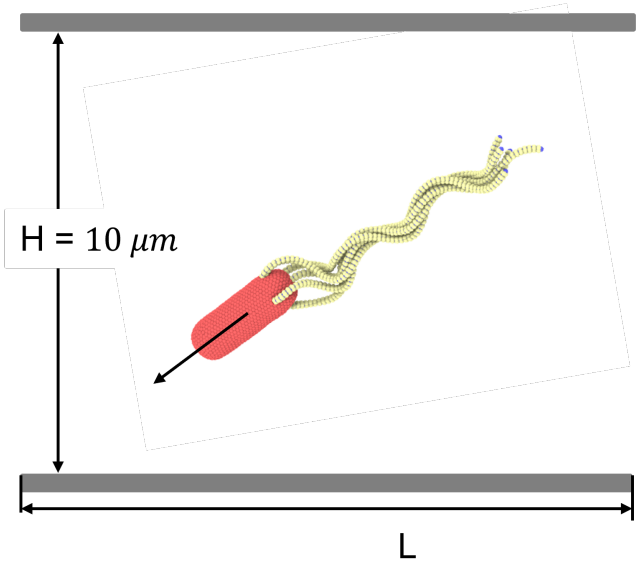

FIGURE 6.1: The model of *E. Coli* confined in a slit. The details of the *E. Coli* model are given in section 3.3.

$L_x = 10.56b_x = 15.8\mu m$, $H = 6.67b_x = 10\mu m$ and $L_z = 11.56b_x = 17.3\mu m$, as shown in FIGURE 6.1. In total, there are around 1.84×10^6 fluid particles in the system, resulting in a number density of $n_d = 2.26 \times 10^3 b_x^{-3} = 672.31\mu m^{-3}$. DPD parameters for the interactions between fluid particles and between fluid particles and wall particles are $a = 540k_BT/b_x$, $\gamma = 225\sqrt{mk_BT}/b_x$ ($m = 1$ and $k_BT = 1$), $s = 0.15$ and $rc = 0.11b_x$. Frictions between the *E. Coli* and fluid particles or wall particles is simulated by DPD interactions with the parameters of $a = 0$, $\gamma = 360\sqrt{mk_BT}/b_x$, $s = 0.1$ and $r_c = 0.09b_x$. These yield a fluid dynamic viscosity of $\eta = 1230\sqrt{mk_BT}/b_x^2$, corresponding to a viscosity of $10^{-3} Pa \cdot s$. The time step Δt of integration is $2.27 \times 10^{-5}\tau$.

The model of *E. Coli* has been described in 3.3 and chapter 5. In summary, we use the model illustrated in FIGURE 5.8(d) where $N_{flag} = 5$, $K_{flag} = 2.7 \times 10^5 k_BTb_x$ (corresponding to $8.5 \times 10^{-23} Nm^2$), $T_m = 300k_BT$, $K_{hook} = 100k_BT$ for non-tumbling flagella, and $K_{hook} = 500k_BT$ for the tumbling flagellum. Note that we consider a symmetrical arrangement of flagella with one of the flagella attached to the body end and others symmetrically around the body. Also, there is only one tumbling flagellum, which undergoes a polymorphic transformation during tumbling.

Finally, the excluded-volume interactions implemented through the Lennard-Jones potential with $\epsilon_{LJ} = k_BT$ and $\sigma_{LJ} = 0.06b_x$.

The simulations are carried out in four steps. In the first step, as mentioned in chapter 5, with a counter-clockwise torque acting on all flagella, they bundle under hydrodynamic interactions. Then, this bundled configuration is placed in the confined system with the orientation vector pointing to one of the walls. We run the simulation so that the *E. Coli* swims toward the wall, then interacts with it, and finally swims parallel to the wall. In the third step, we allow the *E. Coli* to swim on the wall for around $227.27\tau = 1.52s$. The *E. Coli* configurations are saved every $22.73\tau = 0.15s$, and each serves as the initial configuration for the next step. In the last step, we activate the tumbling motion in our model. The duration of run and tumble is set to be exponentially distributed (Block, Segall, and Berg, 1983; Berg and Brown, 1972; Berg, 2004; Saragosti et al., 2011; Alon et al., 1997; Alon et al., 1998). The exponential distribution for run time has a mean of $30.30\tau = 0.20s$ and ranges from

28.79τ to 31.82τ (from 0.19s to 0.21s), while the distribution of tumble time averages at 13.39τ (0.09s) and ranges from 6.82τ (0.05s) to 18.94τ (0.13s). The range of the run time corresponds to a period of body rotation, and the mean is smaller compared to the experimentally reported value of 1s. The range of tumble times follows the range of tumble time reported by Turner, Ryu, and Berg, 2000. The details of how a tumble is modeled are given in section 5.2.

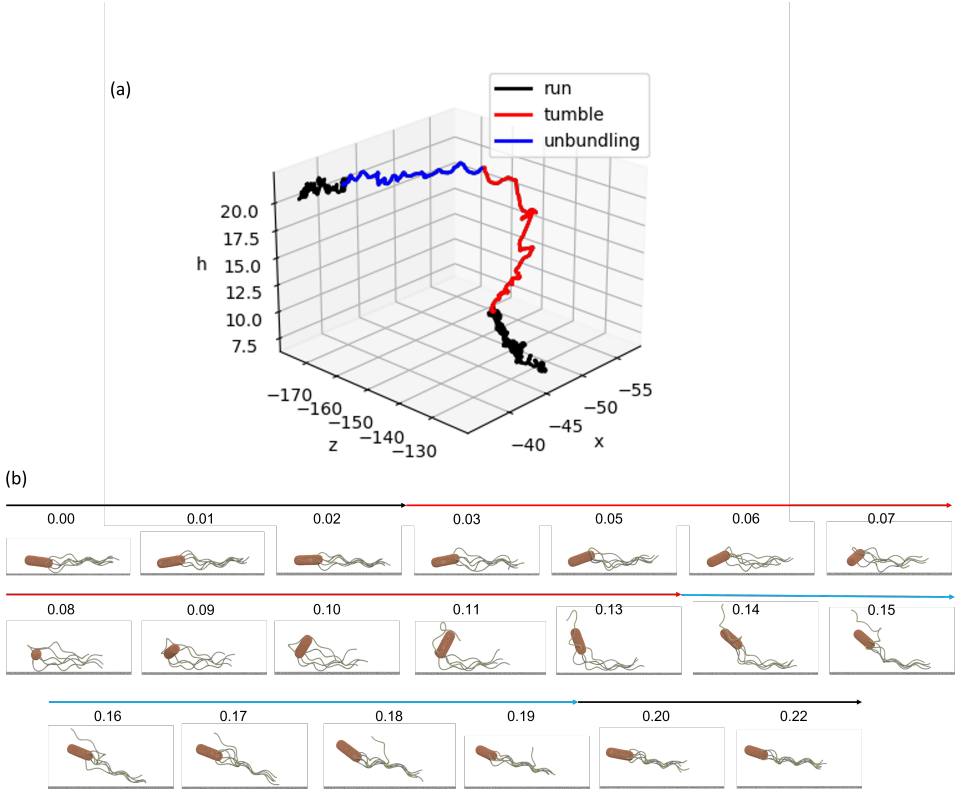

FIGURE 6.2: Trajectory (a) and snapshots (b) of a *E. coli* escaping from the wall. (a) 3D trajectory of *E. Coli* swimming near the surface and then escape after a tumble. Three phases are labelled: run(black), unbundling disoriented (red) and unbundling oriented (blue). Unbundling disoriented phase defines the period when the orientation of the body changes erratically, corresponding to the time from the start of the first polymorphic transformation to the end of the second one in a run-and-tumble cycle. Unbundling oriented phase is the regime where the *E. Coli* changes its orientation only slightly while being unbundled. (b) Time lapse of an escape event. The color of the lines corresponds to different phases as shown in (a). The total duration is 0.24s.

6.2 Results

We consider a "successful escape" when the distance from the body centroid of an *E. Coli* to the wall is larger or equal to 3μm, similarly as defined in Junot et al., 2022. Also, we define the tumble righty before the successful escape as a "successful tumble." We collected 38 instances of successful escapes. The trajectory and snapshots of a successful escape are shown in FIGURE 6.2. There are roughly three phases: run, disoriented unbundling, and oriented unbundling. *E. Coli* moves nearly on a

straight line during the run phase. From simulation videos, we observe that sometimes there is a period when the *E. Coli* is still unbundled but with little change in orientation, in contrast to the erratic motion of *E. Coli* in the disoriented unbundling regime. We further observed that the duration of the disoriented unbundling phase coincides with the time from the start of the first polymorphic transformation to the end of the second one in a run-and-tumble cycle (FIGURE 1.3). We hypothesize that the direction of the body orientation vector at the end of the unbundling disoriented phase is crucial for a successful escape. Note that the moment of the end of the unbundling disoriented phase is defined by the end of the polymorphic transformation directly before a run phase. For simplicity, we abbreviate the moment as t_{ept}. we will first validate our model by computing two distributions presented in Junot et al., 2022. These are the distribution of escape angle and the distribution of the number of tumbles required to escape. Then, the distribution of the pitch angle at t_{ept} is analyzed, propose a mechanism for *E. Coli* to use tumbling to escape.

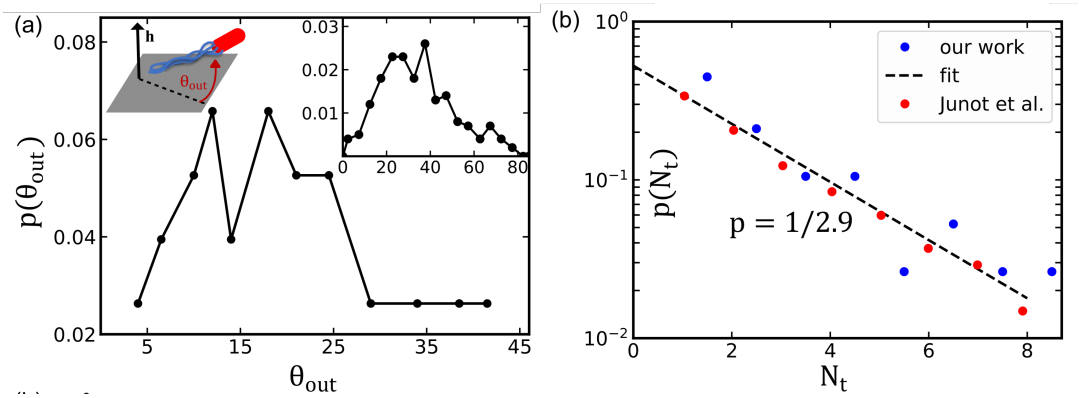

FIGURE 6.3: (a) Probability distribution $p(\theta_{out})$ of escape angles. The inset on the left shows the definition of escape angle θ_{out}, and the inset on the right shows the experimental results from Junot et al., 2022. (b) Distribution of a number of tumbles required to escape. Junot et al., 2022 employed the "BV model" to simulate the motility statistics of *E. Coli*, the parameters for the model are taken from Figueroa-Morales et al., 2020. The black dotted line is proportional to $p(N_t) = (1 - p)^{N_t - 1} p$, with $p = 1/2.9$.

6.2.1 Distribution of escape angles

FIGURE 6.3(a) shows the probability distributions of escape angles from our work and from Junot et al., 2022. $p(\theta_{out})$ is small in the range of $\theta_{out} < 10°$, because when an *E. Coli* moves with a small grazing angle ($\theta_{out} \to 0$), it takes a long time to move away from the during which there is a high chance of having another tumble *en route* (Junot et al., 2022). This tumble event would either lead to a failed escape or an escape with a higher escape angle. The peak centering between 10° and 20° is likely due to the surface hindrance effect for a large-angle tumble, as reported in Molaei et al., 2014; Junot et al., 2022. Comparison of the distributions from our work and Junot et al., 2022 shows reasonable agreement, through the peak in experiments is at larger value, centering around $20° - 40°$, as shown in the inset on the right. This difference might be due to a limited data size and a different setup in comparison the experiments carried out by Junot et al., 2022.

6.2.2 Distribution of number of tumbles required to escape

The distribution of the number of tumbles required for a bacterium to escape is plotted in FIGURE 6.3(b). We count the number of tumbles that a *E. Coli* performs before a successful escape. The work by Junot et al., 2022 employed the "BV" model to simulate the escaping statistics, and the results are shown as red dots, while the data from our work are shown in blue. Both our work and Junot et al., 2022 demonstrate the same trend fitted by a binomial function of $p(N_t) = (1-p)^{N_t-1}p$, with $p = 1/2.9$. However, blue data points are more scattered around the fit, probably because of a limited data amount. $p \approx 1/3$ is counter-intuitive because we would expect that a tumble should lead to a successful escape as long as the post-tumbling orientation of the body is pointing towards the bulk, resulting in $p = 1/2$. $p \approx 1/3$ means that there is a minimum post-tumbling angle for escape to happen.

6.2.3 Distribution of unbundling disoriented pitch angles

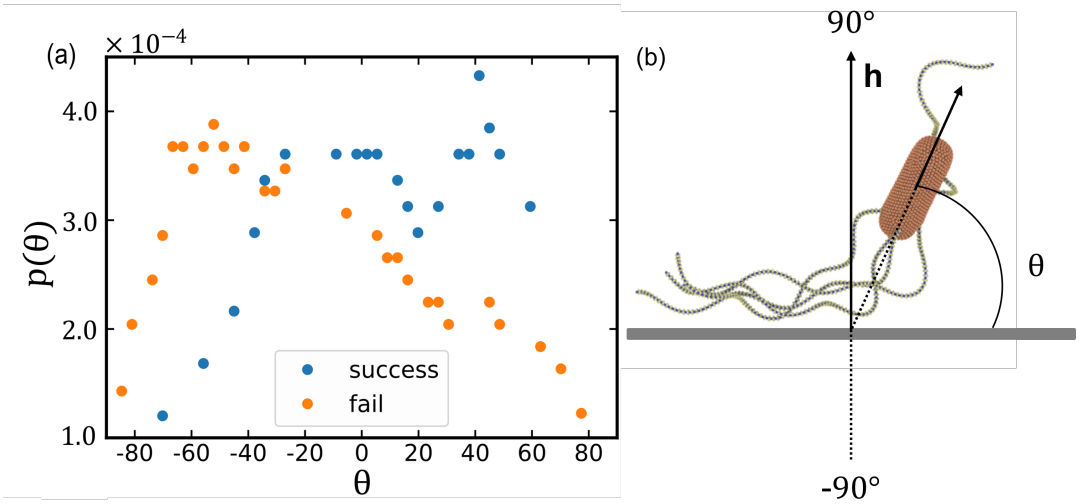

FIGURE 6.4: (a) Distribution of unbundling disoriented pitch angle. (b) Illustration of an unbundling disoriented pitch angle θ. The angle is defined as the angle between the body orientation vector and the wall at the end of the unbundling disoriented phase of a tumble. The angle ranges from $-90°$(body pointing to the wall) to $90°$(body pointing to the bulk). The plot in (a) is smoothed by the convolve method.

FIGURE 6.4(a) shows the distribution of unblundling disoriented pitch angle(θ). θ is defined as the angle between the orientation vector of the body and the wall at t_{ept}, as illustrated in FIGURE 6.4(b). The blue data points show the statistics of θs before successful escapes, while the orange dots are for failed ones. Note that the differences between θ and θ_{out} (section 6.2.1) lie in two aspects: 1) θ_{out} is measured when the *E. Coli* has already left the surface region, while the *E. Coli* is still near the surface for the measurements of θ. 2) θ_{out} is the angle between the orientation vector of a bundled configuration and the wall (Junot et al., 2022), in contrast to what is shown in FIGURE 6.4(b). As shown in FIGURE 6.2, the orientation of *E. Coli* changes erratically during the unbundling disoriented phase because the change of the handedness of the tumbling flagellum induces a repulsive flow field. However, when the unbundling oriented phase starts, the tumbling flagellum changes back to being left-handed, so the flagella attract each other again, form a bundle. Hence,

they bundle together but do not further reorient the body much. Therefore, $p(\theta)$ shows the correlation between the body orientation change due to the flagella interaction during tumbling and the success rate of escaping. In the measurement of θ_{out}, the hindrance by the wall is more significant, as the *E. Coli* has already finished its successful tumble, and goes through a complex interaction with the wall to finally escape. The range of θ is defined from -90° to 90° [FIGURE 6.4(b)].

As shown in FIGURE 6.4(a), a larger θ positively correlates with a successful escape. In other words, *E. Coli* is more likely to escape if the body points more towards the bulk at the end of unbundled disoriented phase. It is also supported by the smaller θ values for the failed escapes (orange). We obtained $p = 1/2.9$ from the binomial fit in FIGURE 6.3(b). We can therefore calculate the minimum pitch angle (θ_{min}) required for a successful leave in FIGURE 6.4(a) as $\int_{\theta_{min}}^{90^\circ} p(\theta)\, d\theta = 1/2.9$, we obtain $\theta_{min} \approx 35^\circ$. The range of $35^\circ - 90^\circ$ indeed represent roughly $1/3$ of the semi circle from -90° to 90°. Therefore, the successful escape is a random event, as it purely depends on whether the body orientation vector points to the appropriate range of directions at t_{ept}.

6.3 Conclusion and discussion

In this part, we investigated how *E. Coli* uses tumbling to escape from the surface. Previous study by Junot et al., 2022 presents experiments with wild-type *E. Coli* and simulations by using the "behavioral variability" model. They conclude that tumbling is an efficient mean for wild-type *E. Coli* to escape from the surface despite being trapped at the surface longer than the typical run time. In our work, we ran several simulations and collected 38 instances of escaping of *E. Coli* from a surface. In section 6.2.1, distribution of the escape angle is presented where it is defined as the angle between the bundled *E. Coli* during escaping and the surface. Simulation data shows a peak at $10 - 20^\circ$ [FIGURE 6.3(a)], which is slightly smaller than the peak in experimental statistics at $20 - 40^\circ$, reported in Junot et al., 2022. This might be due to a limited sample collected in our work as well as different setups in simulations and experiments. Distributions of number of tumbles before escaping were also compared and agree well with the results from the "BV" model (See section 2.3.4 for the details of the model) in Junot et al., 2022. The distribution in FIGURE 6.3(b) can be described well by a binomial fit of $p = 1/2.9$ in both our work and Junot et al., 2022. However, our statistics is more scattered around the fit. $p \approx 1/3$ indicates the existence of a minimum unbundling disoriented pitch angle for a successful escape. Unbundling disoriented pitch angle θ is defined as the pitch angle of a *E. Coli* at the end of the unbundling disoriented phase (t_{ept}) when the *E. Coli*'s orientation changes erractically. Note that the value of the angle θ largely depends on the hydrodynamic interaction between flagella during tumbling. FIGURE 6.4 plots the angle distribution for successful and failed escapes, demonstrating the positive correlation between the successful escape and a larger value of θ. Also, with $p \approx 1/3$ from FIGURE 6.3(b), we estimate the minimum unbundling disoriented pitch angle for a successful escape to be $\theta_{min} \approx 35^\circ$, and the range of $35 - 90^\circ$ indeed roughly corresponds to $1/3$ of a range from -90° to 90°.

These results together firstly support the validity of our model through the favorable comparison of our results to those in Junot et al., 2022. Secondly, we conclude that a successful escape of *E. Coli* from a surface depends on the body orientation directly after the erratic movement due to tumbling. If the body points within the range of $35 - 90^\circ$ with respect to the wall after a tumble, the *E. Coli* has a good

chance of leaving the surface. Our work is limited by the small sample of escaping events, resulting in some discrepancies in the results between our work and Junot et al., 2022. Nevertheless, the model provides a reliable way to investigate further interesting aspects of the behavior of swimmers, such as smooth *E. Coli* swimming in a circle near a wall, *E. Coli* behavior in a liquid crystal or porous media.

Chapter 7

Summary, Conclusions and Outlook

In this dissertation, we have focused on the behavior of single microswimmer and their collectives at low Reynolds numbers by performing mesoscale hydrodynamic simulations. Microswimmers, such as *E. Coli* are typically modeled as active particles with a characteristic persistent motion. A collective of microswimmers is out of equilibrium, and can have long-range correlations and large-scale structures, characterized by physical phenomena such as motility-induced phase separation, swarming, and active turbulence. A prominent instance of the collective behavior of biological microswimmers is biofilms, which are complex and dynamic communities of microorganisms that adhere to surfaces with a protective layer on top (Hall-Stoodley, Costerton, and Stoodley, 2004; Verstraeten et al., 2008). They are the causes for various infectious diseases such as dental plaque on the teeth (Marsh, 2006). Therefore, studying the systems mimicking biofilms brings insights into medicine protections.

An important aspect in these systems is the formation of some collective patterns in a system of microswimmers confined within a thin fluid film. This geometry allows the free orientation of spheroidal swimmers within the confinement, but constraints them into a two-layer structure at maximum. The microswimmers are modeled by squirmers, which mimic the near-field hydrodynamics by a prescribed slip velocity at their surfaces. The model allows the representation of different swimming modes, such as pullers, neutral squirmers, and pushers. We investigate the effect of several parameters, including the volume fraction of squirmers, their swimming modes, and their rotlet dipole strength, on their collective behavior. We find that "gaseous phases" are formed at low packing fractions. With an increase in the packing fraction, a swarming state is observed at intermediate packing fractions where mobile clusters are formed with a wide range of sizes. At large enough packing fractions, motility-induced phase separation (MIPS) is observed as an immobile cluster with a size comparable to the system size, surrounded by a few mobile squirmers. Furthermore, the puller squirmers undergo MIPS at the lowest packing fraction due to their attractive hydrodynamic interactions. For the systems without rotlet dipole at intermediate packing fractions, swarming states exist for the systems of pushers rather than pullers, suggesting that attractive hydrodynamic interactions between swimmers suppress the formation of swarming clusters. Also, our simulations reveal that the effect of a rotlet dipole minimizes the difference in the collective behavior of squirmers with different swimming modes. The elongated shape of the squirmers provides an alignment interaction, which has been observed before for self-propelled rods, spheroids, and semi-flexible filaments (Peruani, Deutsch, and Bär, 2006; Theers et al., 2018; Duman et al., 2018). The alignment interaction also contributes to the swarming clusters. Moreover, the interaction between squirmers and the confining walls strongly affects collective behavior. Firstly, pullers favor a

nearly perpendicular orientation with the walls, while pushers and neutral squirmers favor a configuration parallel to the walls. The perpendicular-to-the-wall configuration results in the formation of flower-like clusters, where a single puller is oriented nearly perpendicular to the wall, surrounded by a few petal pullers due to collisions. Such structures act as a nucleation of clusters for pullers even at low packing fractions, hindering the motility of pullers and promoting MIPS. In contrast, pushers can frequently switch between the layers due to the parallel-to-the-wall orientation, delaying the formation of large immobile clusters with increasing packing fraction. Therefore, a pusher swimmer such as *E. Coli* should be able to leave the initial mono-layer structure and form a multi-layer configuration. This process contribute to the growth of biofilm.

Peritichous bacteria propelled by a bundle of rotating flagella. In order to study the dynamics induced by the flagella, we develop a realistic and flexible *E. Coli* model with the ability to capture run and tumble behavior. We illustrate a few parameters that affect the swimming behavior of *E. Coli*, including the shape of the body and flagella, polymorphic transformation of flagella, and dynamic hook stiffening. The shape of the body and flagella affects the ratio between the rotational frequencies of the body and the flagellar bundle. In experiments, the ratio is close to $1/5$ for wild-type *E. Coli* (Turner, Ryu, and Berg, 2000). With a different body shape, for example, the spheroidal shape, the ratio is close to $1/2$, such that the rotation of tumbling flagella is too fast and it wraps around the body during tumbling. Thus, the re-reorientation of the body is significantly limited. The sphero-cylindrical body provides a ratio of $1/5$ between the body and bundle rotation frequencies. This ratio is small enough so that the fast rotation of flagella yields a fast swimming speed, and does not impose a fast rotation of the body, benefiting the tumbling phase. Another important aspect is the applied torque on the base of the flagella, mimicking the actuation of motors in *E. Coli*. If the value of the torque is too small, the flagellar bundle is not tight due to weak flows, resulting in a poor propulsion of *E. Coli*. Furthermore, the polymorphic transformation of the tumbling flagella is crucial for tumbling, as observed in experiments (Darnton et al., 2007; Turner, Ryu, and Berg, 2000; Berg, 2004). This transformation involves the change of handedness of the tumbling flagellum (from left-handed to right-handed) in the beginning and (from right-handed to left-handed) at the end of a tumble. During tumbling, the right-handed clockwise rotating flagella have a flow field propelling itself in a direction close to the swimming direction, so they can escape from the bundle quickly and not disturb the structure of the flagellar bundle. A recent study (Zhang et al., 2023) suggests the bending stiffness of a hook is higher when it rotates clockwise than counter-clockwise. We have implemented the idea into our model. During tumbling, the tumbling flagella can leave the bundle more efficiently with a stiff hook, while the other flagella stay in the tight bundle with soft hooks. The model properly reproduces experimental observations and measurements such as rotation frequency of the body and flagellar bundle, swimming speed, and tumble angle. However, the simulations of *E. Coli* with different numbers of flagella or different arrangements of flagella demonstrate a substantial variety in run-and-tumble behavior, which is also observed in experiments. For simplicity, we choose a base model of a *E. Coli* constructed with $N_{flag} = 5$ symmetrically placed flagella at one of the body ends. A random distribution of flagella attachment points at the whole surface of the body may result in a model whose run-and-tumble behavior strongly differs from that exhibited by the base model, complicating the generality of *E. Coli* swimming behavior.

The developed *E. Coli* model developed can be used to address some questions

related to *E. Coli* behavior in complex environments. For example, a recent experimental investigation (Junot et al., 2022) suggests that *E. Coli* tumbling is the dominant mechanism for a bacterium to escape from the wall. As *E. Coli*-like bacteria are subject to "wall entrapment" effect, however this is devastating for their survival, because they need to explore the space for nutrition. Various theories have been proposed to explain how bacteria can escape from a wall (Dunstan et al., 2012; Guccione et al., 2017; Molaei et al., 2014; Junot et al., 2022), but the underlying physical mechanism is unclear. We have performed simulations of the bacterium swimming near a wall. The simulations show that a successful escape always happens directly after a tumble. We define the successful escape as the distance between the centroid of the body and the wall exceeding $3\mu m$. We collect many instances of successful escapes and plot the distribution of escape angles and the number of tumbles before escaping to compare with the results from Junot *et al.* (Junot et al., 2022). A binomial to distribution of the number of tumbles before escaping with the success probability of about a third is found. Furthermore, an unbundling disoriented pitch angle (θ) is defined to describe the angle between the body orientation and the wall at the end of the polymorphic transformation directly before a run phase. The distribution of θ shows that *E. Coli* is more likely to escape when its orientation points more toward the bulk. The escape probability can be used to calculate the minimum of θ, and we obtain a value of 35°, indicating the optimal range of escaping angles is between 35° and 90°. Therefore, a successful escape is a random event, depending on whether the body orientation vector points to the appropriate range at the end of tumbling.

There are a few ways to extend the projects presented in the thesis. Firstly, we can consider a study of the collective behavior of microswimmers simulated by the detailed *E. Coli* model rather than the squirmer model. Squirmers have the advantage of their simplicity and flexibility in modeling the near-field hydrodynamics of various swimming modes. However, the real near-field hydrodynamics of bacteria is far more complicated, as it depends on various factors, such as the body shape, the geometry and dynamics of propelling flagella, and different motility patterns. Also, the steric interaction between bacteria involves the motion of flagella and the body, which are hardly captured by idealized spheroidal shapes. Therefore, employing the detailed model can make simulations more realistic and advance our understanding of bacterial interactions within biofilms. However, such simulations are currently limited by computational resources. Secondly, we can consider a study of collective behavior within thicker films. Biofilms *in vivo* are bounded by a solid wall and an air-water interface. With a thicker film, simulated microswimmers are less likely to interact with their periodic images, so the structural and dynamical properties of the system can be more comparable to the corresponding experimental observations. Also, active turbulence can occur at smaller packing fractions for thick films so that more collective phenomena can be studied. Thirdly, the detailed *E. Coli* model can be used to investigate the *E. Coli* behavior in complex environments where the resolution of experimental observation is not high enough to propose an underlying physical mechanism. For example, the circling motion of smoothed *E. Coli* near walls, since the relationship of the physical properties of *E. Coli* with the radius of circulation is still not clear. Another example is *E. Coli* swimming within lipid vesicles, leading to the formation of thin tethers and overall vesicle transport by the encapsulated bacteria (Le Nagard et al., 2022).

Bibliography

Alarcón, F. and I. Pagonabarraga (2013). "Spontaneous aggregation and global polar ordering in squirmer suspensions". In: *J. Mol. Liquids* 185, pp. 56–61.

Alarcón, F., C. Valeriani, and I. Pagonabarraga (2017). "Morphology of clusters of attractive dry and wet self-propelled spherical particle suspensions". In: *Soft Matter* 13, pp. 814–826.

Alert, Ricard, Jean-François Joanny, and Jaume Casademunt (2020). "Universal scaling of active nematic turbulence". In: *Nature Physics* 16.6, pp. 682–688.

Alexander, G. P., C. M. Pooley, and J. M. Yeomans (2008). "Scattering of low-Reynolds-number swimmers". In: *Phys. Rev. E* 78, p. 045302.

Allen, A., O. Habimana, and E. Casey (2018). "The effects of extrinsic factors on the structural and mechanical properties of *Pseudomonas fluorescens* biofilms: a combined study of nutrient concentrations and shear conditions". In: *Colloid. Surf. B* 165, pp. 127–134.

Allen, M. P. and D. J. Tildesley (1991). *Computer simulation of liquids*. New York: Clarendon Press.

Alon, R. et al. (1997). "The kinetics of L-selectin tethers and the mechanics of selectin-mediated rolling". In: *J. Cell Biol.* 138, pp. 1169–1180.

Alon, Uri et al. (1998). "Response regulator output in bacterial chemotaxis". In: *The EMBO journal*.

Alvarez, Luis et al. (2014). "The computational sperm cell". In: *Trends in cell biology* 24.3, pp. 198–207.

Ariel, Gil et al. (2013). "From organized internal traffic to collective navigation of bacterial swarms". In: *New Journal of Physics* 15.12, p. 125019.

Ariel, Gil et al. (2018). "Collective dynamics of two-dimensional swimming bacteria: Experiments and models". In: *Physical Review E* 98.3, p. 032415.

Attinger, C. and R. Wolcott (2012). "Clinically addressing biofilm in chronic wounds". In: *Adv. Wound Care* 1, pp. 127–132.

Babu, S. B. and H. Stark (2012). "Modeling the locomotion of the african trypanosome using multi-particle collision dynamics". In: *New J. Phys.* 14, p. 085012.

Bárdfalvy, D. et al. (2019). "Particle-resolved lattice Boltzmann simulations of 3-dimensional active turbulence". In: *Soft Matter* 15, pp. 7747–7756.

Batchelor, George Keith (1953). *The theory of homogeneous turbulence*. Cambridge university press.

Bechinger, C. et al. (2016). "Active particles in complex and crowded environments". In: *Rev. Mod. Phys.* 88, p. 045006.

Be'er, A. et al. (2020). "A phase diagram for bacterial swarming". In: *Commun. Phys.* 3, p. 66.

Be'er, Avraham et al. (2009). "Paenibacillus dendritiformis bacterial colony growth depends on surfactant but not on bacterial motion". In: *Journal of bacteriology* 191.18, pp. 5758–5764.

Be'er, Avraham et al. (2013). "Periodic reversals in Paenibacillus dendritiformis swarming". In: *Journal of bacteriology* 195.12, pp. 2709–2717.

Ben-Jacob, Eshel et al. (2001). "Modeling branching and chiral colonial patterning of lubricating bacteria". In: *Mathematical models for biological pattern formation*. Springer, pp. 211–253.

Benisty, Sivan et al. (2015). "Antibiotic-induced anomalous statistics of collective bacterial swarming". In: *Physical review letters* 114.1, p. 018105.

Berg, H. C. (2003). "The rotary motor of bacterial flagella". In: *Annu. Rev. Biochem.* 72, pp. 19–54.

Berg, H. C. and D. A. Brown (1972). "Chemotaxis in Escherichia coli analysed by three-dimensional tracking". In: *Nature* 239, pp. 500–504.

Berg, HC (1977). "EM Purcell Physics of chemoreception". In: *Biophys J* 20, pp. 193–219.

Berg, Howard C (2004). *E. coli in Motion*. Springer.

Berke, A. P. et al. (2008). "Hydrodynamic attraction of swimming microorganisms by surfaces". In: *Phys. Rev. Lett.* 101, ppt.

Berne, C. et al. (2018). "Bacterial adhesion at the single-cell level". In: *Nat. Rev. Microbiol.* 16, pp. 616–627.

Bhattacharjee, T. and S. S. Datta (2019). "Bacterial hopping and trapping in porous media". In: *Nat. Comm.* 10, p. 2075.

Bialké, J., H. Löwen, and T. Speck (2013). "Microscopic theory for the phase separation of self-propelled repulsive disks". In: *Europhys. Lett.* 103, p. 30008.

Bialké, J., T. Speck, and H. Löwen (2012). "Crystallization in a dense suspension of self-propelled particles". In: *Phys. Rev. Lett.* 108, p. 168301.

Bianchi, S et al. (2015). "Polar features in the flagellar propulsion of E. coli bacteria". In: *Physical Review E* 91.6, p. 062705.

Bianchi, Silvio, Filippo Saglimbeni, and Roberto Di Leonardo (2017). "Holographic imaging reveals the mechanism of wall entrapment in swimming bacteria". In: *Physical Review X* 7.1, p. 011010.

Bickel, T., A. Majee, and A. Würger (2013). "Flow pattern in the vicinity of self-propelling hot Janus particles". In: *Phys. Rev. E* 88, p. 012301.

Billington, Karen et al. (2023). "Genome-wide subcellular protein map for the flagellate parasite Trypanosoma brucei". In: *Nature microbiology* 8.3, pp. 533–547.

Blair, David F (1995). "How bacteria sense and swim". In: *Annual review of microbiology* 49.1, pp. 489–520.

Blake, J. R. (1971). "A spherical envelope approach to ciliary propulsion". In: *J. Fluid Mech.* 46, pp. 199–208.

Blaschke, J. et al. (2016). "Phase separation and coexistence of hydrodynamically interacting microswimmers". In: *Soft Matter* 12, pp. 9821–9831.

Block, Steven M, David F Blair, and Howard C Berg (1991). "Compliance of bacterial polyhooks measured with optical tweezers". In: *Cytometry: The Journal of the International Society for Analytical Cytology* 12.6, pp. 492–496.

Block, Steven M, Jeffery E Segall, and Howard C Berg (1983). "Adaptation kinetics in bacterial chemotaxis". In: *Journal of bacteriology* 154.1, pp. 312–323.

Bondarenko, Volodymyr and Jacky Cosson (2019). "Structure and beating behavior of the sperm motility apparatus in aquatic animals". In: *Theriogenology* 135, pp. 152–163.

Bratanov, Vasil, Frank Jenko, and Erwin Frey (2015). "New class of turbulence in active fluids". In: *Proceedings of the National Academy of Sciences* 112.49, pp. 15048–15053.

Braun, Marco and Frank Cichos (2013). "Optically controlled thermophoretic trapping of single nano-objects". In: *ACS nano* 7.12, pp. 11200–11208.

Brown, M. T. et al. (2012). "Flagellar hook flexibility is essential for bundle formation in swimming *Escherichia coli* cells". In: *J. Bacteriol.* 194, pp. 3495–3501.

Brown, Robert (1828). "Microscopical observations". In: *Philos. Mag* 4.21, pp. 161–173.

Bunde, Armin et al. (2017). *Diffusive Spreading in Nature, Technology and Society*. Springer.

Buttinoni, I. et al. (2013). "Dynamical clustering and phase separation in suspensions of self-propelled colloidal particles". In: *Phys. Rev. Lett.* 110, p. 238301.

Buyl, P. de and R. Kapral (2013). "Phoretic self-propulsion: a mesoscopic description of reaction dynamics that powers motion". In: *Nanoscale* 5, pp. 1337–1344.

Cates, M. E. and J. Tailleur (2015). "Motility-induced phase separation". In: *Annu. Rev. Condens. Matter Phys.* 6, pp. 219–244.

Chattopadhyay, Suddhashil et al. (2006). "Swimming efficiency of bacterium Escherichia coli". In: *Proceedings of the National Academy of Sciences* 103.37, pp. 13712–13717.

Chen, Xiao et al. (2012). "Scale-invariant correlations in dynamic bacterial clusters". In: *Physical review letters* 108.14, p. 148101.

Cluzel, Philippe, Michael Surette, and Stanislas Leibler (2000). "An ultrasensitive bacterial motor revealed by monitoring signaling proteins in single cells". In: *Science* 287.5458, pp. 1652–1655.

Compant, Stéphane et al. (2019). "A review on the plant microbiome: ecology, functions, and emerging trends in microbial application". In: *Journal of advanced research* 19, pp. 29–37.

Condiff, D. W. and J. S. Dahler (1964). "Fluid mechanical aspects of antisymmetric stress". In: *Phys. Fluids* 7, pp. 842–854.

Copeland, Matthew F and Douglas B Weibel (2009). "Bacterial swarming: a model system for studying dynamic self-assembly". In: *Soft matter* 5.6, pp. 1174–1187.

Copeland, Matthew F et al. (2010). "Studying the dynamics of flagella in multicellular communities of Escherichia coli by using biarsenical dyes". In: *Applied and environmental microbiology* 76.4, pp. 1241–1250.

Cosson, Jacky et al. (2008). "Marine fish spermatozoa: racing ephemeral swimmers". In: *Reproduction* 136.3, pp. 277–294.

Costerton, J William et al. (1987). "Bacterial biofilms in nature and disease". In: *Annual Reviews in Microbiology* 41.1, pp. 435–464.

Courtney, Colleen R, Loralyn M Cozy, and Daniel B Kearns (2012). "Molecular characterization of the flagellar hook in Bacillus subtilis". In: *Journal of bacteriology* 194.17, pp. 4619–4629.

Darnige, T. et al. (2017). "Lagrangian 3D tracking of fluorescent microscopic objects in motion". In: *Rev. Sci. Instrum.* 88, p. 055106.

Darnton, N. C. et al. (2007). "On torque and tumbling in swimming *Escherichia coli*". In: *J. Bacteriol.* 189, pp. 1756–1764.

Darnton, Nicholas C et al. (2010). "Dynamics of bacterial swarming". In: *Biophysical journal* 98.10, pp. 2082–2090.

Das, Shibananda, Gerhard Gompper, and Roland G Winkler (2018). "Confined active Brownian particles: theoretical description of propulsion-induced accumulation". In: *New Journal of Physics* 20.1, p. 015001.

Delmotte, B. et al. (2015). "Large-scale simulation of steady and time-dependent active suspensions with the force-coupling method". In: *J. Comp. Phys.* 302, pp. 524–547.

Denissenko, Petr et al. (2012). "Human spermatozoa migration in microchannels reveals boundary-following navigation". In: *Proceedings of the National Academy of Sciences* 109.21, pp. 8007–8010.

Dhont, J. K. G. (1996). *An introduction to dynamics of colloids*. Amsterdam: Elsevier.
Digregorio, P. et al. (2018). "Full phase diagram of active Brownian disks: from melting to motility-induced phase separation". In: *Phys. Rev. Lett.* 121, p. 098003.
Doi, Masao (2013). *Soft matter physics*. Oxford University Press, USA.
Dombrowski, Christopher et al. (2004). "Self-concentration and large-scale coherence in bacterial dynamics". In: *Physical review letters* 93.9, p. 098103.
Doostmohammadi, Amin et al. (2015). "Celebrating Soft Matter's 10th Anniversary: Cell division: a source of active stress in cellular monolayers". In: *Soft Matter* 11.37, pp. 7328–7336.
Doostmohammadi, Amin et al. (2017). "Onset of meso-scale turbulence in active nematics". In: *Nature communications* 8.1, p. 15326.
Drescher, K. et al. (2011). "Fluid dynamics and noise in bacterial cell-cell and cell-surface scattering". In: *Proc. Natl. Acad. Sci. USA* 108, pp. 10940–10945.
Drescher, Knut et al. (2009). "Dancing volvox: hydrodynamic bound states of swimming algae". In: *Physical review letters* 102.16, p. 168101.
Drescher, Knut et al. (2010). "Direct measurement of the flow field around swimming microorganisms". In: *Physical Review Letters* 105.16, p. 168101.
Dreyfus, R. et al. (2005). "Microscopic artificial swimmers". In: *Nature* 437, pp. 862–865.
Duman, Ö. et al. (2018). "Collective dynamics of self-propelled semiflexible filaments". In: *Soft Matter* 14, pp. 4483–4494.
Dunkel, J. et al. (2013). "Fluid dynamics of bacterial turbulence". In: *Phys. Rev. Lett.* 110, p. 228102.
Dunstan, Jocelyn et al. (2012). "A two-sphere model for bacteria swimming near solid surfaces". In: *Physics of Fluids* 24.1.
Edwards, Sarah J and Birthe V Kjellerup (2013). "Applications of biofilms in bioremediation and biotransformation of persistent organic pollutants, pharmaceuticals/personal care products, and heavy metals". In: *Applied microbiology and biotechnology* 97, pp. 9909–9921.
Einstein, Albert (1905). "Über die von der molekularkinetischen Theorie der Wärme geforderte Bewegung von in ruhenden Flüssigkeiten suspendierten Teilchen". In: *Annalen der physik* 4.
Eisenbach, Michael and Laura C Giojalas (2006). "Sperm guidance in mammals—an unpaved road to the egg". In: *Nature reviews Molecular cell biology* 7.4, pp. 276–285.
Elgeti, J. and G. Gompper (2013). "Wall accumulation of self-propelled spheres". In: *Europhys. Lett.* 101, p. 48003.
Elgeti, J., R. G. Winkler, and G. Gompper (2015). "Physics of microswimmers - single particle motion and collective behavior: a review". In: *Rep. Prog. Phys.* 78, p. 056601.
Elgeti, Jens and Gerhard Gompper (2009). "Self-propelled rods near surfaces". In: *Europhysics Letters* 85.3, p. 38002.
Emonet, Thierry and Philippe Cluzel (2008). "Relationship between cellular response and behavioral variability in bacterial chemotaxis". In: *Proceedings of the National Academy of Sciences* 105.9, pp. 3304–3309.
Español, P. (1998). "Fluid particle model". In: *Phys. Rev. E* 57, pp. 2930–2948.
Español, P. and M. Revenga (2003). "Smoothed dissipative particle dynamics". In: *Phys. Rev. E* 67, p. 026705.
Español, P. and P. Warren (1995). "Statistical mechanics of dissipative particle dynamics". In: *Europhys. Lett.* 30, pp. 191–196.

Evans, A. A. et al. (2011). "Orientational order in concentrated suspensions of spherical microswimmers". In: *Phys. Fluids* 23, p. 111702.

Ezhilan, Barath, Roberto Alonso-Matilla, and David Saintillan (2015). "On the distribution and swim pressure of run-and-tumble particles in confinement". In: *Journal of Fluid Mechanics* 781, R4.

Falasco, Gianmaria et al. (2014). "Effective temperatures of hot Brownian motion". In: *Physical Review E* 90.3, p. 032131.

Fan, X. et al. (2006). "Simulating flow of DNA suspension using dissipative particle dynamics". In: *Phys. Fluids* 18, p. 063102.

Fedosov, D. A., B. Caswell, and G. E. Karniadakis (2010). "A multiscale red blood cell model with accurate mechanics, rheology, and dynamics". In: *Biophys. J.* 98, pp. 2215–2225.

Fedosov, D. A., H. Noguchi, and G. Gompper (2014). "Multiscale modeling of blood flow: from single cells to blood rheology". In: *Biomech. Model. Mechanobiol.* 13, pp. 239–258.

Fedosov, D. A., M. Peltomäki, and G. Gompper (2014). "Deformation and dynamics of red blood cells in flow through cylindrical microchannels". In: *Soft Matter* 10, pp. 4258–4267.

Fedosov, D. A. et al. (2014). "Computational biorheology of human blood flow in health and disease". In: *Ann. Biomed. Eng.* 42, pp. 368–387.

Figueroa-Morales, Nuris et al. (2020). "3D spatial exploration by E. coli echoes motor temporal variability". In: *Physical Review X* 10.2, p. 021004.

Fily, Y., A. Baskaran, and M. F. Hagan (2014). "Dynamics of self-propelled particles under strong confinement". In: *Soft Matter* 10, pp. 5609–5617.

Fily, Y. and M. C. Marchetti (2012). "Athermal phase separation of self-propelled particles with no alignment". In: *Phys. Rev. Lett.* 108, p. 235702.

Fleming, D and K Rumbaugh (2018). *The consequences of biofilm dispersal on the host. Sci Rep 8: 10738*.

Flemming, H.-C., J. Schmitt, and K. C. Marshall (1996). "Sorption properties of biofilms". In: *Sediments and toxic substances: environmental effects and ecotoxicity*. Ed. by W. Calmano and U. Förstner. Heidelberg: Springer, pp. 115–157.

Flemming, H.-C. and J. Wingender (2010). "The biofilm matrix". In: *Nat. Rev. Microbiol.* 8, pp. 623–633.

Flores, Heather et al. (2005). "A study of bacterial flagellar bundling". In: *Bulletin of mathematical biology* 67, pp. 137–168.

Foissner, Wilhelm, Anne Chao, and Laura A Katz (2009). *Diversity and geographic distribution of ciliates (Protista: Ciliophora)*. Springer.

Fournier-Bidoz, Sébastien et al. (2005). "Synthetic self-propelled nanorotors". In: *Chemical Communications* 4, pp. 441–443.

Frangipane, G. et al. (2019). "Invariance properties of bacterial random walks in complex structures". In: *Nat. Comm.* 10, p. 2442.

Friedrich, Benjamin M and Frank Jülicher (2007). "Chemotaxis of sperm cells". In: *Proceedings of the National Academy of Sciences* 104.33, pp. 13256–13261.

Frymier, P. D. et al. (1995). "Three-dimensional tracking of motile bacteria near a solid planar surface". In: *Proc. Natl. Acad. Sci. USA* 92, pp. 6195–6199.

Ginot, Félix et al. (2015). "Nonequilibrium equation of state in suspensions of active colloids". In: *Physical Review X* 5.1, p. 011004.

Gloag, E. S. et al. (2013). "Self-organization of bacterial biofilms is facilitated by extracellular DNA". In: *Proc. Natl. Acad. Sci. USA* 110, pp. 11541–11546.

Golestanian, R., T. B. Liverpool, and A. Ajdari (2005). "Propulsion of a molecular machine by asymmetric distribution of reaction products". In: *Phys. Rev. Lett.* 94, p. 220801.

Golestanian, Ramin (2009). "Anomalous diffusion of symmetric and asymmetric active colloids". In: *Physical review letters* 102.18, p. 188305.

Gompper, G. et al. (2009). "Multi-particle collision dynamics: a particle-based mesoscale simulation approach to the hydrodynamics of complex fluids". In: *Adv. Polym. Sci.* 221, pp. 1–87.

Gompper, G. et al. (2020). "The 2020 motile active matter roadmap". In: *J. Phys.: Condens. Matter* 32, p. 193001.

Götze, I. O. and G. Gompper (2011). "Flow generation by rotating colloids in planar microchannels". In: *Europhys. Lett.* 92, p. 64003.

Götze, I. O., H. Noguchi, and G. Gompper (2007). "Relevance of angular momentum conservation in mesoscale hydrodynamics simulations". In: *Phys. Rev. E* 76, p. 046705.

Groot, R. D. and P. B. Warren (1997). "Dissipative particle dynamics: bridging the gap between atomistic and mesoscopic simulation". In: *J. Chem. Phys.* 107, pp. 4423–4435.

Grosser, Steffen et al. (2021). "Cell and nucleus shape as an indicator of tissue fluidity in carcinoma". In: *Physical Review X* 11.1, p. 011033.

Guasto, Jeffrey S, Karl A Johnson, and Jerry P Gollub (2010). "Oscillatory flows induced by microorganisms swimming in two dimensions". In: *Physical review letters* 105.16, p. 168102.

Guccione, Giorgia et al. (2017). "Diffusivity of E. coli-like microswimmers in confined geometries: The role of the tumbling rate". In: *Physical Review E* 96.4, p. 042603.

Guo, H. et al. (2018a). "Bistability in the synchronization of actuated microfilaments". In: *J. Fluid Mech.* 836, pp. 304–323.

Guo, S. et al. (2018b). "Symmetric shear banding and swarming vortices in bacterial superfluids". In: *Proc. Natl. Acad. Sci. USA* 115, pp. 7212–7217.

Guttenplan, Sarah B, Sidney Shaw, and Daniel B Kearns (2013). "The cell biology of peritrichous flagella in B acillus subtilis". In: *Molecular microbiology* 87.1, pp. 211–229.

Hall-Stoodley, L., J. W. Costerton, and P. Stoodley (2004). "Bacterial biofilms: from the natural environment to infectious diseases". In: *Nat. Rev. Microbiol.* 2, pp. 95–108.

Harris, Elizabeth H (1989). *Chlamydomonas sourcebook*. Vol. 2. Academic Press San Diego.

Harshey, Rasika M (2003). "Bacterial motility on a surface: many ways to a common goal". In: *Annual Reviews in Microbiology* 57.1, pp. 249–273.

Hartmann, Raimo et al. (2019). "Emergence of three-dimensional order and structure in growing biofilms". In: *Nature physics* 15.3, pp. 251–256.

Heddergott, N. et al. (2012). "Trypanosome motion represents an adaptation to the crowded environment of the vertebrate bloodstream". In: *PLoS Pathog.* 8, e1003023.

Helbing, Dirk et al. (2001). "Self-organizing pedestrian movement". In: *Environment and planning B: planning and design* 28.3, pp. 361–383.

Helfrich, W. (1973). "Elastic properties of lipid bilayers: theory and possible experiments". In: *Z. Naturforsch.* 28, pp. 693–703.

Henrichsen, Jφrgen (1972). "Bacterial surface translocation: a survey and a classification". In: *Bacteriological reviews* 36.4, pp. 478–503.

Hohenegger, Christel and Michael J Shelley (2010). "Stability of active suspensions". In: *Physical Review E—Statistical, Nonlinear, and Soft Matter Physics* 81.4, p. 046311.

Hoogerbrugge, P. J. and J. M. V. A. Koelman (1992). "Simulating microscopic hydrodynamic phenomena with dissipative particle dynamics". In: *Europhys. Lett.* 19, pp. 155–160.

Howes, Philip D, Rona Chandrawati, and Molly M Stevens (2014). "Colloidal nanoparticles as advanced biological sensors". In: *Science* 346.6205, p. 1247390.

Hu, J. et al. (2015a). "Modelling the mechanics and hydrodynamics of swimming E. coli". In: *Soft Matter* 11, pp. 7867–7876.

Hu, J. et al. (2015b). "Physical sensing of surface properties by microswimmers – directing bacterial motion via wall slip". In: *Sci. Rep.* 5, p. 9586.

Hyon, Yunkyong et al. (2012). "The wiggling trajectories of bacteria". In: *Journal of Fluid Mechanics* 705, pp. 58–76.

Ilina, Olga et al. (2020). "Cell–cell adhesion and 3D matrix confinement determine jamming transitions in breast cancer invasion". In: *Nature cell biology* 22.9, pp. 1103–1115.

Ilkanaiv, Bella et al. (2017). "Effect of cell aspect ratio on swarming bacteria". In: *Physical review letters* 118.15, p. 158002.

Ishibashi, Kenta, Hitoshi Sakakibara, and Kazuhiro Oiwa (2020). "Force-generating mechanism of axonemal dynein in solo and ensemble". In: *International Journal of Molecular Sciences* 21.8, p. 2843.

Ishikawa, T., J. T. Locsei, and T. J. Pedley (2008). "Development of coherent structures in concentrated suspensions of swimming model micro-organisms". In: *J. Fluid Mech.* 615, pp. 401–431.

Ishikawa, T. and T. J. Pedley (2007). "Diffusion of swimming model micro-organisms in a semi-dilute suspension". In: *J. Fluid Mech.* 588, pp. 437–462.

Ishikawa, T., M. P. Simmonds, and T. J. Pedley (2006). "Hydrodynamic interaction of two swimming model micro-organisms". In: *J. Fluid Mech.* 568, pp. 119–160.

Ishimoto, K. and E. A. Gaffney (2013). "Squirmer dynamics near a boundary". In: *Phys. Rev. E* 88, p. 062702.

Ishimoto, Kenta and Eric Lauga (2019). "The N-flagella problem: elastohydrodynamic motility transition of multi-flagellated bacteria". In: *Proceedings of the Royal Society A* 475.2225, p. 20180690.

Janssen, PJA and MD Graham (2011). "Coexistence of tight and loose bundled states in a model of bacterial flagellar dynamics". In: *Physical Review E* 84.1, p. 011910.

Jeckel, Hannah et al. (2019). "Learning the space-time phase diagram of bacterial swarm expansion". In: *Proceedings of the National Academy of Sciences* 116.5, pp. 1489–1494.

Jiang, H.-R., N. Yoshinaga, and M. Sano (2010). "Active motion of a Janus particle by self-thermophoresis in a defocused laser beam". In: *Phys. Rev. Lett.* 105, p. 268302.

Junot, G. et al. (2022). "Run-to-tumble variability controls the surface residence times of E. coli bacteria". In: *Phys. Rev. Lett.* 128, p. 248101.

Kaiser, A, HH Wensink, and H Löwen (2012). "How to capture active particles". In: *Physical review letters* 108.26, p. 268307.

Kaiser, Dale (2003). "Coupling cell movement to multicellular development in myxobacteria". In: *Nature Reviews Microbiology* 1.1, pp. 45–54.

— (2007). "Bacterial swarming: a re-examination of cell-movement patterns". In: *Current Biology* 17.14, R561–R570.

Kanehl, Philipp and Takuji Ishikawa (2014). "Fluid mechanics of swimming bacteria with multiple flagella". In: *Physical Review E* 89.4, p. 042704.

Kantsler, Vasily et al. (2013). "Ciliary contact interactions dominate surface scattering of swimming eukaryotes". In: *Proceedings of the National Academy of Sciences* 110.4, pp. 1187–1192.

Kaupp, U Benjamin et al. (2003). "The signal flow and motor response controling chemotaxis of sea urchin sperm". In: *Nature cell biology* 5.2, pp. 109–117.

Kearns, Daniel B (2010). "A field guide to bacterial swarming motility". In: *Nature reviews microbiology* 8.9, pp. 634–644.

Keller, S. R. and T. Y. Wu (1977). "A porous prolate-spheroidal model for ciliated micro-organisms". In: *J. Fluid Mech.* 80, pp. 259–278.

Keymer, J. E. et al. (2006). "Bacterial metapopulations in nanofabricated landscapes". In: *Proc. Nat. Acad. Sci. USA* 103, pp. 17290–17295.

Khan, Shahid and Robert M Macnab (1980). "The steady-state counterclockwise/clockwise ratio of bacterial flagellar motors is regulated by protonmotive force". In: *Journal of molecular biology* 138.3, pp. 563–597.

Kim, Do Kyung and Jon Dobson (2009). "Nanomedicine for targeted drug delivery". In: *Journal of Materials Chemistry* 19.35, pp. 6294–6307.

Kim, M.-J. et al. (2003). "A macroscopic scale model of bacterial flagellar bundling". In: *Proc. Natl. Acad. Sci. USA* 100, pp. 15481–15485.

Kim, Min Jun et al. (2004). "Particle image velocimetry experiments on a macro-scale model for bacterial flagellar bundling". In: *Experiments in fluids* 37, pp. 782–788.

Kim, MunJu and Thomas R Powers (2004). "Hydrodynamic interactions between rotating helices". In: *Physical review E* 69.6, p. 061910.

Kim, S and SJ Karrila (2005). *Resistance and mobility relations*.

Koelman, J. M. V. A. and P. J. Hoogerbrugge (1993). "Dynamic simulations of hard-sphere suspensions under steady shear". In: *Europhys. Lett.* 21, pp. 363–368.

Kong, M. et al. (2015). "A bead-spring model for running and tumbling of flagellated swimmers: detailed predictions compared to experimental data for *E. coli*". In: *Soft Matter* 11, pp. 1572–1581.

Korobkova, E. et al. (2004). "From molecular noise to behavioural variability in a single bacterium". In: *Nature* 428, pp. 574–578.

Korobkova, Ekaterina A et al. (2006). "Hidden stochastic nature of a single bacterial motor". In: *Physical review letters* 96.5, p. 058105.

Kraichnan, R. H. and D. Montgomery (1980). "Two-dimensional turbulence". In: *Rep. Prog. Phys.* 43, pp. 547–619.

Kuhr, J.-T., F. Rühle, and H. Stark (2019). "Collective dynamics in a monolayer of squirmers confined to a boundary by gravity". In: *Soft Matter* 15, pp. 5685–5694.

Kyoya, K. et al. (2015). "Shape matters: near-field fluid mechanics dominate the collective motions of ellipsoidal squirmers". In: *Phys. Rev. E* 92, p. 063027.

Landau, Lev D. and E. M. Lifshitz (2013). *Course of theoretical physics*. Elsevier.

Langer, Robert (1990). "New methods of drug delivery". In: *Science* 249.4976, pp. 1527–1533.

Lauga, E. and T. R. Powers (2009). "The hydrodynamics of swimming microorganisms". In: *Rep. Prog. Phys.* 72, p. 096601.

Lauga, E. et al. (2006). "Swimming in circles: motion of bacteria near solid boundaries". In: *Biophys. J.* 90, pp. 400–412.

Lauga, Eric (2016). "Bacterial hydrodynamics". In: *Annual Review of Fluid Mechanics* 48, pp. 105–130.

Lazarova, V. and J. Manem (1995). "Biofilm characterization and activity analysis in water and wastewater treatment". In: *Water Res.* 29, pp. 2227–2245.

Le Nagard, L. et al. (2022). "Encapsulated bacteria deform lipid vesicles into flagellated swimmers". In: *Proc. Natl. Acad. Sci. USA* 119, e2206096119.

Lee, K. Y. et al. (2018a). "Photosynthetic artificial organelles sustain and control ATP-dependent reactions in a protocellular system". In: *Nat. Biotech.* 36, pp. 530–535.

Lee, Wanho et al. (2018b). "Bacterial flagellar bundling and unbundling via polymorphic transformations". In: *Physical Review E* 98.5, p. 052405.
Lemelle, Laurence et al. (2010). "Counterclockwise circular motion of bacteria swimming at the air-liquid interface". In: *Journal of bacteriology* 192.23, pp. 6307–6308.
Levis, D. and L. Berthier (2014). "Clustering and heterogeneous dynamics in a kinetic Monte Carlo model of self-propelled hard disks". In: *Phys. Rev. E* 89, p. 062301.
Li, G. and J. X. Tang (2009). "Accumulation of microswimmers near a surface mediated by collision and rotational Brownian motion". In: *Phys. Rev. Lett.* 103, p. 078101.
Li, Guanglai et al. (2011). "Accumulation of swimming bacteria near a solid surface". In: *Physical Review E* 84.4, p. 041932.
Li, J. et al. (2008). "Transient functional blood flow change in the human brain measured noninvasively by diffusing-wave spectroscopy". In: *Opt. Lett.* 33, pp. 2233–2235.
Lighthill, James (1976). "Flagellar hydrodynamics". In: *SIAM review* 18.2, pp. 161–230.
Lighthill, M. J. (1952). "On the squirming motion of nearly spherical deformable bodies through liquids at very small Reynolds numbers". In: *Commun. Pure Appl. Math.* 5, pp. 109–118.
Lin, Shao-Zhen et al. (2021). "Energetics of mesoscale cell turbulence in two-dimensional monolayers". In: *Communications Physics* 4.1, p. 21.
Lintuvuori, J. S. et al. (2016). "Hydrodynamic oscillations and variable swimming speed in squirmers close to repulsive walls". In: *Soft Matter* 12, pp. 7959–7968.
Litvinov, S. et al. (2008). "Smoothed dissipative particle dynamics model for polymer molecules in suspension". In: *Phys. Rev. E* 77, p. 066703.
Liu, G. et al. (2019). "Self-driven phase transitions drive Myxococcus xanthus fruiting body formation". In: *Phys. Rev. Lett.* 122, p. 248102.
Lopez, Diego and Eric Lauga (2014). "Dynamics of swimming bacteria at complex interfaces". In: *Physics of Fluids* 26.7.
Lucy, L. B. (1977). "A numerical approach to the testing the fission hypothesis". In: *Astronom. J.* 82, pp. 1013–1024.
Lushi, E., H. Wioland, and R. E. Goldstein (2014). "Fluid flows created by swimming bacteria drive self-organization in confined suspensions". In: *Proc. Natl. Acad. Sci. USA* 111, pp. 9733–9738.
Lynch, JM (1994). "The rhizosphere—form and function". In: *Applied Soil Ecology* 1.3, pp. 193–198.
Maas, Michael (2016). "Carbon nanomaterials as antibacterial colloids". In: *Materials* 9.8, p. 617.
Machemer, Hans (1972). "Ciliary activity and the origin of metachrony in Paramecium: effects of increased viscosity". In: *Journal of Experimental Biology* 57.1, pp. 239–259.
Machemer, Hans and Sigrun Machemer-Röhnisch (1996). "Is gravikinesis in Paramecium affected by swimming velocity?" In: *European Journal of Protistology* 32, pp. 90–93.
Macnab, Robert M (1977). "Bacterial flagella rotating in bundles: a study in helical geometry." In: *Proceedings of the National Academy of Sciences* 74.1, pp. 221–225.
Maggi, Claudio et al. (2015). "Multidimensional stationary probability distribution for interacting active particles". In: *Scientific reports* 5.1, p. 10742.
Malevanets, A. and R. Kapral (1999). "Mesoscopic model for solvent dynamics". In: *J. Chem. Phys.* 110, pp. 8605–8613.

Mann, E. E. and D. J. Wozniak (2012). "Pseudomonas biofilm matrix composition and niche biology". In: *FEMS Microbiol. Rev.* 36, pp. 893–916.

Marsh, P. D. (2006). "Dental plaque as a biofilm and a microbial community–implications for health and disease". In: *BMC Oral Health* 6, S14.

Martinez, V. A. et al. (2020). "A combined rheometry and imaging study of viscosity reduction in bacterial suspensions". In: *Proc. Natl. Acad. Sci. USA* 117, pp. 2326–2331.

Matas-Navarro, R. et al. (2014). "Hydrodynamic suppression of phase separation in active suspensions". In: *Phys. Rev. E* 90, p. 032304.

Mazza, M. G. (2016). "The physics of biofilms-an introduction". In: *J. Phys. D: Appl. Phys.* 49, p. 203001.

Melchior, MB, H Vaarkamp, and J Fink-Gremmels (2006). "Biofilms: a role in recurrent mastitis infections?" In: *The Veterinary Journal* 171.3, pp. 398–407.

Mendelson, Neil H et al. (1999). "Organized cell swimming motions in Bacillus subtilis colonies: patterns of short-lived whirls and jets". In: *Journal of bacteriology* 181.2, pp. 600–609.

Miller, Melissa B and Bonnie L Bassler (2001). "Quorum sensing in bacteria". In: *Annual Reviews in Microbiology* 55.1, pp. 165–199.

Min, Taejin L et al. (2009). "High-resolution, long-term characterization of bacterial motility using optical tweezers". In: *Nature methods* 6.11, pp. 831–835.

Molaei, Mehdi et al. (2014). "Failed escape: solid surfaces prevent tumbling of Escherichia coli". In: *Physical review letters* 113.6, p. 068103.

Monaghan, J. J. (1992). "Smoothed particle hydrodynamics". In: *Annu. Rev. Astron. Astrophys.* 30, pp. 543–574.

Moreira, Camila Alencar et al. (2012). "Biofilm production by clinical staphylococci strains from canine otitis". In: *Brazilian Journal of Microbiology* 43, pp. 371–374.

Müller, K., D. A. Fedosov, and G. Gompper (2014). "Margination of micro- and nanoparticles in blood flow and its effect on drug delivery". In: *Sci. Rep.* 4, p. 4871.

Nagel, Andrew M et al. (2020). "Collective dynamics of model pili-based twitcher-mode bacilliforms". In: *Scientific Reports* 10.1, p. 10747.

Najafi, A. and R. Golestanian (2004). "Simple swimmer at low Reynolds number: three linked spheres". In: *Phys. Rev. E* 69, p. 062901.

Nassir, Mayssam et al. (2022). "Prediction of sperm progression in three dimensions using rapid optical imaging and dynamic mechanical modeling". In: *Cells* 11.8, p. 1319.

Nguyen, Frank TM and Michael D Graham (2018). "Impacts of multiflagellarity on stability and speed of bacterial locomotion". In: *Physical Review E* 98.4, p. 042419.

Nord, A. L. et al. (2022). "Dynamic stiffening of the flagellar hook". In: *Nat. Comm.* 13, p. 2925.

Okamoto, Ken-Ichi and Yasuo Nakaoka (1994). "Reconstitution of Metachronal Waves in Ciliated Cortical Sheets of Paramecium: II. Asymmetry of the Ciliary Movements". In: *Journal of experimental biology* 192.1, pp. 73–81.

Olson, Merle E et al. (2002). "Biofilm bacteria: formation and comparative susceptibility to antibiotics". In: *Canadian journal of veterinary research* 66.2, p. 86.

Oseen, Carl Wilhelm (1910). "Uber die Stokes' sche Formel und Uber eine verwandte Aufgabe in der Hydrodynamik". In: *Arkiv Mat., Astron. och Fysik* 6, p. 1.

Pagonabarraga, I. and I. Llopis (2013). "The structure and rheology of sheared model swimmer suspensions". In: *Soft Matter* 9, pp. 7174–7184.

Palacci, J. et al. (2013). "Living crystals of light-activated colloidal surfers". In: *Science* 339, pp. 936–940.

Palagi, S. and P. Fischer (2018). "Bioinspired microrobots". In: *Nat. Rev. Mater.* 3, pp. 113–124.

Paul, Aloke et al. (2014). "Fick's laws of diffusion". In: *Thermodynamics, diffusion and the kirkendall effect in solids*, pp. 115–139.

Paxton, W. F. et al. (2006). "Chemical locomotion". In: *Angew. Chem. Int. Ed.* 45, pp. 5420–5429.

Paxton, Walter F et al. (2004). "Catalytic nanomotors: autonomous movement of striped nanorods". In: *Journal of the American Chemical Society* 126.41, pp. 13424–13431.

Pearce, P. et al. (2019). "Flow-induced symmetry breaking in growing bacterial biofilms". In: *Phys. Rev. Lett.* 123, p. 258101.

Peruani, F., A. Deutsch, and M. Bär (2006). "Nonequilibrium clustering of self-propelled rods". In: *Phys. Rev. E* 74, p. 030904.

Peterson, B. W. et al. (2015). "Viscoelasticity of biofilms and their recalcitrance to mechanical and chemical challenges". In: *FEMS Microbiol. Rev.* 39, pp. 234–245.

Petrova, Olga E and Karin Sauer (2009). "A novel signaling network essential for regulating Pseudomonas aeruginosa biofilm development". In: *PLoS pathogens* 5.11, e1000668.

Pivkin, I. V., B. Caswell, and G. E. Karniadakis (2011). "Dissipative Particle Dynamics". In: *Reviews in Computational Chemistry*. Ed. by K. B. Lipkowitz. Vol. 27. Hoboken, NJ, USA: John Wiley & Sons, Inc., pp. 85–110.

Platzer, Josef et al. (1997). "Three genes of a motility operon and their role in flagellar rotary speed variation in Rhizobium meliloti". In: *Journal of bacteriology* 179.20, pp. 6391–6399.

Pohl, Oliver and Holger Stark (2014). "Dynamic clustering and chemotactic collapse of self-phoretic active particles". In: *Physical review letters* 112.23, p. 238303.

— (2015). "Self-phoretic active particles interacting by diffusiophoresis: A numerical study of the collapsed state and dynamic clustering". In: *The European Physical Journal E* 38, pp. 1–11.

Popescu, M. N. et al. (2010). "Phoretic motion of spheroidal particles due to self-generated solute gradients". In: *Eur. Phys. J. E* 31, pp. 351–367.

Popescu, Mihail N, Siegfried Dietrich, and G Oshanin (2009). "Confinement effects on diffusiophoretic self-propellers". In: *The Journal of chemical physics* 130.19.

Popescu, MN, M Tasinkevych, and S Dietrich (2011). "Pulling and pushing a cargo with a catalytically active carrier". In: *Europhysics Letters* 95.2, p. 28004.

Preda, V. G. and O. Săndulescu (2019). "Communication is the key: biofilms, quorum sensing, formation and prevention". In: *Discoveries* 7, e100.

Purcell, E. M. (1977). "Life at low Reynolds number". In: *Am. J. Phys.* 45, pp. 3–11.

Purcell, Edward M (2014). "Life at low Reynolds number". In: *Physics and our world: reissue of the proceedings of a symposium in honor of Victor F Weisskopf*. World Scientific, pp. 47–67.

Qi, K. et al. (2020). "Rheotaxis of spheroidal squirmers in microchannel flow: interplay of shape, hydrodynamics, active stress, and thermal fluctuations". In: *Phys. Rev. Res.* 2, p. 033275.

Qi, K. et al. (2022). "Emergence of active turbulence in microswimmer suspensions due to active hydrodynamic stress and volume exclusion". In: *Commun. Phys.* 5, p. 49.

Qin, Boyang et al. (2015). "Flagellar kinematics and swimming of algal cells in viscoelastic fluids". In: *Scientific reports* 5.1, p. 9190.

Qu, Zijie et al. (2018). "Changes in the flagellar bundling time account for variations in swimming behavior of flagellated bacteria in viscous media". In: *Proceedings of the National Academy of Sciences* 115.8, pp. 1707–1712.

Redner, G. S., M. F. Hagan, and A. Baskaran (2013). "Structure and dynamics of a phase-separating active colloidal fluid". In: *Phys. Rev. Lett.* 110, p. 055701.

Reichert, Michael and Holger Stark (2005). "Synchronization of rotating helices by hydrodynamic interactions". In: *The European Physical Journal E* 17, pp. 493–500.

Reigh, S. Y., R. G. Winkler, and G. Gompper (2012). "Synchronization and bundling of anchored bacterial flagella". In: *Soft Matter* 8, pp. 4363–4372.

— (2013). "Synchronization, slippage, and unbundling of driven helical flagella". In: *PLoS ONE* 8, e70868.

Riley, Emily E, Debasish Das, and Eric Lauga (2018). "Swimming of peritrichous bacteria is enabled by an elastohydrodynamic instability". In: *Scientific reports* 8.1, p. 10728.

Rings, D. et al. (2010). "Hot Brownian motion". In: *Phys. Rev. Lett.* 105, p. 090604.

Rodenborn, Bruce et al. (2013). "Propulsion of microorganisms by a helical flagellum". In: *Proceedings of the National Academy of Sciences* 110.5, E338–E347.

Rodriguez, Patricia A et al. (2019). "Systems biology of plant-microbiome interactions". In: *Molecular plant* 12.6, pp. 804–821.

Romanczuk, P. et al. (2012). "Active Brownian Particles: From individual to collective stochastic dynamics". In: *Eur. Phys. J. Special Topics* 202, pp. 1–162.

Rückner, G. and R. Kapral (2007). "Chemically powered nanodimers". In: *Phys. Rev. Lett.* 98, p. 150603.

Rupp, C. J., C. A. Fux, and P. Stoodley (2005). "Viscoelasticity of *Staphylococcus aureus* biofilms in response to fluid shear allows resistance to detachment and facilitates rolling migration". In: *Appl. Environ. Microbiol.* 71, pp. 2175–2178.

Russell, James J et al. (2017). "Non-model model organisms". In: *BMC biology* 15, pp. 1–31.

Sabass, Benedikt and Udo Seifert (2012). "Dynamics and efficiency of a self-propelled, diffusiophoretic swimmer". In: *The Journal of chemical physics* 136.6.

Saintillan, David (2010). "The dilute rheology of swimming suspensions: A simple kinetic model". In: *Experimental Mechanics* 50, pp. 1275–1281.

Sanchez, T. et al. (2011). "Cilia-like beating of active microtubule bundles". In: *Science* 333, pp. 456–459.

Sanchez, T. et al. (2012). "Spontaneous motion in hierarchically assembled active matter". In: *Nature* 491, pp. 431–434.

Saragosti, Jonathan et al. (2011). "Directional persistence of chemotactic bacteria in a traveling concentration wave". In: *Proceedings of the National Academy of Sciences* 108.39, pp. 16235–16240.

Sauer, Karin et al. (2002). *Pseudomonas aeruginosa displays multiple phenotypes during development as a biofilm*.

Sauer, Karin et al. (2022). "The biofilm life cycle: expanding the conceptual model of biofilm formation". In: *Nature Reviews Microbiology* 20.10, pp. 608–620.

Schaar, K., A. Zöttl, and H. Stark (2015). "Detention times of microswimmers close to surfaces: influence of hydrodynamic interactions and noise". In: *Phys. Rev. Lett.* 115, p. 038101.

Scharf, B. (2002). "Real-time imaging of fluorescent flagellar filaments of *rhizobium lupini* H13-3: flagellar rotation and pH-induced polymorphic transitions". In: *J. Bacteriol.* 184, pp. 5979–5986.

Schmidt, Christine K et al. (2020). "Engineering microrobots for targeted cancer therapies from a medical perspective". In: *Nature Communications* 11.1, p. 5618.

Sen, Anindito, Ranjan K Nandy, and Amar N Ghosh (2004). "Elasticity of flagellar hooks". In: *Microscopy* 53.3, pp. 305–309.

Sentenac, Hugo et al. (2022). "The significance of biofilms to human, animal, plant and ecosystem health". In: *Functional Ecology* 36.2, pp. 294–313.

Sharma, D., L. Misba, and A. U. Khan (2019). "Antibiotics versus biofilm: an emerging battleground in microbial communities". In: *Antimicrob. Resist. Infect. Control* 8, p. 76.

Sipos, Orsolya et al. (2015). "Hydrodynamic trapping of swimming bacteria by convex walls". In: *Physical review letters* 114.25, p. 258104.

Sokolov, Andrey and Igor S Aranson (2012). "Physical properties of collective motion in suspensions of bacteria". In: *Physical review letters* 109.24, p. 248109.

Solon, A. P. et al. (2015). "Pressure and phase equilibria in interacting active Brownian spheres". In: *Phys. Rev. Lett.* 114, p. 198301.

Son, Kwangmin, Jeffrey S Guasto, and Roman Stocker (2013). "Bacteria can exploit a flagellar buckling instability to change direction". In: *Nature physics* 9.8, pp. 494–498.

Spagnolie, S. E. and E. Lauga (2012). "Hydrodynamics of self-propulsion near a boundary: predictions and accuracy of far-field approximations". In: *J. Fluid Mech.* 700, pp. 105–147.

Spöring, I. et al. (2018). "Hook length of the bacterial flagellum is optimized for maximal stability of the flagellar bundle". In: *PLoS Biol.* 16, e2006989.

Stancil, Kimani A (2012). "Introduction to statistical mechanics; statistical mechanics in a nutshell". In: *Physics Today* 65.8, pp. 50–52.

Stenhammar, J. et al. (2017). "Role of correlations in the collective behavior of microswimmer suspensions". In: *Phys. Rev. Lett* 119, p. 028005.

Stoodley, Paul et al. (2002). "Biofilms as complex differentiated communities". In: *Annual Reviews in Microbiology* 56.1, pp. 187–209.

Succi, S. (2001). *The Lattice Boltzmann equation for fluid dynamics and beyond*. Oxford: Oxford University Press.

Tailleur, J. and M. E. Cates (2008). "Statistical mechanics of interacting run-and-tumble bacteria". In: *Phys. Rev. Lett.* 100, p. 218103.

Tailleur, Julien and ME Cates (2009). "Sedimentation, trapping, and rectification of dilute bacteria". In: *Europhysics Letters* 86.6, p. 60002.

Tallawi, M., M. Opitz, and O. Lieleg (2017). "Modulation of the mechanical properties of bacterial biofilms in response to environmental challenges". In: *Biomater. Sci.* 5, pp. 887–900.

Tamm, Sidney L and George Adrian Horridge (1970). "The relation between the orientation of the central fibrils and the direction of beat in cilia of Opalina". In: *Proceedings of the Royal Society of London. Series B. Biological Sciences* 175.1040, pp. 219–233.

Tamm, Sidney L, TM Sonneborn, and Ruth V Dippell (1975). "The role of cortical orientation in the control of the direction of ciliary beat in Paramecium." In: *The Journal of cell biology* 64.1, pp. 98–112.

Taute, K. M. et al. (2015). "High-throughput 3D tracking of bacteria on a standard phase contrast microscope". In: *Nat. Comm.* 6, p. 8776.

Thakur, S. and R. Kapral (2011). "Dynamics of self-propelled nanomotors in chemically active media". In: *J. Chem. Phys.* 135, p. 024509.

Theers, M. et al. (2016a). "From local to hydrodynamic friction in Brownian motion: a multiparticle collision dynamics simulation study". In: *Phys. Rev. E* 93, p. 032604.

— (2016b). "Modeling a spheroidal microswimmer and cooperative swimming in a narrow slit". In: *Soft Matter* 12, pp. 7372–7385.

Theers, M. et al. (2018). "Clustering of microswimmers: interplay of shape and hydrodynamics". In: *Soft Matter* 14, pp. 8590–8603.

Theillard, M., R. Alonso-Matillaa, and D. Saintillan (2017). "Geometric control of active collective motion". In: *Soft Matter* 13, pp. 363–375.

Theurkauff, Isaac et al. (2012). "Dynamic clustering in active colloidal suspensions with chemical signaling". In: *Physical review letters* 108.26, p. 268303.

Thompson, Alasdair G et al. (2011). "Lattice models of nonequilibrium bacterial dynamics". In: *Journal of Statistical Mechanics: Theory and Experiment* 2011.02, P02029.

Toner, M. and D. Irimia (2005). "Blood-on-a-chip". In: *Annu. Rev. Biomed. Eng.* 7, pp. 77–103.

Tran, Stephanie et al. (2017). "Cancer nanomedicine: a review of recent success in drug delivery". In: *Clinical and translational medicine* 6, pp. 1–21.

Tu, Yuhai and G Grinstein (2005). "How white noise generates power-law switching in bacterial flagellar motors". In: *Physical review letters* 94.20, p. 208101.

Turner, L., W. S. Ryu, and H. C. Berg (2000). "Real-time imaging of fluorescent flagellar filaments". In: *J. Bacteriol.* 182, pp. 2793–2801.

Tuson, Hannah H et al. (2013). "Flagellum density regulates Proteus mirabilis swarmer cell motility in viscous environments". In: *Journal of bacteriology* 195.2, pp. 368–377.

Uppaluri, S. et al. (2011). "Impact of microscopic motility on the swimming behavior of parasites: straighter trypanosomes are more directional". In: *PLoS Comput. Biol.* 7, e1002058.

Vandenkoornhuyse, Philippe et al. (2015). "The importance of the microbiome of the plant holobiont". In: *New Phytologist* 206.4, pp. 1196–1206.

Verstraeten, N. et al. (2008). "Living on a surface: swarming and biofilm formation". In: *Trends Microbiol.* 16, pp. 496–506.

Vicsek, T. and A. Zafeiris (2012). "Collective motion". In: *Phys. Rep.* 517, pp. 71–140.

Vicsek, Tamás et al. (1995). "Novel type of phase transition in a system of self-driven particles". In: *Physical review letters* 75.6, p. 1226.

Vigeant, M. A.-S. et al. (2002). "Reversible and irreversible adhesion of motile *Escherichia coli* cells analyzed by total internal reflection aqueous fluorescence microscopy". In: *Appl. Environ. Microbiol.* 68, pp. 2794–2801.

Vigeant, MA and Roseanne M Ford (1997). "Interactions between motile Escherichia coli and glass in media with various ionic strengths, as observed with a three-dimensional-tracking microscope". In: *Applied and Environmental Microbiology* 63.9, pp. 3474–3479.

Vladescu, I. D. et al. (2014). "Filling an emulsion drop with motile bacteria". In: *Phys. Rev. Lett.* 113, p. 268101.

Vogel, Reinhard and Holger Stark (2010). "Force-extension curves of bacterial flagella". In: *The European Physical Journal E* 33.3, pp. 259–271.

— (2012). "Motor-driven bacterial flagella and buckling instabilities". In: *The European Physical Journal E* 35, pp. 1–15.

Volpe, G. et al. (2011). "Microswimmers in patterned environments". In: *Soft Matter* 7, pp. 8810–8815.

Vorholt, Julia A (2012). "Microbial life in the phyllosphere". In: *Nature reviews microbiology* 10.12, pp. 828–840.

Wang, Fangbin et al. (2017). "Non-equilibrium effect in the allosteric regulation of the bacterial flagellar switch". In: *Nature Physics* 13.7, pp. 710–714.

Watari, N. and R. G. Larson (2010). "The hydrodynamics of a run-and-tumble bacterium propelled by polymorphic helical flagella". In: *Biophys. J.* 98, pp. 12–17.

Wensink, H. H. and H. Löwen (2008). "Aggregation of self-propelled colloidal rods near confining walls". In: *Phys. Rev. E* 78, p. 031409.

Wensink, H. H. et al. (2012). "Meso-scale turbulence in living fluids". In: *Proc. Natl. Acad. Sci. USA* 109, pp. 14308–14313.

Wichterman, Ralph (2012). *The biology of Paramecium*. Springer science & business media.

Williams, B. J. et al. (2014). "A self-propelled biohybrid swimmer at low Reynolds number". In: *Nat. Comm.* 5, p. 3081.

Wingender, J., T. R. Neu, and H.-C. Flemming, eds. (1999). *Microbial extracellular polymeric substances: characterization, structure and function*. Heidelberg: Springer.

Wioland, H. et al. (2013). "Confinement stabilizes a bacterial suspension into a spiral vortex". In: *Phys. Rev. Lett.* 110, p. 268102.

Wolgemuth, Charles W (2008). "Collective swimming and the dynamics of bacterial turbulence". In: *Biophysical journal* 95.4, pp. 1564–1574.

Worlitzer, Vasco M et al. (2022). "Biophysical aspects underlying the swarm to biofilm transition". In: *Science advances* 8.24, eabn8152.

Wu, Y (2017). "Chapter 7–The evaluation of phosphorus removal processes and mechanisms from surface water by periphyton". In: *Periphyton, Boston: Elsevier*, pp. 171–202.

Wu, Yonghong (2016). *Periphyton: functions and application in environmental remediation*. Elsevier.

Wu-Zhang, Bohan, Dmitry A Fedosov, and Gerhard Gompper (2024). "Collective behavior of squirmers in thin films". In: *Soft Matter*.

Yamakawa, Hiromi (1997). *Helical wormlike chains in polymer solutions*. Vol. 1. Springer.

Yan, Wen and John F Brady (2015). "The force on a boundary in active matter". In: *Journal of Fluid Mechanics* 785, R1.

Yang, Lin and Paschalis Alexandridis (2000). "Physicochemical aspects of drug delivery and release from polymer-based colloids". In: *Current opinion in colloid & interface science* 5.1-2, pp. 132–143.

Yang, M. and M. Ripoll (2011). "Simulations of thermophoretic nanoswimmers". In: *Phys. Rev. E* 84, p. 061401.

Yoshinaga, N. and T. B. Liverpool (2017). "Hydrodynamic interactions in dense active suspensions: from polar order to dynamical clusters". In: *Phys. Rev. E* 96, p. 020603.

Zhang, He-Peng et al. (2010). "Collective motion and density fluctuations in bacterial colonies". In: *Proceedings of the National Academy of Sciences* 107.31, pp. 13626–13630.

Zhang, HP et al. (2009). "Swarming dynamics in bacterial colonies". In: *Europhysics Letters* 87.4, p. 48011.

Zhang, X. et al. (2023). "Differential bending stiffness of the bacterial flagellar hook under counterclockwise and clockwise rotations". In: *Phys. Rev. Lett.* 130, p. 138401.

Zhang, Yong et al. (2012). "From individual cell motility to collective behaviors: insights from a prokaryote, Myxococcus xanthus". In: *FEMS microbiology reviews* 36.1, pp. 149–164.

Zöttl, A. and H. Stark (2012). "Nonlinear dynamics of a microswimmer in Poiseuille flow". In: *Phys. Rev. Lett.* 108, p. 218104.

Zöttl, A. and H. Stark (2014). "Hydrodynamics determines collective motion and phase behavior of active colloids in quasi-two-dimensional confinement". In: *Phys. Rev. Lett.* 112, p. 118101.

Zöttl, A. and H. Stark (2018). "Simulating squirmers with multiparticle collision dynamics". In: *Eur. Phys. J. E* 41, p. 61.

Zwanzig, Robert (2001). *Nonequilibrium statistical mechanics*. Oxford university press.

Acknowledgements

Time flies, my PhD mission is closer to the end. Three years are fast, but I have many people who I appreciate and thank for. Firstly, I appreciate my colleagues from my own small group: Alper, Florian, and Priyanka. We are like a family in our institute and thank for a lot of help and warmth that they offered to me. Other colleagues are also on my thank list: Johannes, Amir and Kai. A big thank to Kai, thanks for the lunch that we spent together so that I can still practice my Chinese; a warm thank to Amir for all the chatty bus trips to Aachen we shared.

My visit to Paris also gave me the chances to make new friends, especially Peixin and Zhibo, a lovely couple invited me to their home when I did not have a bed to sleep during my Paris stay. Furthermore, the friendship that I have developed with her during the three years under PHYMOT scheme makes me appreciate the luck I have. It has also been a pleasure to share with her my burden, my pressure and also my happiness. I will be certain that our friendship will be forever. Also, a cute thank to Benjamin, thanks for his patiently teaching the experimental techniques to me (a theorist). Since he is a newlywed, I want to wish him a happy marriage forever.

I have also made other friends within the PHYMOT scheme, Farnoosh, Erica, Fedrica, Eva, Medea, Luc and many other. The meetings with them colours normally speaking boring conferences, I still miss the jokes we made and the heartful chat we had after a drink. Wish all of them best of luck in the future and I hope our life would cross again.

Apart from them, my dearest friends in UK (Rui and Jessie), in China (Xiaochen, Shuai), in Aachen (Sen, Yudi, Yinyin, Tom, Xinyi) and in Netherlands (Helen) all warm up my cold and lonely life in Aachen where I do not feel like belonging to. The appreciation is beyond words. It is my honour to have them in my life and I wish to continue the friendships.

My mentor, Dmitry Fedosov, who taught me the way of doing research and leads me to the door of academia. I thank for all of his help and support he have been giving to me. A thank should also go to Gerrit Vliegenthart, the tallest guy I have ever seen in my life, who organises the miscellaneous work of PHYMOT network and really enjoyed the gift of a photo of Felipe II from me despite being a Dutch. My biggest boss Gerhard Gompper, who first provided me with salary, and always lighten up the atmosphere with his typical jokes, especially his jokes about "almost veggie". I also appreciate the help from Anke Lindner and Eric Clement when I was in Paris. Also, I want to thank Jorge R Espinosa and Rosalind Allen who offered me help for Postdoc searching.

Family is always part of acknowledgement as we cannot achieve what we have today without the support from them. I want to thank my parents for their many years of support for my dream. I appreciate their understanding for whatever decision that I made and the freedom they gave to me. I appreciate their care and I really wish they could enjoy their own life now. Also, I want to express my great appreciation to the family of my partner who have been treating me like their own kid. Thank for their kindness, I have felt great warmth in this unfamiliar land and have enjoyed Christmas never before.

The list will end now with a very important name in my life: my partner, Andres Tejedor. Thanks for his love and encouragement which makes me going through one of the darkest and toughest period of my life. Thanks for his understanding and patience to my childishness. Thanks for his comforting when I lose my temper. This can go on and on. I hope I could use the rest of my life to express my appreciation back.

As a joke, I want to thank Deutsche Bahn (DB). Thanks for them to be so slow and inefficient so that I want to finish my PhD fast and leave the country. In the last year, I have been collecting the reasons that DB claims when the train delays. They include: 1) Police activity; 2) Preparation of additional wagons; 3) Track repairs; 4) Unexpected stuff illness; 5) Technical fault on another train; 6) Another train has priority; 7) Due to delays, a connecting service may not be reachable; 8) Delayed train preparation; 9) Delay outside of Germany; 10) Snow and ice; 11) Impact of adverse weather; 12) Train repairs; 13) Unauthorised people on line; 14) Staff delayed due to earlier journey; 15) Construction work; 16) Delay of previous train; 17) Cow on the tracks; 18) Wait due to connecting passengers; 19) Intervention by authorities; 20) Unexpected staff shortage. 21) Medical emergency on the line.

Declaration of Authorship

In the dissertation, we have not used any artificial intelligence tool like ChatGPT to generate any text for this thesis, A basic Grammarly application (without AI) is used to check for grammar mistakes. Also, DeepL is used to translate the English abstract to the German abstract.

According to the Doctoral Regulations of the Faculty of Mathematics and Natural Sciences of the University of Cologne on March 12, 2020, I must also clarify my contribution to this part of the thesis as a published manuscript.

Chapter 4, section 3.1, section 3.2 and section 3.4.2 in chapter 3 have been published in Soft Matter, 2024 (Wu-Zhang, Fedosov, and Gompper, 2024) as the title of "Collective behavior of squirmers in thin films," written by Bohan Wu-Zhang (first author), Dmitry A. Fedosov and Gerhard Gompper. Bohan Wu-Zhang is also the author of the thesis. In this project, I performed the simulations, coded for the listed analyses, and wrote the manuscript under the supervision of Dmitry A. Fedosov and Gerhard Gompper. Gerhard Gompper designed the project, and Dmitry A. Fedosov provided me with daily supervision. All three people contribute to the writing of the manuscript.

Chapter 5, and section 3.3 in chapter 3 serves as the framework of a publication under the name of "Importance of Different *E. Coli* Characteristics for its Run and Tumble Behavior" **in the future**. Bohan Wu-Zhang (the author of the thesis) is the first author of the future publication who performed the simulations, coded for the listed analyses, and wrote the chapter and the manuscript under the supervision of Dmitry A. Fedosov and Gerhard Gompper. Gerhard Gompper and Dmitry A. Fedosov designed the project. Peixin Zhang and Renaud Baillou performed the experiments and provided the experimental data, under the supervision of Anke Lindner and Eric Clement. All people contribute to the writing of the manuscript in preparation.